ULTRA-SMALL RARE-EARTH OXIDE NANOCRYSTALS: DEVELOPMENT, FILM ASSEMBLY, OPTICAL AND DIELECTRIC STUDIES

by

Sameer V. Mahajan

Dissertation

Submitted to the Faculty of the

Graduate School of Vanderbilt University

in partial fulfillment of the requirements

for the degree of

DOCTOR OF PHILOSOPHY

in

Interdisciplinary Materials Science

May, 2010

Nashville, Tennessee

Approved:

Professor James H. Dickerson

Professor Richard Haglund

Professor Sandra Rosenthal

Professor Kalman Varga

Professor Greg Walker

INTERDISCIPLINARY MATERIALS SCIENCE

ULTRA-SMALL RARE-EARTH OXIDE NANOCRYSTALS: DEVELOPMENT, FILM ASSEMBLY, OPTICAL AND DIELECTRIC STUDIES

SAMEER V. MAHAJAN

Dissertation under the direction of Professor James H. Dickerson

The oxides of rare-earth elements (rare-earth sesquioxide: RE_2O_3) are known for their optical and dielectric properties. Europium oxide is known for characteristic red luminescence and gadolinium oxide has excellent insulating properties (band gap: 5.5 eV). Development of ultra-small nanocrystals (sub-3 nm diameter) of these rare-earth oxides and investigation of their optical and dielectric properties are explored in this dissertation. A new synthesis process was developed successfully to produce ultra-small colloidal nanocrystals, which were capped with oleic acid. Europium oxide nanocrystals exhibited a new luminescence peak because of the occupation of Eu^{3+} ions in a surface site. The nanocrystals were assembled into films from their suspensions in hexane by electrophoretic deposition. Films of europium oxide were highly transparent in visible spectral region because of minimal scattering losses within the films and exhibited characteristic red luminescence. Gadolinium oxide nanocrystals exhibited charge-storage properties when integrated in a metal-insulator-semiconductor structure. Layered heterostructures of carbon nanotubes and nanocrystals were fabricated and their charge-storage properties were studied.

Dedicated

to

My parents, Mrs. Vaishali V. Mahajan and Mr. Vinayak P. Mahajan,

and my sister, Mrs. Ashwini N. Joshi

for their encouragement and support to pursue graduate studies in the USA

ACKNOWLEDGEMENT

First, I express my utmost gratitude towards Prof. James H. Dickerson, my advisor and the Chair of my Ph.D. committee, for providing me the opportunity to work in the exciting research area of nanotechnology. His guidance and support that he has provided at various stages of my Ph.D. work have been invaluable. I thank him for teaching me how to organize scientific thoughts, to write scientific documents, and to present research effectively. Also, his encouragement and support to present the exciting research at various national and international conferences was extremely important.

I am grateful to the other members of my Ph.D. committee: Prof. Richard Haglund, Prof. Sandra Rosenthal, Prof. Kalman Varga, and Prof. Greg Walker for their guidance and time during the development of this dissertation work.

I would like to thank Dr. Marcela L. Rediolo and Dr. Dmitry S. Koktysh for getting me started with the experimental nanoscience work in the laboratory.

Special thanks go to my colleagues: Dr. Dustin W. Kavich, Suseela Somarajan, Melissa Harrison, Saad Hasan, John Riguer, and Weidong He for their assistance in the day-to-day laboratory activities, and Dr. Eugenii Donev and Dr. John Rozen for their help with learning LaTex.

I thank Mrs. Sarah Ross-Satterwhite, Interdisciplinary Materials Science Program Coordinator, for her assistance during my tenure as a graduate student at Vanderbilt University.

I would like to thank the National Science Foundation (NSF) for financial support through award DMR-0757380, the Vanderbilt Institute for Nanoscale Science and Engineering (VINSE), and the Center for Nanophase Materials Sciences (CNMS) of Oak Ridge National Laboratory (ORNL) through user grants CNMS2005-011 & CNMS2007-011.

My earnest thanks to my friends: Dr. Sriram Dixit, Dr. Saumitra Vajandar, Dr. Nageswara Rao Sunkaranam, Dr. Sachin Bet, Dr. Vaishali Ukirde, Dr. Anuradha Bulusu,

Dr. Karthik Subramanian, Dr. Anupama Balsubramanian, and Anusha Rao for their friendship and support.

Finally, I am able to reach this stage in my career purely because of the never-ending encouragement, support, and belief in me of my parents, for which I cannot thank them enough. My heartfelt thanks to my sister who has supported me in pursuing graduate studies in the USA and has been taking care of my parents. And of course, I specially thank my wife, Ketaki for her untiring support during the final stage of my Ph.D. work. Her wonderful company here in Nashville has made the final difficult stage of Ph.D. easy.

TABLE OF CONTENTS

LIST OF TABLES

LIST OF FIGURES

CHAPTER I

INTRODUCTION

1.1 Overview

The lanthanide series elements [lanthanide (La, atomic number 57) to lutetium (Lu, atomic number 71)], scandium (Sc, atomic number 21), and yttrium (Y, atomic number 39) are called rare-earth (RE) elements. The oxides of these elements are called rare-earth oxides, which have been widely used in a variety of applications: as activators and/or sensitizers in phosphors, as dopants in glasses for coloring, as dopants in optical fibers, as ultraviolet (UV) absorbing materials in glasses, as neutron absorber in nuclear reactors, as catalysts in chemical reactions, and as light emitters in tricolor fluorescent lamps. Generally, rare-earth oxides are found in three compositions: monoxide (REO), sesquioxide (RE_2O_3), and dioxide (REO_2). Of these compositions, rare-earth sesquioxide is the most thermally and chemically stable composition of majority of the rare-earth elements, which form stable trivalent ions (RE^{3+}). The RE^{3+} ions (Ce^{3+} to Yb^{3+}) have partially filled $4f$ orbitals, while the RE^{3+} ions (Sc^{3+}, Y^{3+}, La^{3+}) have empty $4f$ orbitals and Lu^{3+} have completely filled $4f$ orbitals. The ground state electronic configurations of the lanthanide RE^{3+} ions (La^{3+} to Lu^{3+}) are characterized as [Xe]$4f^n$ (n = 0 - 14). Various RE^{3+} ions have emission transition energies, arising from their ground state electronic configurations, in or near the visible region of the electromagnetic spectrum (Table 1.1).[1] Therefore, these ions exhibit emission peaks in or near visible spectral region. Emission spectra of some of these ions is shown in figure 1.1. These peaks are sharp due to the discrete energy levels of the RE^{3+} ions. Since the $4f$ electrons of these ions are well shielded from surrounding anions by completely filled outer $5s^2$ and $5p^6$ electrons, the energy levels are discrete and are not affected much by a crystallographic environment. The splitting of these energy levels into multiple energy

Table 1.1: Electronic configurations and emission colors of trivalent rare-earth ions.[1]

Ions	Electronic configuration	Emission color	Ions	Electronic configuration	Emission color
Ce^{3+}	$4f^1$	ultraviolet, green	Tb^{3+}	$4f^8$	green
Pr^{3+}	$4f^2$	blue, green, red	Dy^{3+}	$4f^9$	yellow
Nd^{3+}	$4f^3$	near infrared (NIR)	Ho^{3+}	$4f^{10}$	blue, green
Sm^{3+}	$4f^5$	pink	Er^{3+}	$4f^{11}$	green, IR
Eu^{3+}	$4f^6$	red	Tm^{3+}	$4f^{12}$	blue
Gd^{3+}	$4f^7$	ultraviolet	Yb^{3+}	$4f^{13}$	blue, NIR

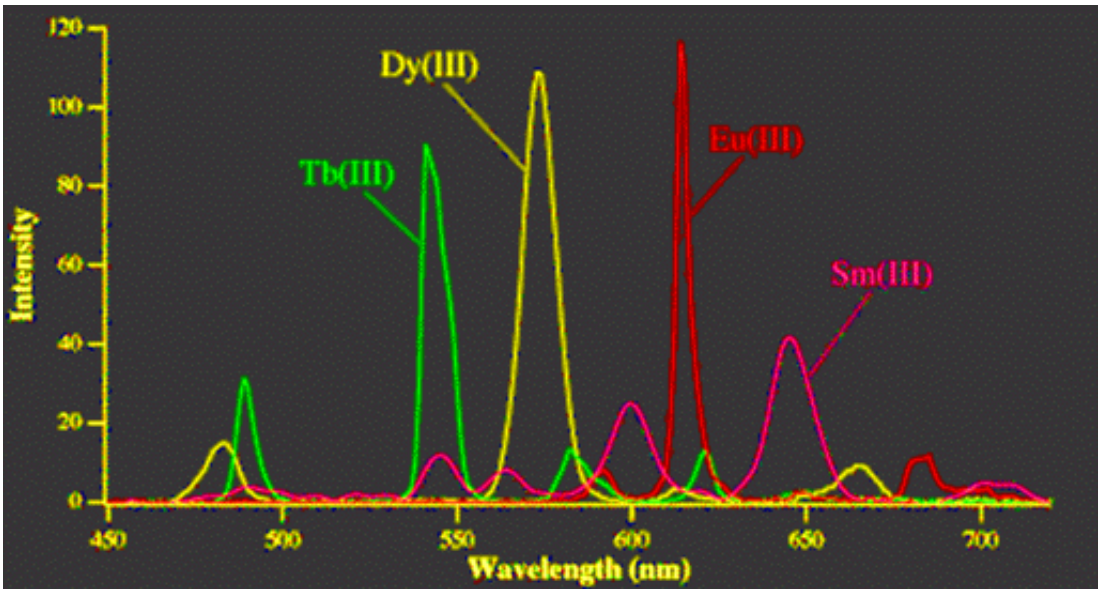

Figure 1.1: Emission spectra of some of the RE^{3+} ions, which show emission peaks in the visible region. The source of this image is unknown.

manifolds occur by the crystal field when RE^{3+} ions reside in a crystallographic environment. The splitting is very small because of the shielding of the $4f$ electrons. Hence, the rare-earth sesquioxides (RE_2O_3) comprising the RE^{3+} ions exhibit sharp emission peaks, which are characteristic of those ions. Since the RE^{3+} ions offer such a wide range of emission colors and their oxides are very stable, these rare-earth oxides are well known as luminescent materials for their optical characteristics. Apart from the luminescence characteristics, the rare-earth sesquioxides are known for their excellent dielectric properties (high-κ), which also arise from their electronic configuration.[4] Within the scope of this dissertation, the rare-earth sesquioxides (RE_2O_3) are defined as the rare-earth oxides (REOs).

Of all the rare-earth oxides, europium oxide (Eu_2O_3) and terbium oxide (Tb_2O_3) have been investigated most thoroughly because they offer two of the three basic colors required in red-green-blue (RGB) pixel-based video display devices and in tricolor fluorescent lamps. Luminescence from these materials is observed when they are excited with high-energy photons (UV), fast electrons, X-rays, or γ-rays. Generally, Eu^{3+}/Tb^{3+}-doped in a non-luminescent oxide host lattice is employed instead of a pure oxide (Eu_2O_3 and Tb_2O_3) to minimize concentration-dependent luminescence quenching, known as concentration quenching. Migration of the excitation energy and the exchange interaction between the identical luminescent ions (Eu^{3+}/Tb^{3+}) in the pure host lattice remain central to the concentration quenching effect (Section 1.3.4). The energy migration and exchange interaction are strongly dependent on distance between the identical luminescent ions. Doping of luminescent ions in a non-luminescent host lattice increases distance between them and thus minimizes the energy transfer. Gadolinium oxide or yttrium oxide (Gd_2O_3/Y_2O_3) are preferred over other host lattices because these oxides have same crystal structure and have similar lattice constants compared to the Eu_2O_3 and Tb_2O_3. These oxides are non-luminescent in the visible region. Also, the doping technique facilitates efficient energy transfer from the Gd_2O_3/Y_2O_3 host lattice to the Eu^{3+}/Tb^{3+} ions when the host lattice is excited with X-rays, γ-rays, and fast electrons. Overall, luminescence efficiency of

Eu^{3+}/Tb^{3+}-doped Gd_2O_3/Y_2O_3 is higher than that of pure Eu_2O_3 and Tb_2O_3. These oxides in their microcrystalline form (1 - 10 μm) have been employed in various commercial applications such as cathode-ray tube (CRT) and projection television screens, tricolor fluorescent lamps, and X-ray intensifying screens.[5,6]

Over the past decade, nanocrystalline Eu^{3+}/Tb^{3+}-doped Gd_2O_3/Y_2O_3, Eu_2O_3, and Tb_2O_3 materials have gained significant research interest, which stems from widespread use of their microcrystalline particles in various optical devices. The nanocrystals have potential applications in high-resolution, energy-efficient video display devices, in efficient solid-state lighting applications, and as bright luminescent probes in immunoassays.[7,8] Typically, nanocrystals are single crystals with sizes in the sub-100 nm regime. Since nanocrystals are typically single crystals, they do not have grain boundaries. Since grain boundaries, present in polycrystalline particles, are defect sites where the excitation energy can be lost non-radiatively, their absence in nanocrystals is beneficial. In addition, various nanocrystal synthesis procedures do not employ the mechanical grinding or milling processes, which are employed in the production of microcrystalline rare-earth oxide particles. Thus, surface defects that are produced on the particles by mechanical grinding and milling processes are avoided in nanocrystals. Since nanocrystals have large surface-to-volume (SVR) ratio, they have a large number of surface defects if their surfaces are not passivated. The nanocrystal synthesis procedures should passivate nanocrystal's surfaces by reducing a number of surface defects that act as luminescence quenching sites, and thus increase luminescence efficiency.[3] Additionally, the surface passivation of nanocrystals improves their colloidal stability, which is important for their implementation in biological applications. For example, nanocrystals are dispersed in a variety of solvents, for which colloidal stability prevents nanocrystal agglomeration and, hence, facilitates the manipulation and distribution of the nanocrystals in biological applications.

The primary research thrust within scientific community has been to develop techniques to produce nanocrystals of Eu^{3+}/Tb^{3+}-doped Gd_2O_3/Y_2O_3, Eu_2O_3, and Tb_2O_3 and

to study their optical properties. Important findings reported by the scientific community are outlined here in chronological order.

Eilers H. *et al.*[9] (1995): *Synthesis of nanophase ZnO, Eu_2O_3, and ZrO_2, by gas-phase condensation with cw-CO_2 laser heating*

- A cw-CO_2 laser was employed to directly heat cubic phase Eu_2O_3 pellet to gaseous phase, which was condensed on a cold finger to form nanophase Eu_2O_3.
- Nanophase Eu_2O_3 had monoclinic crystal structure, which is a metastable phase at room temperature. The particle size varied between 2 - 30 nm diameter.

Bihari B. *et al.*[10] (1997): *Spectra and dynamics of monoclinic Eu_2O_3 and Eu^{3+}:Y_2O_3 nanocrystals*

- Spectroscopy studies of monoclinic Eu_2O_3 and Eu^{3+}:Y_2O_3 nanocrystals of 14 and 23 nm average diameter, respectively were conducted at low temparature ($\sim$ 10 K). The gas-phase condensation technique was employed for the synthesis of the nanocrystals.
- The excitation spectra of nanocrystalline Eu_2O_3 showed sharp peaks at 578.5 nm, 582.2 nm, and 582.4 nm corresponding to the three distinct crystallographic sites (labeled as A, B, and C, respectively) where Eu^{3+} ions reside in the monoclinic crystal structure. Energy transfer between the three sites was studied by selectively exciting different sites and observing intensities of emission peaks. Energy transfer was observed between all three sites.
- Similar site selective excitation studies, performed on 0.1 wt % Eu^{3+}:Y_2O_3, revealed that energy transfer occurs from site A to sites B and C, but energy transfer between sites B and C was not observed. Energy transfer occured between all the sites for Eu^{3+} ion concentration of 0.7 wt % and higher.

Goldburt E. T. *et al.*[2] (1997): *Size dependent efficiency in Tb doped Y_2O_3 nanocrystalline phosphor*

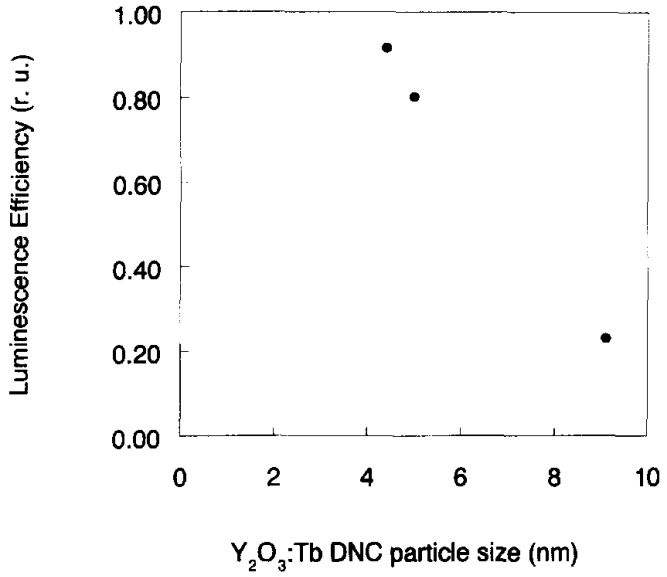

Figure 1.2: Luminescence efficiency of Tb^{3+}-doped Y_2O_3 nanocrystals as a function of size. After Goldburt ET *et al.*[2]

- Sol-gel techniques were employed to produce Tb doped Y_2O_3 nanocrystals with diameters between 4 - 10 nm. Monodispersivity of the nanocrystals was between 25 % - 40 %.

- Increase in luminescence efficiency of the nanocrystals was observed as the size decreased. Figure 1.2 shows the graph of luminescence efficiency as a function of nanocrystal size. The nanocrystals had 40 % efficiency of that of conventional Tb^{3+}:LaOBr phosphor.

Wakefield G. *et al.*[3,11] (1999): *Synthesis and properties of sub-50-nm europium oxide nanoparticles* and *Structural and optical properties of terbium oxide nanoparticles*

- Eu_2O_3 and Tb_2O_3 nanocrystals of cubic phase were synthesized by a colloidal precipitation technique. The nanocrystals were passivated with a layer of trioctyl phosphine oxide (TOPO) in order to minimize non-radiative transition pathways. The Eu_2O_3 nanocrystals were synthesized in the size range 2 - 40 nm, while the Tb_2O_3 nanocrystals of an average 4.2 nm diameter were produced.

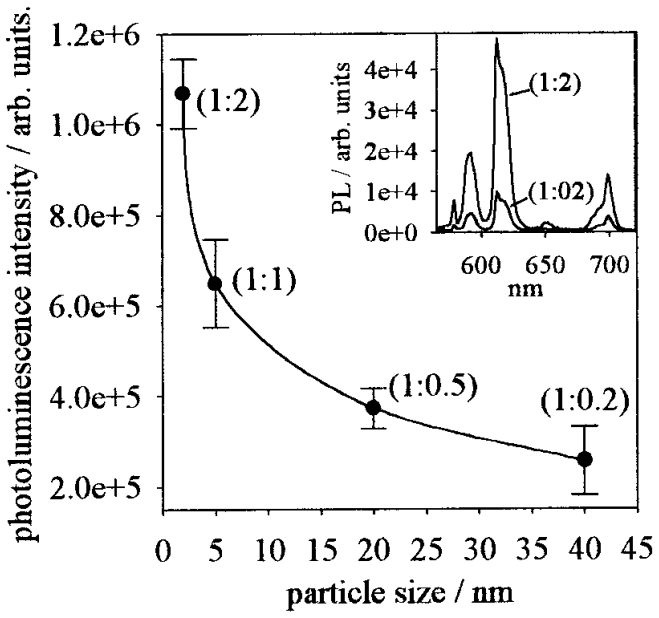

Figure 1.3: Variation in the photoluminescence intensity with particle size per unit mass of particles. The figures given in brackets are the Eu^{3+}/TOPO ratios. Inset: The photoluminescence spectra of Eu_2O_3 nanocrystals with Eu^{3+}/TOPO ratios of 1:2 and 1:0.02, respectively. After Wakefield G *et al.*[3]

- Photoluminescence intensity of Eu_2O_3 nanocrystals increased as the nanocrystal size decreased as shown in figure 1.3.

- Absorption spectrum of Tb_2O_3 nanocrystals showed no absorption edge at 400 - 600 nm, which confirmed absence of Tb^{4+} ions and formation of Tb_2O_3. Luminescence efficiency of these nanocrystals was 37 %.

Bazzi R. *et al.*[12] (2004): *Synthesis and properties of europium-based phosphors on the nanometer scale: Eu_2O_3, Gd_2O_3:Eu, and Y_2O_3:Eu*

- Cubic phase Eu_2O_3 and Eu^{3+}-doped Y_2O_3 and Gd_2O_3 nanocrystals were synthesized at high temperature (180 °C) in a high boiling-point alcohol (diethylene glycol) by colloidal precipitation. Nanocrystals with average diameter in the range 2 - 5 nm were produced.

- Emission peaks of these nanocrystals corresponded to the known emission transi-

tions of Eu^{3+} ions in the cubic phase lattice (Eu_2O_3, Gd_2O_3, and Y_2O_3). In the nanocrystals, relative intensities of the emission peaks were modified and the peaks were broadened when compared with bulk. The broadening was attributed to disorder within the nanocrystals.

Si R. *et al.*[13] (2005): *Rare-earth oxide nanopolyhedra, nanoplates, and nanodisks*

- A synthesis technique to produce anisotropic rare-earth oxide nanostructures by thermolysis of their benzoylacetonate complexes in oleic acid/oleylamine was developed. The selective adsorption of the capping ligands (oleic acid or oleylamine) on certain cubic faces during crystal growth facilitated production of different anisotropic structures such as nanopolyhedra, nanoplates, and nanodisks. Anisotropic structures (nanodisks and/or nanoplates) of the Eu_2O_3, Gd_2O_3, Tb_2O_3, and Y_2O_3 were produced in the size range of 10 - 70 nm diameter/ edge length.

- A new emission peak at 625 nm was observed in the photoluminescence spectrum of the Eu_2O_3 nanodisks. Further studies were conducted by the same group and the presence of this peak was later attributed to the occupation of Eu^{3+} ions in a unique surface site of ultrathin nanodisks of Eu_2O_3.[14]

Yang H. S. *et al.*[15] (2005): *Anisotropic growth of luminescent Eu^{3+}- or Er^{3+}-doped Gd_2O_3 nanocrystals*

- Anisotropic Eu^{3+}- or Er^{3+}-doped Gd_2O_3 nanocrystals of monoclinic crystal structure were prepared by a two-stage solution phase technique. Metal oleate complexes were decomposed in a trioctyamine-trioctylphosphine oxide mixture to produce these nanostructures. Selective adsorption of the surface capping ligands on certain crystal surfaces resulted in the growth of aniosotropic structures. Edge length of these nanostructures varied between 11 - 16 nm with approximate thickness of 1 nm. Broadening of the emission peaks in the photoluminescence spectra of these nanostructures was observed when compared to the bulk.

Dosev D. *et al.*[16] (2006): *Photoluminescence of Eu^{3+}:Y_2O_3 as an indication of crystal structure and particle size in nanoparticles synthesized by flame spray pyrolysis*

- Eu^{3+}-doped Y_2O_3 nanocrystals were synthesized by a flame spray pyrolysis. Within a single batch of the nanocrystals, the size of nanocrystals varied in the range 5 - 200 nm. These nanocrystals were separated by centrifugation into two size groups (5 50 nm and 50 200 nm), each characterized by luminescence spectroscopy and X-ray diffraction. The nanocrystals larger than about 50 nm were of the cubic phase of the Y_2O_3. The nanocrystals smaller than about 50 nm had mix phases of the cubic and monoclinic structures.

The scientific community focused their attention primarily on developing techniques to produce rare-earth oxide nanocrystals and studying their optical properties. It is also important to assemble these nanocrystals into films and study their optical properties because the potential applications for these materials comprise video display and X-ray intensifying screens, and coatings for the fluorescent lamps. Electrophoretic deposition (EPD) is a promising technique to manipulate and assemble nanocrystals into densely-packed homogeneous and smooth films.[17] It is essential to have well-dispersed and stable suspension of the nanocrystals to produce homogeneous films, for which nanocrystal surface passivation is essential. Of all the available nanocrystal synthesis techniques, the synthesis technique developed by Wakefield *et al.* produces the nanocrystals capped with ligands such as TOPO.[3] We attempted to produce homogeneous films of the Eu_2O_3 nanocrystals produced with this technique. Our early efforts to produce homogeneous films of these nanocrystals were unsuccessful because the films were formed of micron-size agglomerates of the Eu_2O_3 nanocrystals.[18] Hence, a new versatile synthesis technique was required to produce the cubic phase rare-earth oxide nanocrystals (isotropic), capped with ligands. The nanocrystals produced by this technique should be colloidally stable and the surface should be well passivated so that homogeneous films can be deposited. Since this dissertation explores the properties of films of the rare-earth oxide nanocrystals, the development of a nanocrystal

technique that facilitates production of homogeneous films is very important.

This dissertation explores synthesis of the rare-earth oxide nanocrystals, their assembly into films, and investigates of their optical and dielectric properties. Outline of this dissertation is as follows:

This chapter has introduced rare-earth oxide materials, which are of technological importance and has listed their widespread applications. In particular, the optical characteristics of the rare-earth sesquioxides (RE_2O_3; defined as rare-earth oxide in this dissertation) have been introduced. Important optical properties of Eu_2O_3, Tb_2O_3, Y_2O_3, and Gd_2O_3 were highlighted. The chapter outlined research accomplished by scientific community to produce nanocrystals of these oxides and to understand their optical properties. Prior to describe the research conducted on these oxides, it is essential to understand properties of these materials in detail. Different crystal structures of Eu_2O_3, Gd_2O_3, and Tb_2O_3 are explained in this chapter. To understand the origin of the optical properties of these oxides, different processes such as excitation transition, emission transitions, and energy transfer are discussed. Also, the dielectric properties of these oxides are listed.

Chapter II describes a new colloidal synthesis procedure that was developed to produce ultra-small Eu_2O_3, Tb_2O_3, and Eu^{3+}-doped Gd_2O_3 nanocrystals. It includes results of various materials characterization techniques that were employed during the development of the nanocrystals. Results of the optical studies of these nanocrystals are discussed.

Chapter III provides a brief overview of electrophoretic deposition, which is a particle assembly technique. It includes fundamentals of the deposition technique and lists various deposition parameters. It describes concisely the long existing and well-known EPD technique that employs polar solvents. It introduces a relatively new EPD technique that employs non-polar solvents. Details of the EPD experiments performed in this research are discussed.

Chapter IV describes an assembly of the Eu_2O_3 nanocrystals into transparent and luminescent films using EPD. Results of the optical characterization of these films

are discussed. Effect of the EPD parameters on growth of uniform films of the Eu_2O_3 nanocrystals is explored.

Chapter V explores dielectric properties of the Gd_2O_3 nanocrystals, which are assembled into films via EPD. It includes results of the materials characterization techniques employed to characterize the films of the Gd_2O_3 nanocrystals, and includes analysis of these results. Results of the electrical characterization of these films, performed to study their dielectric properties, are discussed.

Chapter VI describes the development of layered architectures of carbon nanotubes and nanocrystals using different EPD techniques. These heterostructures were characterized with different materials and electrical characterization techniques and those results are discussed here.

Chapter VII summarizes the research conducted in this dissertation.

1.2 Rare-earth oxides

Rare-earth oxides exhibit polymorphism with five distinct polymorphs, designated as A, B, C, H, and X. Goldschmidt *et al.* observed the A-, B-, and C-type polymorphs below approximately 2000 °C,[19] while the H- and X-type polymorphs were formed above this temperature.[20,21] The thermal stabilities of these five polymorph types at atmospheric pressure are represented in figure 1.4 for different REOs.[20] For example, the order of transition for Eu_2O_3 is C $\rightarrow$ B $\rightarrow$ A $\rightarrow$ H $\rightarrow$ X with the increasing temperature . The C-type polymorph of Eu_2O_3 changes to the B-type polymorph at around 1100 °C and then to the A-type polymorph at about 2040 °C. When the A-type polymorph is heated further, it transforms to the H-type polymorph at around 2140 °C and then to the X-type polymorph at about 2280 °C. Further, the X-type polymorph melts at around 2340 °C. Of these polymorphs of REOs, the crystal structures of the A-, B-, and C-type polymorphs are well characterized.

The A-type polymorph of REOs has the hexagonal crystal structure with the space

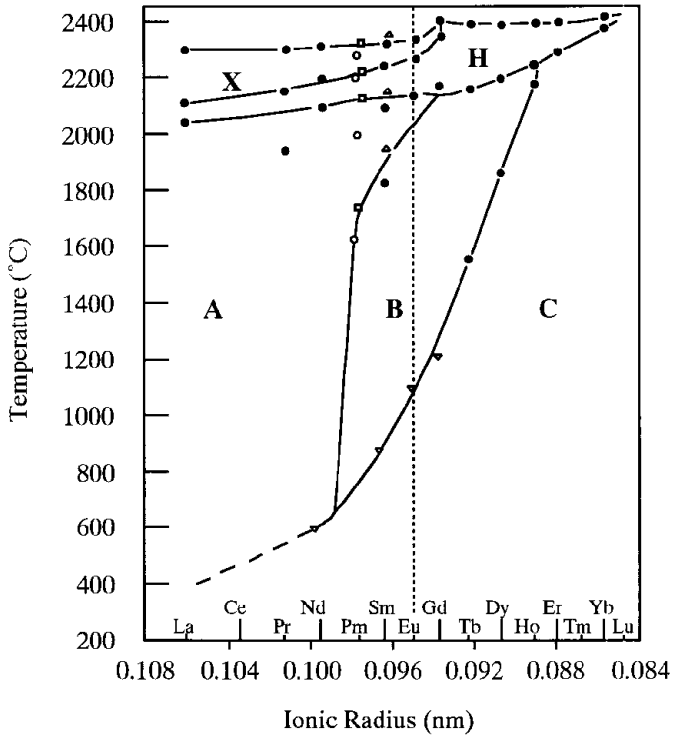

Figure 1.4: Polymorphic transformation for the lanthanoid sesquioxides. After Foëx M. *et al.*[20]

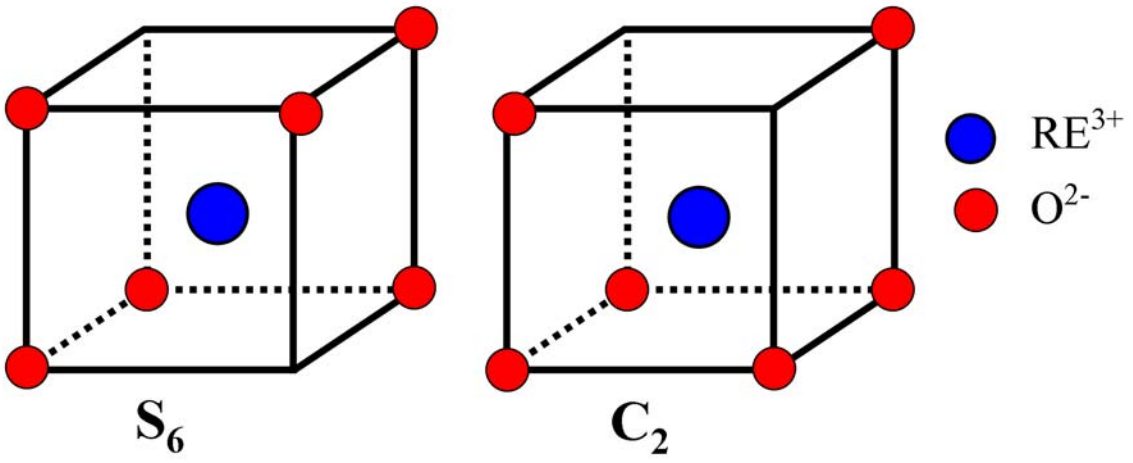

Figure 1.5: Schematic of lattice sites in the C-type rare-earth oxides with two types of symmetry (C_2 and S_6). Of the 32 RE^{3+} ions, 24 ions occupy the lattice sites with C_2 symmetry, and eight ions occupy the sites with S_6 symmetry.

group $P32/m$ and has one formula (RE_2O_3) per unit cell.[22,23] The coordination number of RE ions is seven with four oxygen ions closer than the other three. The B-type polymorph has the monoclinic crystal structure with the space group $C2/m$ and has six formulae (RE_2O_3) per unit cell.[24,25] The coordination numbers of RE ions are six and seven. The C-type polymorph has the cubic crystal structure, like Bixbyite mineral [$(Fe,Mn)_2O_3$], with the space group $Ia\overline{3}$. The coordination number of RE ions is six. The unit cell comprises sixteen formulae of RE_2O_3; 32 RE ions and 48 oxygen ions per unit cell.[26] The RE^{3+} ions occupy lattice sites with two symmetry types; C_2 symmetry and C_{3i} (S_6) symmetry, as shown in figure 1.5. Of the 32 RE^{3+} ions, 24 ions occupy the lattice sites with C_2 symmetry, and eight occupy the sites with C_{3i} (S_6) symmetry. The C_2 symmetry site lacks inversion symmetry and the S_6 symmetry site has inversion symmetry.

The B- and C-type polymorphs of the europium oxide, gadolinium oxide, and terbium oxide are formed at atmospheric pressure and below the temperature of approximately 2000 °C. The unit cell parameters of these oxides in the two polymorphs are listed in Table 1.2 (a, b, c, and β for monoclinic and a for cubic). The C-type polymorph is stable at

Table 1.2: Lattice parameters of the Eu_2O_3, Gd_2O_3, and Tb_2O_3 polymorphs.[27]

Oxides	Crystal structure	a (nm)	b (nm)	c (nm)	β
B-type Eu_2O_3	monoclinic	1.411	0.360	0.880	100.05 °
B-type Gd_2O_3	monoclinic	1.406	0.356	0.876	100.10 °
B-type Tb_2O_3	monoclinic	1.404	0.354	0.872	100.06 °
C-type Eu_2O_3	cubic	1.086	-	-	-
C-type Gd_2O_3	cubic	1.081	-	-	-
C-type Tb_2O_3	cubic	1.073	-	-	-

atmospheric pressure and at low-temperatures. This dissertation explores the development of the C-type Eu_2O_3, Gd_2O_3, and Tb_2O_3 nanocrystals.

1.3 Optical properties

Luminescence from the europium oxide, gadolinium oxide, and terbium oxide is observed only when these oxides absorb the excitation energy. To understand the origin of luminescence in these materials, it is essential to have knowledge of the underlying absorption, emission, non-radiative transitions, which are discussed in the following sections.

1.3.1 Excitation transitions

The energy level diagram of a REO provides a clear picture of how the excitation energy is absorbed. Figure 1.6 shows a schematic energy level diagram of a REO exhibiting three excitation transitions: (a) $4f$-$4f$ transitions, (b) $4f$-$5d$ transitions, and (c) charge-transfer state (CTS) transitions.

$4f$-$4f$ transitions

In the $4f$-$4f$ transitions, electrons are transferred between different energy levels of the $4f$ orbital of the same RE^{3+} ion. These transitions are actually forbidden by the parity selection rule, which states that electronic transitions between energy levels with the same parity can not occur. Since energy levels within the $4f$ orbital have same parity, the $4f$-$4f$ electronic transitions are forbidden. In reality, these transitions occur in the rare-earth

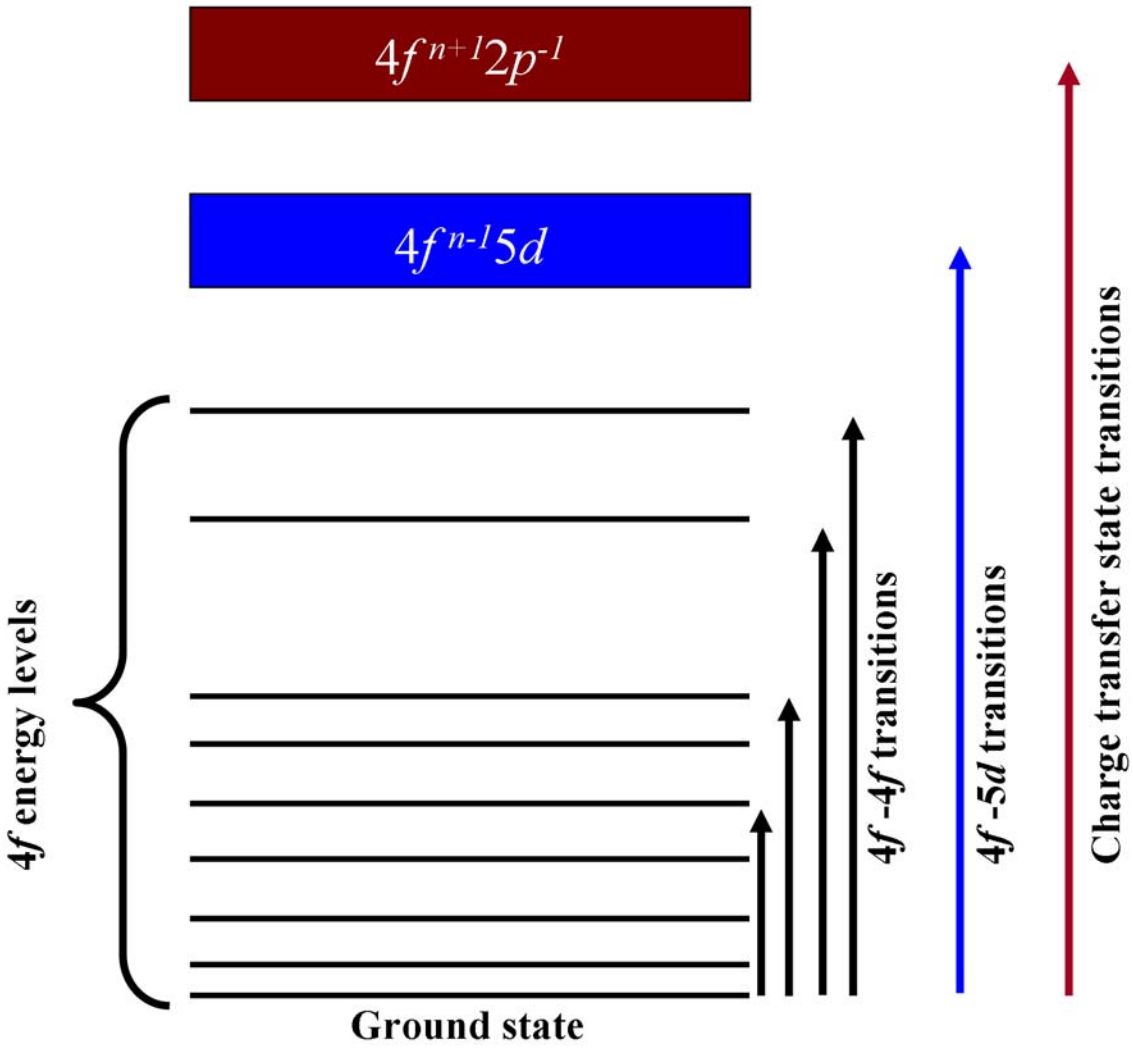

Figure 1.6: Excitation transitions are represented in an energy level diagram of a rare-earth oxide. $4f$-$4f$ transitions are forbidden by the parity selection rule, but occur because of relaxation of the parity selection rule. Occupation of RE^{3+} ion in a lattice site, which lacks inversion symmetry (C_2) is responsible for relaxation of the parity selection rule. The absorption peaks resulting from these transitions are narrow and weak. In $4f$-$5d$ transitions, one of the $4f$ electrons is transferred to a higher energy level in $5d$ orbital within the same RE^{3+} ion. In charge-transfer state transitions, one of the $2p$ electrons of the surrounding O^{2-} ion is excited to a higher energy level in $4f$ orbital of the RE^{3+} ion. The absorption peaks resulting from the $4f$-$5d$ and charge-transfer state transitions are broad and intense.

oxides because the parity selection rule is relaxed due to perturbations such as electron-vibration coupling and uneven crystal-field terms. The electron-vibration coupling has a small influence on the relaxation of parity selection rule.[28] More importantly, the uneven crystal-field terms, which are present as a result of the occupation of RE ion in a lattice site without inversion symmetry (C_2), are responsible for the relaxation of the parity selection rule. A small amount of opposite-parity wave functions (like $5d$, charge-transfer states) are mixed with the $4f$ wave functions because of these uneven crystal-field terms. Thus, the forbidden $4f$-$4f$ transitions occur in the rare-earth oxides. However, absorption peaks resulting from these transitions are very narrow and weak.

$4f$-$5d$ transitions

In $4f$-$5d$ transitions, one of the $4f$ electrons is transferred to a higher energy level in $5d$ orbital within the same RE^{3+} ion. These transitions are represented as $4f^n \rightarrow 4f^{n-1}5d$. Unlike $4f$-$4f$ transitions, these electronic transitions are allowed and are observed as broad and strong peaks in the absorption spectra. Between the three rare-earth oxides (Eu_2O_3, Gd_2O_3, and Tb_2O_3), Tb_2O_3 has lowest $4f$-$5d$ transition energy, which is explained by the electronic configuration of the Tb^{3+} ion ($4f^8$). An empty or a half-filled or a completely filled electron shell is a very stable configuration. Since Tb^{3+} ion ($4f^8$) has one electron excess of the half-filled configuration ($4f^7$), the excess electron is readily transferred to the $5d$ orbital. Hence, the $4f$-$5d$ transitions occur at the lower energy in Tb_2O_3 compared to Eu_2O_3 and Gd_2O_3.

Charge-transfer state transitions

In charge-transfer state transitions, one of the $2p$ electrons of the surrounding O^{2-} ion is excited to a higher energy level in $4f$ orbital of the RE^{3+} ion. These transitions are represented as $4f^n \rightarrow 4f^{n+1}2p^{-1}$. Similar to the $4f$-$5d$ transitions, these electronic transitions are also allowed and are present as broad and intense peaks in the absorption spectra. Eu_2O_3 has the lowest CTS transition energy between the three rare-earth oxides

(Eu_2O_3, Gd_2O_3, and Tb_2O_3). Since Eu^{3+} ions ($4f^6$) has one electron less than the half-filled configuration ($4f^7$), the $4f$ orbital of Eu^{3+} ion readily accepts an electron from the $2p$ orbital of the neighboring oxygen ion. Hence, the charge-transfer transitions occur at the lower energy in Eu_2O_3 compared to Gd_2O_3 and Tb_2O_3.

Based on the discussion of different excitation transitions in the rare-earth oxides, it is clear that the excitation energy is absorbed efficiently via two types of transitions: $4f$-$5d$ transitions and charge-transfer state transitions. The absorption bands corresponding to the CTS transitions of Eu_2O_3 and the $4f$-$5d$ transitions of Tb_2O_3 are in the UV region. The UV radiation ($\sim$ 254 nm) is the minimum energy radiation that excites the ions efficiently and is employed to excite the rare-earth oxide nanocrystals explored in this dissertation. However, these oxides can also be excited with higher energy irradiations by fast electrons, X-rays, and γ-rays.

1.3.2 Emission transitions

Upon absorption of the excitation energy, electrons are transferred to the higher energy levels as described in the earlier section and then, they return to the ground state via non-radiative and/or radiative transitions. Radiative transitions are known as emission transitions, which are discussed in this section. Emission transitions in the rare-earth oxides (Eu_2O_3, Gd_2O_3, and Tb_2O_3) are characteristic of the $4f$-$4f$ transitions within the Eu^{3+}, Gd^{3+}, and Tb^{3+} ions, respectively. Since the $4f$ orbitals in these ions are shielded by the $5s$ and $5p$ orbitals, the influence of lattice (surrounding crystallographic environment) on the energy levels of the RE^{3+} ions and therefore, on the emission transitions is small, but very important. Here, we discuss the emission transitions of the three oxides (Eu_2O_3, Gd_2O_3, and Tb_2O_3) based on their energy level diagrams.

Eu_2O_3

Figure 1.7 shows the energy level diagram of the Eu_2O_3, where $^7F_0$ is the ground state.[29,30] The electrons excited into the CTS, transit non-radiatively to occupy various ^5D

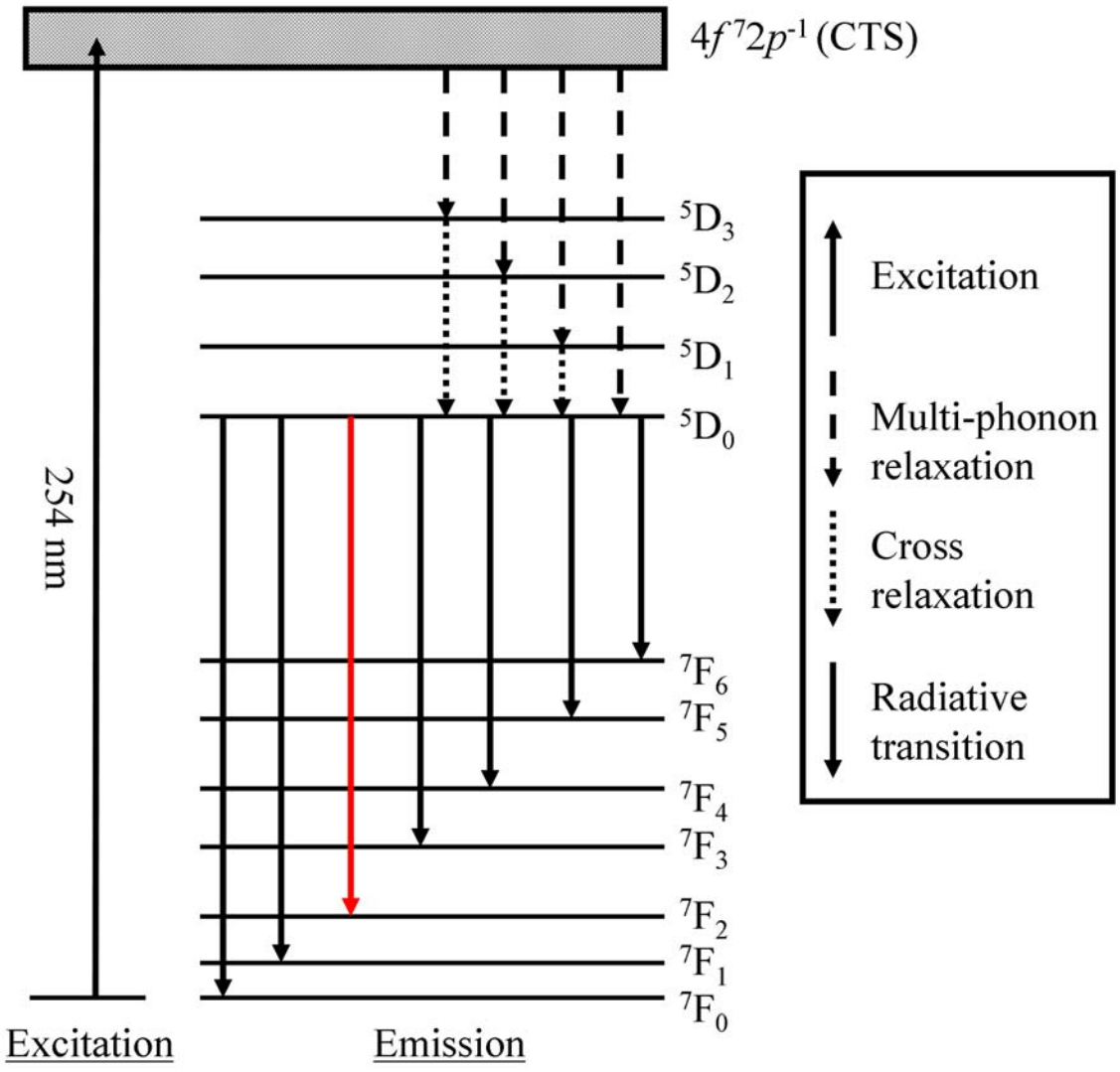

Figure 1.7: Schematic energy level diagram of Eu_2O_3 showing emission transitions. The electrons excited into the CTS transit non-radiatively to occupy various ^{5}D levels (^5D_J, J = 0, 1, 2, 3). The electrons from the high ^{5}D levels (^5D_J, J > 0) transfer to the $^5D_0$ level by cross-relaxation and populate the $^5D_0$ energy level. Further, these electrons transit radiatively to the ^{7}F energy levels (^7F_J, J = 0 - 6). Typically, the $^5D_0 \rightarrow {}^7F_2$ transition dominates over the other transitions. The energy of this transition corresponds to the red emission color ($\sim$ 611 nm), which is characteristic of the Eu^{3+} ions.

levels (^5D_J, J = 0, 1, 2, 3). The electrons from the high ^5D levels (^5D_J, J > 0) transfer to the $^5D_0$ level by cross-relaxation mechanism (Section 1.3.4) and populate the $^5D_0$ energy level. Further, these electrons transit radiatively to the ^7F energy levels (^7F_J, J = 0, 1, 2, 3, 4, 5, 6). The above transitions are of two types, magnetic-dipole transitions and electric-dipole transitions. The magnetic-dipole transitions are subject to the selection rule $\Delta J = 0, \pm 1$ ($J = 0 \rightarrow J = 0$ is forbidden). Electric-dipole transitions between $4f$ levels of Eu^{3+} ions are strictly prohibited because of the parity selection rule. However, this rule is relaxed because of the influence of the lattice. As described earlier (Section 1.2), Eu^{3+} ions occupy lattice sites with the two different symmetry types in C-type Eu_2O_3: S_6 symmetry site that has inversion symmetry and C_2 symmetry site that lacks inversion symmetry (Figure 1.5). The absence of inversion symmetry at C_2 symmetry site is responsible for the presence of uneven crystal-field terms, because of which, the odd parity wave functions (CTS) are mixed with the $4f$ wave functions. Thus, the parity selection rule is relaxed and the electric-dipole transitions are possible only within the Eu^{3+} ions that occupy lattice sites with C_2 symmetry. These transitions are known as forced electric-dipole transitions within rare-earth scientific community and are subject to the selection rule. Since J = 0 for the initial energy level, ΔJ = 2, 4, and 6. The forced electric-dipole transitions do not occur within the Eu^{3+} ions occupying the lattice site with S_6 symmetry because of inversion symmetry and only the magnetic-dipole transition $^5D_0 \rightarrow {}^7F_1$ is possible. In addition to the forced electric-dipole transitions [$^5D_0 \rightarrow {}^7F_J$, (J = 2, 4, 6)] and the magnetic-dipole transitions [$^5D_0 \rightarrow {}^7F_1$], the following transitions [$^5D_0 \rightarrow {}^7F_J$, (J = 0, 3, 5)] are present,[31] but have very low intensity. The radiative transitions $^5D_0 \rightarrow {}^7F_J$, (J = 0, 1, 2, 3, 4) are observed as the emission peaks in the visible spectral region. Typically, the $^5D_0 \rightarrow {}^7F_2$ transition dominates over the other transitions. The energy of this transition corresponds to the red emission color ($\sim$ 611 nm), which is characteristic of the Eu^{3+} ions.

The energy levels of Eu^{3+} ions, exhibited in figure 1.7, are actually split into multiple energy manifolds (not shown in figure 1.7) by the crystal field (crystal-field splitting) when

the ions occupy a crystalline host lattice. The splitting of the $4f$ energy levels is small because the $4f$ electrons are shielded from the surrounding crystallographic environment by the $5s^2$ and $5p^6$ electrons. An energy level with J = 0 is a single, non-degenerate state, which can not be split. The $^5D_0$ level is not split by the crystal field (J = 0), but the crystal-field splitting of the ^7F levels occurs. The number of these crystal-field-split energy manifolds depends on the crystallographic symmetry at the location of Eu^{3+} ion. The transitions with $\Delta J = 0, \pm 2$ are hypersensitive to this effect. Since the starting energy level has J = 0, the $^5D_0 \rightarrow {}^7F_2$ transition is a hypersensitive transition. This hypersensitive $^5D_0 \rightarrow {}^7F_2$ transition distinctly exhibits these multiple energy manifolds as the multiple emission peaks in the luminescence spectrum.

Tb_2O_3

Figure 1.8 shows the energy level diagram of the Tb_2O_3, where $^7F_6$ is the ground state.[29,30] The electrons excited into the $4f$-$5d$ state, transfer non-radiatively to occupy $^5D_3$ and $^5D_4$ energy levels. The electrons from the higher $^5D_3$ level transit to the $^5D_4$ level by cross-relaxation mechanism (Section 1.3.4). The $^5D_4$ energy level is populated at the expense of $^5D_4$. These electrons transit radiatively to the ^7F energy levels (^7F_J, J = 6, 5, 4, 3, 2, 1, 0). Similar to the Eu^{3+}, the forced electric-dipole transitions are present within the Tb^{3+} ions because they occupy lattice sites that lack inversion symmetry (C_2). The forced electric-dipole and magnetic-dipole transitions are present in Tb_2O_3. Of the emission transitions, $^5D_4 \rightarrow {}^7F_5$ is the dominant transition. The energy of this transition corresponds to the green emission ($\sim$ 542 nm), which is characteristic of the Tb^{3+} ions. For the majority of the transitions, the J values of involved energy levels are non-zero. These energy levels can be split into multiple manifolds by the crystal field (not shown in figure 1.8), which are observed as multiple peaks in the luminescence spectrum.

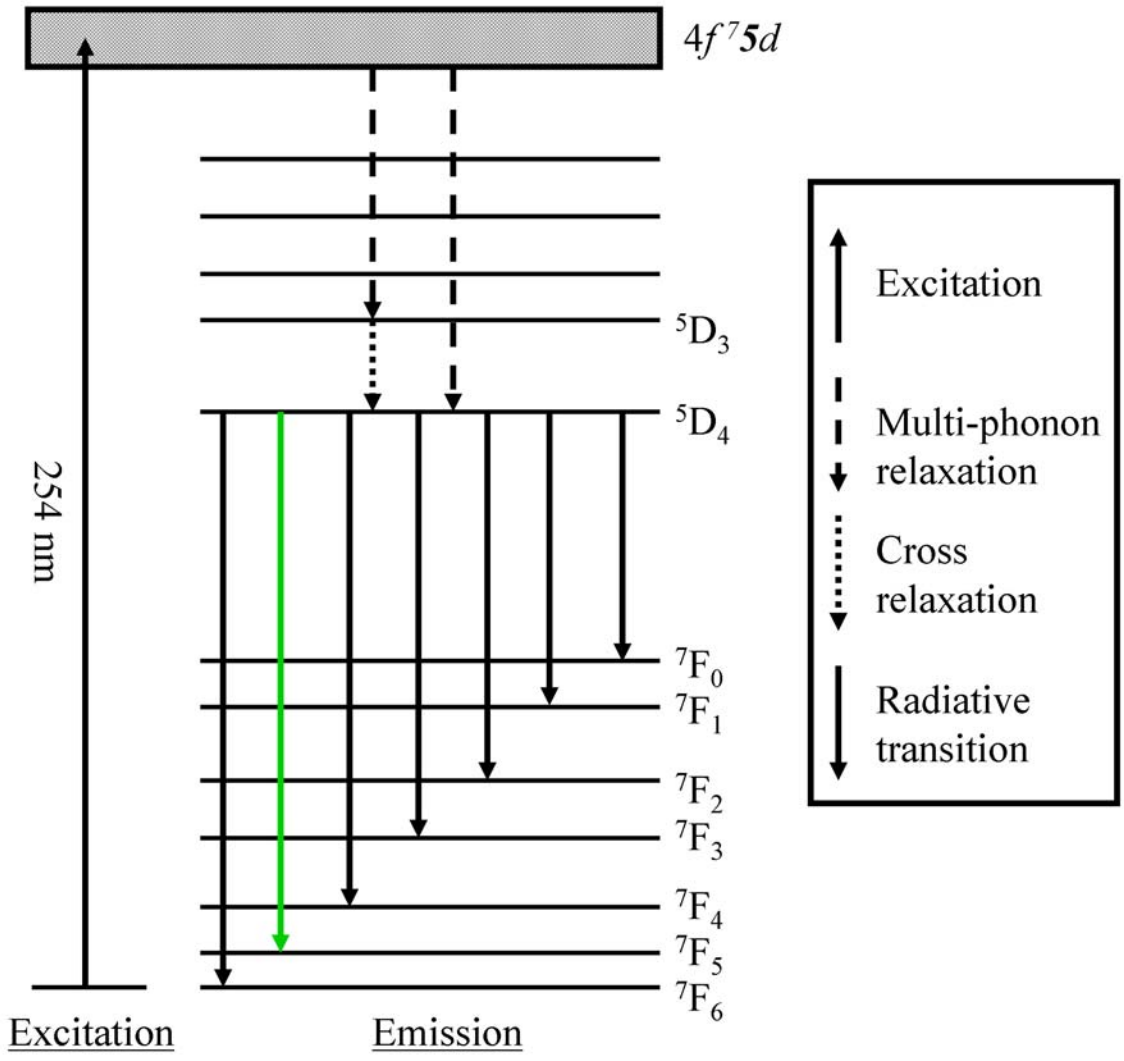

Figure 1.8: Schematic energy level diagram of Tb_2O_3 with emission transitions. The electrons excited into the $4f$-$5d$ state, transfer non-radiatively to occupy $^5D_3$ and $^5D_4$ energy levels. The electrons from the higher $^5D_3$ level transit to the $^5D_4$ level by cross-relaxation mechanism (Section 1.3.4). The $^5D_4$ energy level is populated at the expense of $^5D_4$. These electrons transfer radiatively to the ^7F energy levels (^7F_J, J = 6, 5, 4, 3, 2, 1, 0). The $^5D_4$ $\rightarrow$ $^7F_5$ is the dominant transition, which corresponds to the green emission color ($\sim$ 542 nm) in visible spectrum. Green color is characteristic of the Tb^{3+} ions.

Gd_2O_3

The Gd^{3+} ion has a very stable electronic configuration $4f^7$, which is a half-filled $4f$ shell. Compared to Eu_2O_3 and Tb_2O_3, Gd_2O_3 requires more energy to excite an electron from the ground state of Gd^{3+} ion to the $4f$-$5d$ state or to accept an electron into the $4f$ orbital of Gd^{3+} ion from the $2p$ orbital of the oxygen ion. Figure 1.9 shows the energy level diagram of the Gd_2O_3, where $^8S_{7/2}$ is the ground state.[29,30] The UV (254 nm) radiation does not correspond to any excitation transition and thus, cannot be employed to excite Gd_2O_3. The higher energy UV radiation, fast electrons, X-rays, and γ-rays can excite Gd_2O_3. The lowest-energy emission transition ($^6P_{7/2} \rightarrow {}^8S_{7/2}$) corresponds to an emission peak in UV ($\sim$ 313 nm) region. Hence, Gd_2O_3 is not employed as a luminescent material. However, it is used as a host for luminescent material (Gd_2O_3:Eu^{3+}/Gd_2O_3:Tb^{3+}).

1.3.3 Non-radiative transition

The electrons transferred into the excited state upon absorption of excitation energy can return to a lower energy level or the ground state without emission of radiation. Such a transition is called non-radiative transition. If the energy difference between the levels is equal to or less than about 5 times the highest vibrational frequency of the host lattice, the energy can excite multiple phonon (high energy vibrations) simultaneously. This transition is called multi-phonon relaxation. Thus, the excitation energy is given up as heat to the host lattice. Such a non-radiative transition is observed in the rare-earth oxides discussed earlier (Eu_2O_3, Gd_2O_3, and Tb_2O_3).

1.3.4 Energy transfer: origin of concentration quenching

When the excitation energy is absorbed by the system (e.g. Eu_2O_3 and Tb_2O_3), all the Eu^{3+}/Tb^{3+} ions within the system do not absorb the energy. The ions that absorb the excitation energy are in the excited state, but the energy is not confined to those ions (excited state). The excitation energy can be transferred from one Eu^{3+}/Tb^{3+} ion

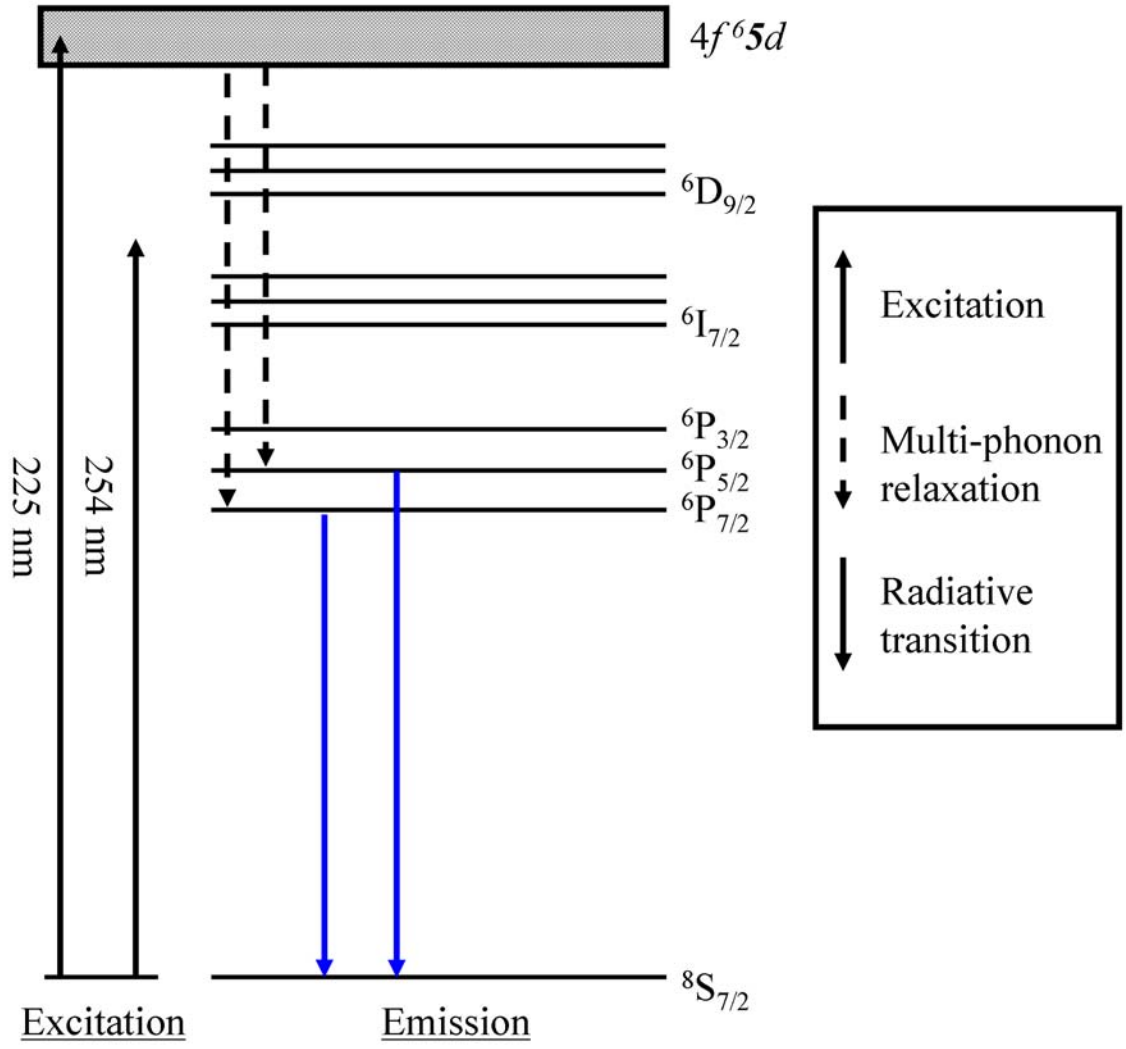

Figure 1.9: Schematic energy level diagram of Gd_2O_3 with emission transitions. The lowest-energy emission transition ($^6P_{7/2} \rightarrow {}^8S_{7/2}$) corresponds to an emission peak in UV ($\sim$ 313 nm) region.

(excited state) to the other Eu^{3+}/Tb^{3+} ion (ground state). Energy transfer between the two ions is possible only if (a) the energy differences between the ground state and excited state of the two ions are equal, which is known as energy resonance and (b) a suitable interaction between the two ions is present. The interaction between the two ions may be of exchange type (overlap of wave functions) or an electric or magnetic multipolar type. The electric multipolar interaction is strong if the electric-multipole transitions are allowed. Since the electric-dipole transitions within the $4f$ energy levels of Eu^{3+}/Tb^{3+} ions are forced, but not allowed, the multipolar interactions are weak. Energy transfer between the Eu^{3+}/Tb^{3+} ions is possible only if the exchange interaction is strong. The strength of the exchange interaction is influenced by the distance between the ions. Typically, the exchange interaction is effective when the distance between the ions is shorter than 5-8 $\mathring{A}$. At high concentration of the ions (e.g. Eu_2O_3 and Tb_2O_3), the distance between them is short. Since the two identical Eu^{3+}/Tb^{3+} ions fulfill the energy resonance criterion and the exchange interaction is effective, the energy transfer occurs. Considering the long radiative lifetimes ($\sim$ 1 ms) of Eu^{3+} and Tb^{3+} ions, the energy transfer can occur multiple times. The excitation energy can relocate far away from the original location where it was absorbed, which is called energy migration. If the excitation energy migrates to a defect or impurity site where it is lost non-radiatively, the radiative emission (luminescence) is quenched. This process leads to reduction in the luminescence efficiency. This phenomenon is defined as concentration-dependent luminescence quenching or concentration quenching. A schematic of the energy migration process that leads to concentration quenching is shown in figure 1.10.

The Eu^{3+}/Tb^{3+}-doped RE_2O_3 is preferred over the pure Eu_2O_3/Tb_2O_3 for their higher luminescence efficiency. Common host lattices are Y_2O_3 (lattice constant = 10.60 $\mathring{A}$, space group: $Ia\overline{3}$) and Gd_2O_3 (lattice constant: 10.81 $\mathring{A}$, space group: $Ia\overline{3}$). The crystal structure of these host lattices is identical to that of Eu_2O_3 and Tb_2O_3. Typically, Y_2O_3 is employed because yttrium (Y) is abundant compared to gadolinium (Gd). Reducing

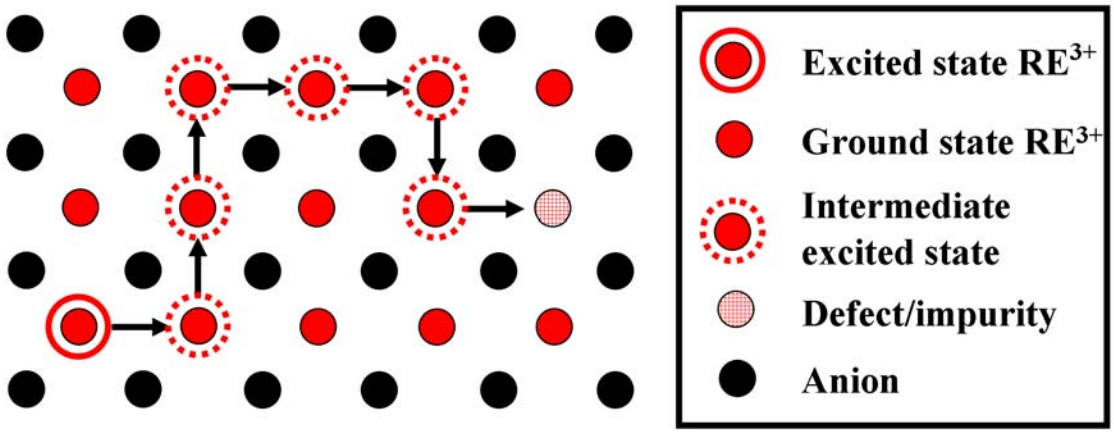

Figure 1.10: Schematic of excitation migration mechanism.

the concentration of luminescent ions minimizes the exchange interaction between them. For example, all lattice sites occupying RE^{3+} ions are filled by Eu^{3+} ions in pure Eu_2O_3. In contrast, $10\%Eu^{3+}$:Gd_2O_3 has only 10% of the RE^{3+} ion occupying lattice sites filled by Eu^{3+} ions. The Eu^{3+} ions occupy these lattice sites in a statistical way. Hence, the Eu^{3+}-Eu^{3+} distance increases as the Eu^{3+} ion concentration decreases, which minimizes the exchange interaction between them at low concentration. The excitation energy migration is reduced and it is confined to the ion where it was absorbed. Thus, the luminescence efficiency is increased.

Low concentration of luminescent ions is required to enhance the luminescence efficiency, but a certain concentration should be employed to quench higher energy-level emission transitions by cross-relaxation. In cross-relaxation, a part of the excitation energy of one luminescent ion is transferred to another identical luminescent ion via phonon-assisted energy transfer. Cross-relaxation is the preferred energy transfer mechanism because certain higher energy level emission transitions are quenched at the expense of lower energy level excitation transitions, which can be easily explained for Eu^{3+} and Tb^{3+} ions. Figure 1.11 shows cross-relaxation process using the energy level diagrams of Eu^{3+} and Tb^{3+} ions. For example, the $^5D_1 \rightarrow {}^5D_0$ emission transition is quenched in one Eu^{3+} ion at the

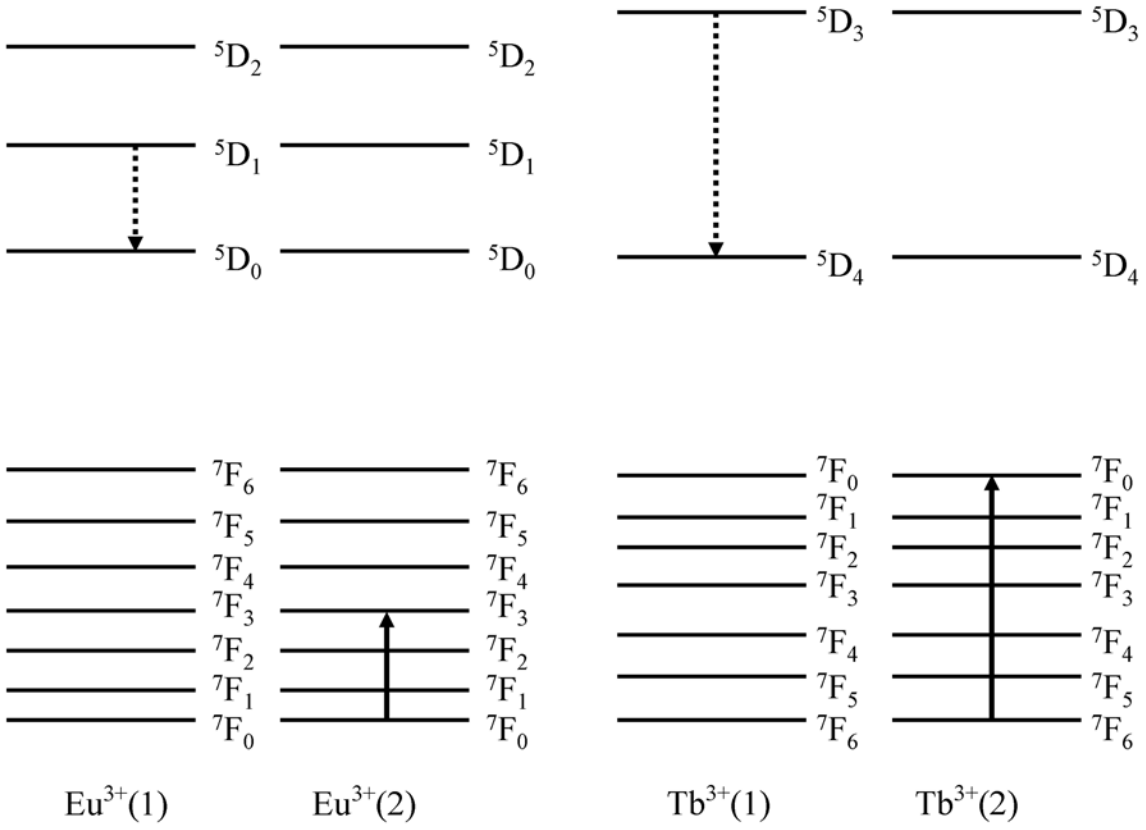

Figure 1.11: Schematic of cross-relaxation mechanism in Eu^{3+} and Tb^{3+} ions. The $^5D_1 \rightarrow {}^5D_0$ emission transition is quenched in one Eu^{3+} ion at the expense of the $^7F_0 \rightarrow {}^7F_3$ excitation transition in another Eu^{3+} ion. Similarly, the $^5D_3 \rightarrow {}^5D_4$ emission transition is quenched in one Tb^{3+} ion at the expense of the $^7F_6 \rightarrow {}^7F_0$ excitation transition in another Tb^{3+} ion.

expense of the $^7F_0 \rightarrow {}^7F_3$ excitation transition in another Eu^{3+} ion. Such transitions are preferred because electrons are populated at the $^5D_0$ energy level and emission transitions from the higher energy level [$^5D_1 \rightarrow {}^7F_J$ (J = 0-6)] are avoided. Similarly, the $^5D_3 \rightarrow {}^5D_4$ emission transition is quenched in one Tb^{3+} ion at the expense of the $^7F_6 \rightarrow {}^7F_0$ excitation transition in another Tb^{3+} ion. Thus, electrons are populated at the $^5D_4$ energy level and emission transitions from the higher energy level [$^5D_3 \rightarrow {}^7F_J$ (J = 6-0)] are avoided. The cross-relaxation is observed above a critical concentration of luminescent ions as it depends on the interaction between the luminescent ions. The critical concentration depends on the host lattice (3% Eu^{3+}-doped Y_2O_3).[5] Doping of the host lattice with the luminescent ions to the critical concentration is desired. Doping of the luminescent ions in the host lattice above the critical concentration results in lower luminescence efficiency as described earlier.

1.4 Dielectric properties

Apart from the luminescent characteristics of the rare-earth oxides, their excellent dielectric/insulating properties are well known. These oxides have large band gaps (E_g), which range between 3 - 6 eV.[32] Again, the $4f^n$ configuration of the RE^{3+} ions is responsible for their large band gaps. The dielectric constants of these oxides are high (κ = 7 - 20).[33] Also, these oxides have high electrical resistivity ($\rho = 10^{12}$ - 10^{15} Ωcm).[34] In addition, these oxides are thermodynamically stable with silicon, which avoids formation of silicides at high temperatures.[35] The band gaps of the rare-earth oxides (Eu_2O_3, Gd_2O_3, and Tb_2O_3) explored in this dissertation are $\sim$ 4.5 eV, $\sim$ 5.5 eV, and $\sim$ 3.8 eV, respectively. Since the $4f^7$ configuration of the Gd^{3+} ions is more stable than the configurations of the Eu^{3+} ions ($4f^6$) and Tb^{3+} ions ($4f^8$), the band gap of Gd_2O_3 is largest among the three rare-earth oxides. The dielectric constants of Eu_2O_3, Gd_2O_3, and Tb_2O_3 are $\sim$ 12, $\sim$ 14, and $\sim$ 13, respectively.

CHAPTER II

ULTRA-SMALL RARE-EARTH OXIDE NANOCRYSTALS: SYNTHESIS & CHARACTERIZATION

2.1 Introduction

The synthesis of rare-earth oxide nanocrystals is of interest to explore the effect of size on their optical properties. The synthesis of these nanocrystals is not only of scientific interest but also of technological importance for their potential applications in solid state light-emitting devices or as luminescent probes in immunoassays.[7,8] Over the past decade, nanocrystals of europium oxide (Eu_2O_3), terbium oxide (Tb_2O_3), and RE^{3+}-doped gadolinium or yttrium oxide (Gd_2O_3:RE^{3+}, Y_2O_3:RE^{3+}; RE = Eu, Tb, Er), have been synthesized via multiple approaches in a range of sizes (2-100 nm).[3,9,11,12,16,36–38] Various synthesis approaches include gas-phase condensation,[9] sol-lyophilization,[36] flame pyrolysis[16] and colloidal synthesis.[3,11,12,37,38] In the gas-phase condensation technique,[9] a continuous-wave CO_2 laser is used to vaporize the rare-earth oxide. These vapors condense upon collision with inert-gas molecules to form clusters that are collected on a cold finger. In flame-pyrolysis,[16] a dispersion of rare-earth nitrate in ethanol is sprayed through a nebulizer to form micron-size droplets, which are oxidized in a hydrogen diffusion flame. A cold finger is used to collect the nanocrystals. Both techniques produce nanocrystals that are generally polydisperse in size and are not well-dispersed in solvents. In sol-lyophilization method,[36] rare-earth hydroxide sols are produced, which are calcined at high temperatures to produce rare-earth oxide nanocrystals. In the colloidal precipitation method,[3,11] surface-passivated Eu_2O_3 and Tb_2O_3 nanocrystals were produced at room temperature within an alcohol environment. The dehydrating properties of alcohol facilitated formation of oxide instead of hydroxide. In the polyol method,[12,37] the nanocrystals were synthesized at high temper-

ature in a high boiling point alcohol (diethylene glycol) by colloidal precipitation. Both techniques employed a base (NaOH) for the precipitation of the nanocrystals. The amount of NaOH controlled the reaction yield as well as the luminescence efficiency of the nanocrystals. A time consuming dialysis procedure is required to purify the nanocrystals produced by these techniques. Recently, anisotropic nanostructures of rare-earth oxide, such as nanodisks and nanoplates, in the size range of 5-20 nm in diameter have been synthesized by decomposition of various RE-complexes in the presence of fatty acids as surface stabilizing agents in high boiling point solvents.[14,15,39,40] However, throughout the previous work, there has been a considerable challenge to produce monodisperse, ultra-small (sub-3 nm) nanocrystals. The nanocrystals in this size regime exhibit interesting optical properties considering their size approaches a few multiples of lattice constants (Eu_2O_3: 10.86 $\mathring{A}$, Gd_2O_3: 10.81 $\mathring{A}$, Tb_2O_3: 10.73 $\mathring{A}$).

In this chapter, the development of a two-stage hot-solution phase technique to synthesize monodisperse, colloidally stable sub-3 nm cubic phase Eu_2O_3, Tb_2O_3, and Gd_2O_3:Eu^{3+} nanocrystals is discussed. The addition of oleic acid, which was employed in this technique, provides control over the nanocrystal size within a small regime. The nanocrystals and respective precursors were characterized systematically with various meterials characterization techniques. Photoluminescence (PL) characteristics of these nanocrystals are investigated and the new optical features are discussed. The luminescence intensities of the Eu_2O_3 and Gd_2O_3:Eu^{3+} nanocrystals are compared to investigate concentration quenching effects.

The research described in this chapter has been published in the following journal articles:

- S. V. Mahajan and J. H. Dickerson, Synthesis of monodisperse sub-3 nm RE_2O_3 and Gd_2O_3:Eu^{3+} nanocrystals, *Nanotechnology*, **18** 325605, (2007)

- S. V. Mahajan and J. H. Dickerson, Optical studies of sub-3 nm Eu_2O_3 and Gd_2O_3:Eu^{3+} nanocrystals, *J. Alloys Compd.*, **488** 574, (2009)

2.2 Experimental details

A two-stage procedure was developed to synthesize colloidally stable, ultra-small rare-earth oxide nanocrystals with oleic acid as the surface capping ligand.[41] First, rare-earth oleate complex (RE-oleate) was prepared from commercially available chemicals. In the second stage, the nanocrystals were synthesized via the thermal decomposition of the RE-oleate complex in a high boiling point solvent.

2.2.1 Precursor preparation

Commercially available europium (III) chloride hexahydrate ($EuCl_3{\cdot}6H_2O$, 99.99%), terbium (III) chloride hexahydrate ($TbCl_3{\cdot}6H_2O$, 99.99%), gadolinium (III) chloride hexahydrate ($GdCl_3{\cdot}6H_2O$, 99.99%), and oleic acid ($CH_3(CH_2)_7CH{:}CH(CH_2)_7COOH$, 90% tech. grade) were purchased from Sigma-Aldrich. Sodium oleate ($C_{18}H_{33}O_2Na$, 95%) and tri-*n*-octylamine ($C_{24}H_{51}N$, 90.0%) were purchased from TCI America. All the chemicals were used as-received without further purification. The precursor preparation step was derived from a previously reported preparation of a Fe oleate precursor.[42] Figure 2.1(a) shows the experimental set-up of the precursor preparation stage. RE-(III) chloride hexahydrate (2 mM) and sodium oleate (6 mM) were mixed with ethanol (4 ml), de-ionized (DI) water (3 ml), and hexane (7 ml) in a round-bottom flask (25 ml). A water-cooled condenser was connected to the flask to condense vapors of ethanol and hexane during the reaction. The flask was immersed in a silicone oil bath, which was placed on a heating and stirring plate. The reaction mixture was heated to and maintained at ∼60-65 °C for 4 hours. A Teflon-coated magnetic stir bar stirred the mixture vigorously to achieve uniform distribution of reactants and temperature inside the flask. The reaction mixture became colorless and transparent as soon as the reactants dissolved completely (approximately within 10-15 min). Upon completion of the reaction, the flask was removed from the oil bath and was cooled in air. The reaction can be expressed as stated in equation 2.1.

$$RECl_3 \cdot 6H_2O + 3Na\text{-}oleate \overset{hexane,\, water,\, ethanol,\, 60^\circ C}{\longrightarrow} RE\text{-}(oleate)_3 + 3NaCl \qquad (2.1)$$

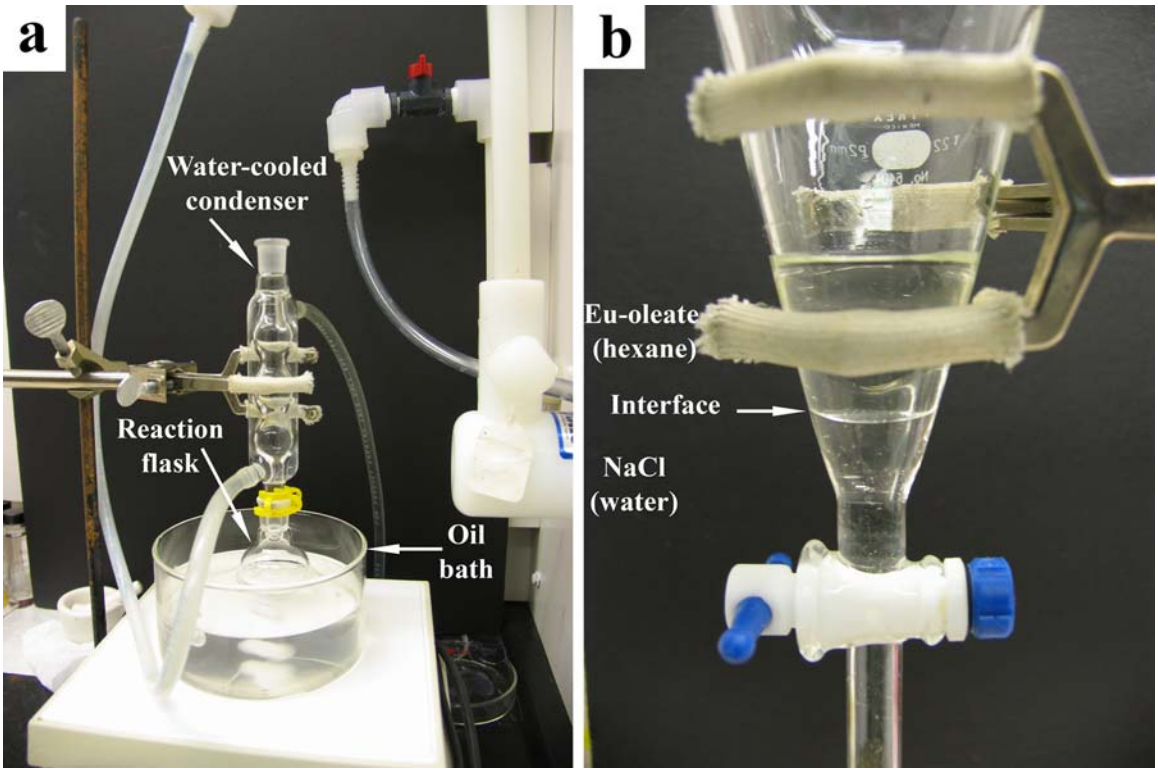

Figure 2.1: (a) Experimental set-up of the RE-oleate precursor preparation inside of a fume hood in air environment. A silicone oil bath, used to heat the reaction mixture, was kept on a heating & stirring plate. A round bottom flask, filled with the reaction mixture, was immersed into the oil bath. A stir bar inside the flask stirred the mixture vigorously to achieve uniform distribution of reactants and temperature in the flask. A water-cooled condenser facilitated condensation of hexane-ethanol vapors. (b) Precursor isolation was achieved using a separatory funnel. Since hexane and water are immiscible, they formed bi-layers. Water settled at the bottom because it is heavier than hexane. The RE-oleate complex was retained by removing water (NaCl).

To isolate the RE-oleate complex from the reaction mixture, the mixture was transferred to a separatory funnel. Since hexane and water are immiscible, they formed bi-layers. Water (H_2O) is heavier than hexane (C_6H_{14}), which settled at the bottom as seen in figure 2.1(b). The top hexane layer contained RE-oleate, and the bottom water-ethanol layer contained sodium chloride (NaCl). The bottom water layer was removed, and the top hexane layer, which contained RE-oleate complex, was retained. The RE-oleate complex was washed once with DI water to get rid of NaCl completely. The RE-oleate complex, suspended in hexane, was a colorless, transparent, viscous solution. This solution was divided into four glass vials (0.5 mM RE-oleate each) and was stored at room temperature in a dessicator. This RE-oleate complex was used as a standard precursor for the synthesis of the nanocrystals.

To prepare precursor for the synthesis of Gd_2O_3:Eu^{3+}(10%) nanocrystals, we employed 1:9 molar ratio of the europium (III) chloride hexahydrate and gadolinium (III) chloride hexahydrate, while keeping all the other parameters the same.

2.2.2 Nanocrystal synthesis

Synthesis of RE_2O_3 nanocrystals was performed in a glassware set-up under argon atmosphere using a Schlenk line as depicted in figure 2.2. The RE-oleate (0.5 mM) and oleic acid (0.25 mM) was mixed with 7 ml of tri-*n*-octylamine in a three-neck, round-bottom flask (25 ml). The flask was connected to a Schlenk line through a flash guard, which was used to safeguard the Schlenk line from becoming contaminated with reaction mixture during the degassing stage. The reaction flask was placed inside a heating mantle that was kept on a stir plate, and a thermocouple was inserted into the mixture. The thermocouple and heating mantle were connected to a digital temperature controller (Crouzet, CTD 46), which, in turn, connected to a power source to monitor and to control temperature precisely inside the reaction flask. A Pyrex-coated magnetic stir bar was used to stir the mixture vigorously to achieve uniform distribution of reactants. Since the flask was heated from the bottom,

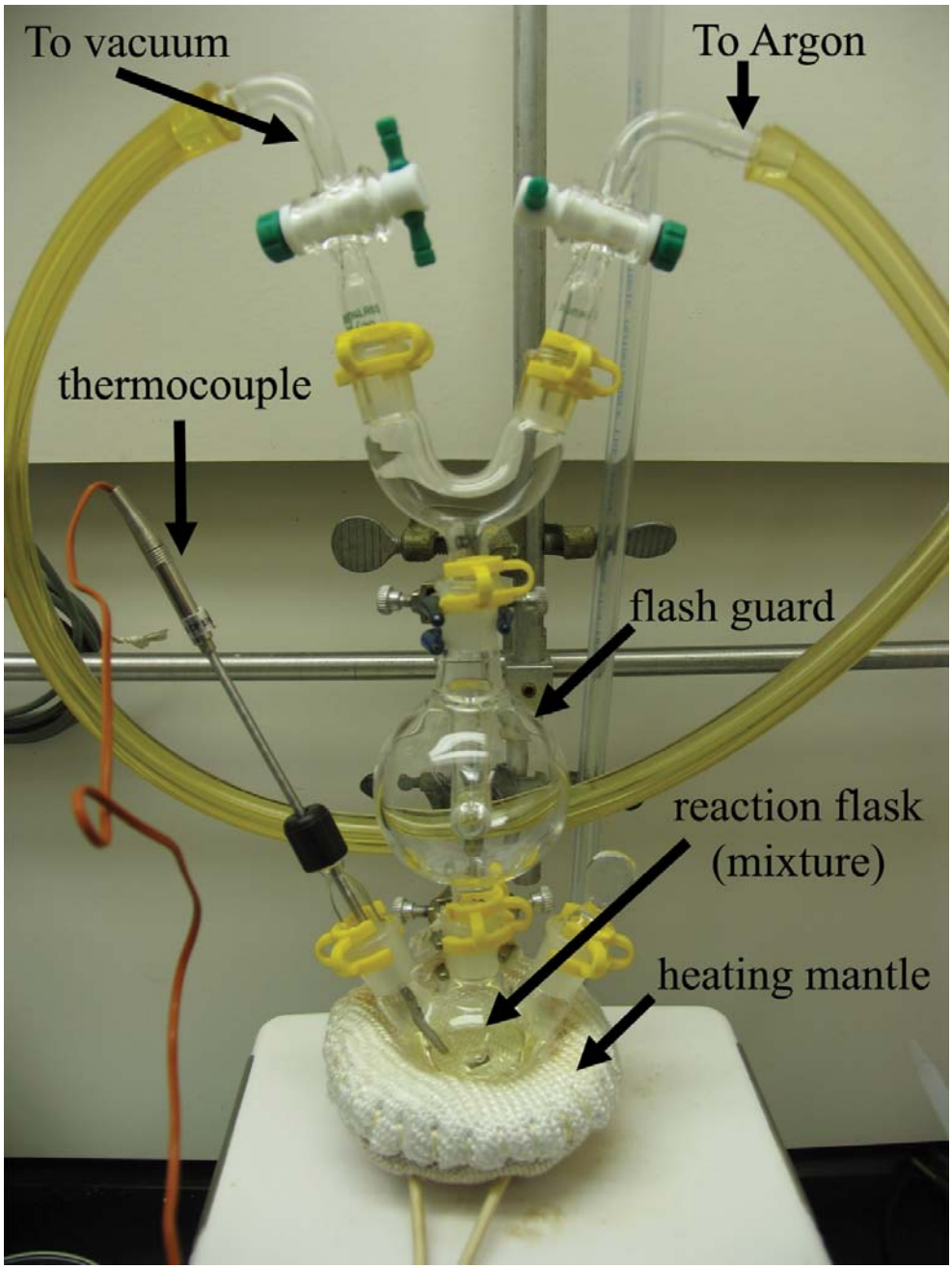

Figure 2.2: A glassware set-up for RE_2O_3 nanocrystal synthesis inside the fume hood using a Schlenk line under an Argon environment. A three-neck flask, filled with the reaction mixture, was placed inside a heating mantle on top a stir plate. A Pyrex-coated magnetic stir bar vigorously stirred the reaction mixture to maintain a uniform distribution of reactants and temperature. A thermocouple, inserted into the mixture, and a heating mantle were connected to a digital temperature controller to monitor and control temperature of mixture precisely.

uniform temperature was maintained by stirring the mixture. First, the mixture was put under vacuum (degassing) and purged with argon twice at room temperature to remove air. Next, the mixture was heated to and maintained at 100 °C for 30-45 min under vacuum to expedite the removal of moisture and hexane from the mixture. Next, the solution purged with argon and was heated to approximately 350 °C at an average rate of 5 °C min^{-1} under constant argon flux. The solution was maintained at this temperature for one hour. Upon completion of this stage, the flask (and solution) was cooled rapidly to room temperature using a burst of compressed air. The nanocrystal solution was stored in a glass vial in a dessicator. The nanocrystal synthesis can be expressed schematically as in equation 2.2.

$$RE\text{-}(oleate)_3 \overset{oleic\,acid,\,tri-n-octylamine,\,Ar,\,350^{\circ}C}{\longrightarrow} RE_2O_3\ nanocrystals \tag{2.2}$$

2.2.3 Nanocrystal cleaning

To isolate the nanocrystals from the reaction mixture, a sequential precipitation and centrifugation process was employed. The addition of ethanol to the reaction mixture facilitated nanocrystal precipitation; centrifugation helped to isolate the nanocrystals. 10 ml of ethanol was added to 1 ml of nanocrystal solution to precipitate the nanocrystals. The nanocrystal solution turned milky white, indicating the precipitation of the nanocrystals. This solution was centrifuged at 3500 rpm for 90 min in a Horizon Premier centrifuge, manufactured by the Drucker company. The nanocrystals settled at the bottom of the vial, and then, the supernatant was poured off to isolate the nanocrystals. The nanocrystal cleaned once with this sequence were termed as 1× -cleaned nanocrystals. The isolated nanocrystals were dispersed back in hexane and the precipitation-centrifugation sequence was repeated. The nanocrystals purified more than once were defined according to the number of cleaning steps employed. 8×-cleaned nanocrystals were employed for all the characterizations.

2.2.4 Characterization techniques

A Link ISIS Series 300 microanalysis system (Oxford Instruments) connected to a Hitachi S-4200 scanning electron microscope (SEM) was used to conduct elemental analysis of the RE-oleate complexes with X-ray energy dispersive spectroscopy (EDS). A thin-film of RE-oleate was deposited onto a silicon substrate by drop-casting technique, and the film was dried in air until the hexane evaporated. Molecular bondings of the RE-oleate complexes were characterized with Fourier transform infrared (FT-IR) spectroscopy using a Thermo-Nicolet 300 FT-IR spectrometer. A few drops of the precursor solution were placed onto a IR-transparent, potassium bromide (KBr) substrate and air-dried until the hexane evaporated. A TGA-1000 (Scientific Systems Inc.) thermogravimetric analysis (TGA) system was employed to determine the thermal decomposition temperatures of the RE-oleate complexes. A small section of the drop-casted film of RE-oleate was placed in a platinum weighing pan and was heated to 700 °C in an N_2 environment at a heating rate of 5 °C min^{-1}. A Scintag X1 powder diffractometer with Cu $K_{\alpha 1}$ radiation ($\lambda = 1.5406$ $\mathring{A}$) was used to conduct X-ray diffraction (XRD) experiments using a scan rate of 0.15 degree min^{-1} on the nanocrystals. A thin-film of the nanocrystals was prepared on a zero-background silicon plate (511 orientation) by drop-casting technique for XRD measurements. The nanocrystal size and size distribution were investigated using a Philips CM 20 transmission electron microscope (TEM) operating at 200 kV. The TEM samples were prepared by adding a drop of cleaned nanocrystals, dispersed in hexane, onto a copper grid covered with ultra-thin type-A carbon film (Ted Pella). A FT-IR spectroscopic analysis of the nanocrystals was conducted to investigate coverage of ligands on nanocrystal's surface. Photoluminescence (PL) experiments were performed using a Fluorolog 3 FL3-111 spectrophotofluorometer, equipped with 450 W Xenon lamp and photomultiplier tube. A quartz cuvette with 1-cm path length was used to hold the nanocrystal suspension prepared in hexane for PL measurement.

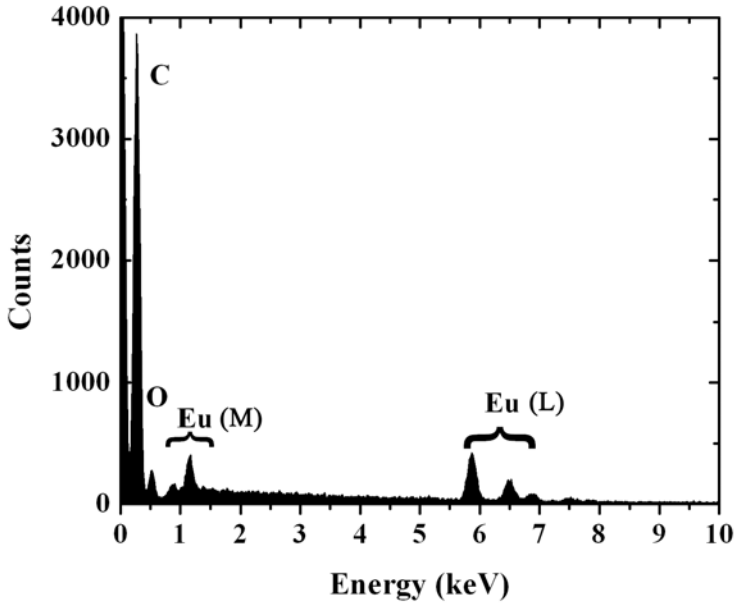

Figure 2.3: EDS spectrum of the europium precursor on a silicon substrate, which reveals the presence of europium, oxygen, and carbon that originates from the Eu-oleate complex. The absence of sodium and chlorine peaks confirmed sufficient cleaning of the Eu-oleate complex.

2.3 Results and discussion

2.3.1 Precursor characterization

To verify the completion of the reaction and the formation of the RE-oleate complex according to the equation 2.1, an elemental analysis of the precursor solution was performed. For the analysis, a few drops of the precursor solution were placed onto a silicon substrate. We chose a silicon substrate because its EDS peaks do not coincide with the europium, terbium, gadolinium, oxygen, and carbon peaks. Figure 2.3 shows a typical EDS graph of the Eu-oleate precursor. The characteristic X-ray emission peaks associated with the europium (L & M), carbon (K), and oxygen (K) were detected, which confirmed the presence of these elements. Hence, the precursor synthesis reaction was successful. In addition, the absence of sodium and chlorine peaks confirmed that the Eu-oleate precursor was washed sufficiently to remove sodium chloride (NaCl).

Fourier transform infrared spectroscopy is an excellent technique to characterize

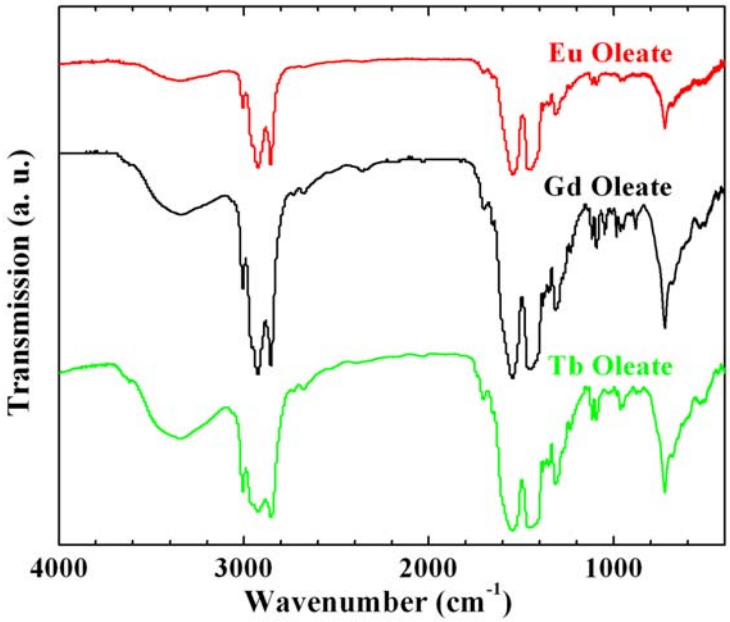

Figure 2.4: FT-IR spectra of Eu-, Gd-, and Tb-oleate complexes. The peaks at 1450 cm^{-1} and 1540 cm^{-1} are assigned to the symmetric $\nu_s(COO^-)$ stretch and asymmetric $\nu_{as}(COO^-)$ stretch vibrational modes, respectively. The FT-IR spectra are shifted vertically for clarity.

molecular bondings of a complex. The FT-IR analyses were performed on the precursor solutions to verify the formation of RE-oleate complexes. The FT-IR spectra in figure 2.4 show the presence of characteristic peaks of metal-oleate,[43] which confirmed the formation of the RE-oleate complexes. The peaks at 1450 cm^{-1} and 1540 cm^{-1} were assigned to the symmetric $\nu_s(COO^-)$ and asymmetric $\nu_{as}(COO^-)$ vibrational stretch modes of RE-oleates, respectively.

To investigate the thermal decomposition properties of the RE-oleate complexes, thermogravimetric analyses were conducted. TGA monitors weight of the sample as a function of temperature. Figure 2.5 shows the TGA curves of the RE-oleate complexes. A large drop in the weight of a complex indicated decomposition of the precursor. Complete decomposition of the RE-oleate complexes occurred below 550 °C since the weight of the complexes did not change significantly above 550 °C. Since the decomposition rates (or slopes of the curves) were maximum in the 350 - 375 °C region, the nanocrystal synthesis

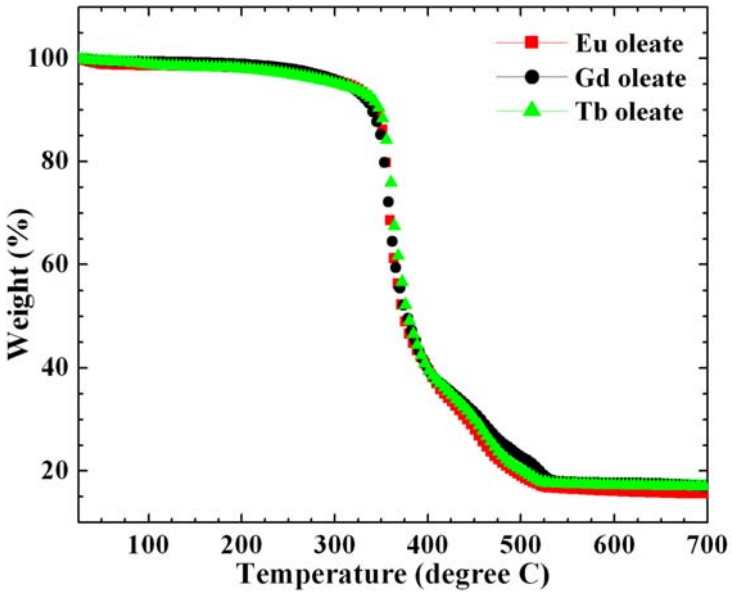

Figure 2.5: TGA curves of Eu-, Gd-, and Tb-oleate complexes. The thermal decomposition rate was maximum in 350-375 °C region, indicated by a sharp drop in weight.

temperature should be selected from this region.

2.3.2 Nanocrystal characterization

The decomposition of RE-oleate complexes in the presence of oleic acid and tri-*n*-octylamine yielded the rare-earth oxide (Eu_2O_3, Tb_2O_3, and Gd_2O_3:Eu^{3+}) nanocrystals. Investigations of the crystalline structure of these oxides were performed using X-ray diffraction. Figure 2.6 shows XRD patterns of the rare-earth oxide nanocrystals. Each of the peaks of the three patterns matched with the XRD patterns of the body-centered-cubic (bcc) crystallinities of the respective oxides [space group: $Ia\overline{3}$; JCPDS: 34-392 (Eu_2O_3), JCPDS: 23-1418 (Tb_2O_3), and JCPDS: 43-1014 (Gd_2O_3)]. The peaks were assigned to the specific lattice planes of the body-centered-cubic (bcc) crystallinities of the respective oxides. Since the lattice constants and crystal structures for the compounds were very similar [Eu_2O_3: 10.86 $\mathring{A}$, Tb_2O_3: 10.73 $\mathring{A}$, and Gd_2O_3: 10.81 $\mathring{A}$], the XRD patterns were similar as seen in figure 2.6. The presence of broadened peaks suggested that the nanocrystals were small in size. We attempted to identify the size of these nanocrystals with Scherrer analysis. A

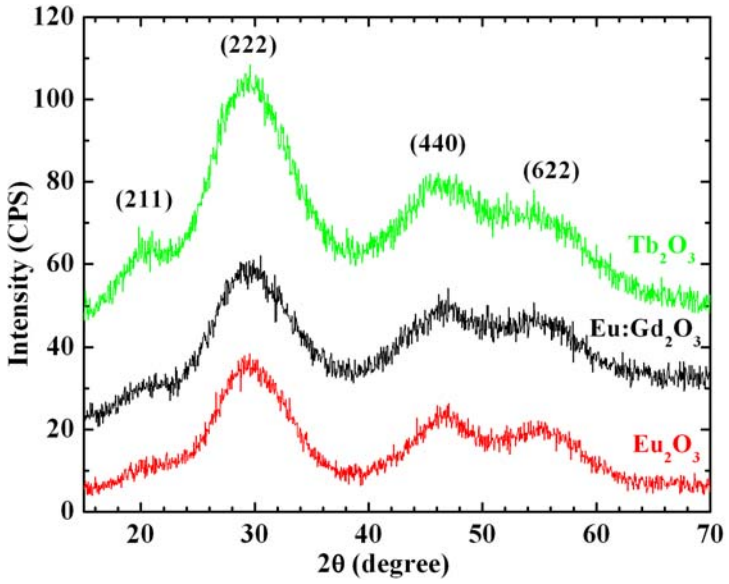

Figure 2.6: XRD patterns of Eu_2O_3, Gd_2O_3:Eu^{3+}, and Tb_2O_3 nanocrystals. All the peaks are assigned to the body-centered-cubic (bcc) form of their oxides [JCPDS: 34-392 (Eu_2O_3), JCPDS: 23-1418 (Tb_2O_3), and JCPDS: 43-1014 (Gd_2O_3)]. The observed peaks are reflections from the same lattice planes for the three oxides.

good peak fitting was not observed for the three curves because the peaks were very broad. The diameter of the nanocrystals determined from the analysis was $\sim$ 1.6 nm, which was significantly different from the diameter ($\sim$ 2.4) measured from the TEM images.

Figure 2.7 shows the TEM images of Eu_2O_3, Tb_2O_3, and Gd_2O_3:Eu^{3+} nanocrystals. The nanocrystals were 2.4 $\pm$ 0.3 nm in size. We observed the identical diameter and dispersivity for the three nanocrystal types, using the same synthesis parameters. Controlled nucleation and growth of oxide nuclei via appropriate precursor and synthesis temperature selection were key to the synthesis of monodisperse, small size nanocrystals. A metal-oleate complex is formed inevitably when oleic acid is involved in the synthesis with any metal precursor because oleic acid reacts quickly with metal ions at high temperatures.[42,44] Therefore, it was advantageous to employ RE-oleate complexes as RE-precursor for controlled nucleation. Further, the synthesis temperature ($\sim$ 350 °C) was slightly lower than the temperature ($\sim$ 370 °C) at which decomposition rate was a maximum. Thus, the slow nucleation and growth facilitated the formation of very small nanocrystals.

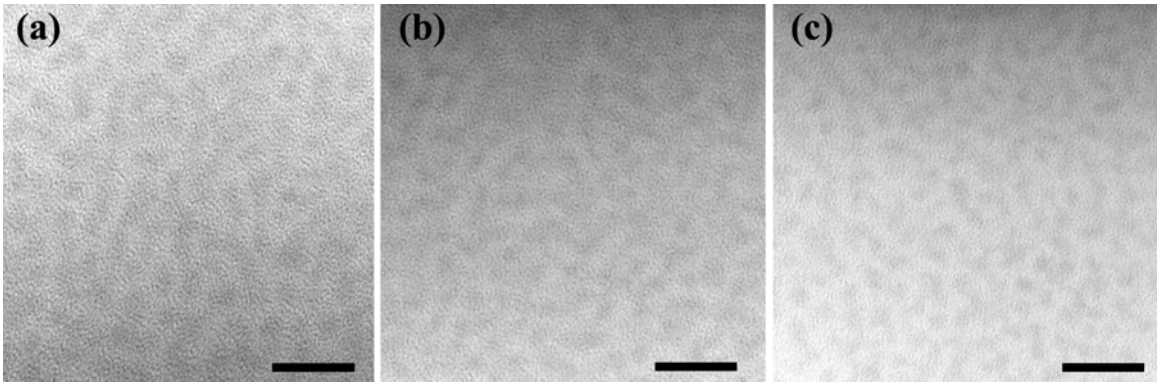

Figure 2.7: TEM images of (a) Eu_2O_3, (b) Gd_2O_3:Eu^{3+}, and (c) Tb_2O_3 nanocrystals. The average size of all three nanocrystals types is $\sim$ 2.4 nm. Scale bars for the images are 12 nm.[41]

Colloidal stability of the nanocrystals is dependent on the nanocrystal surface ligand coverage and the equilibrium adsorption/desorption of the ligands on said surface.[45,46] To assess the colloidal stability of our nanocrystals, we probed the surface binding through FT-IR spectroscopy. Figure 2.8 shows the FT-IR spectra of the nanocrystals. The spectra revealed the binding nature of capping ligand with the nanocrystal surface. Free carboxylic acid has a characteristic peak near 1700 cm^{-1}, which represents the C=O stretch mode of free carboxylic acid. The absence of this characteristic peak near 1700 cm^{-1} indicated the absence of free oleic acid. The peaks at 1440 cm^{-1} and 1550 cm^{-1} were assigned to the symmetric $\nu_s(COO^-)$ stretch and asymmetric $\nu_{as}(COO^-)$ vibrational stretch modes, respectively. The difference of 110 cm^{-1} between the symmetric and asymmetric stretches identified the binding as chelating bidentate.[47,48]

Photoluminescence characteristics of the RE-oleate complexes and the nanocrystals were investigated with photoluminescence spectroscopy. PL spectra were collected in the spectral range of 575 - 725 nm wavelength for Eu^{3+} -based materials and 475 - 650 nm wavelength for Tb^{3+} -based materials upon UV excitation at 254 nm. The nanocrystals and the RE-oleate complexes were suspended in hexane for the PL measurements. Prior to measuring the PL spectrum of the sample, a background spectrum of pure hexane was collected in the same cuvette using the same experimental parameters. This spectrum

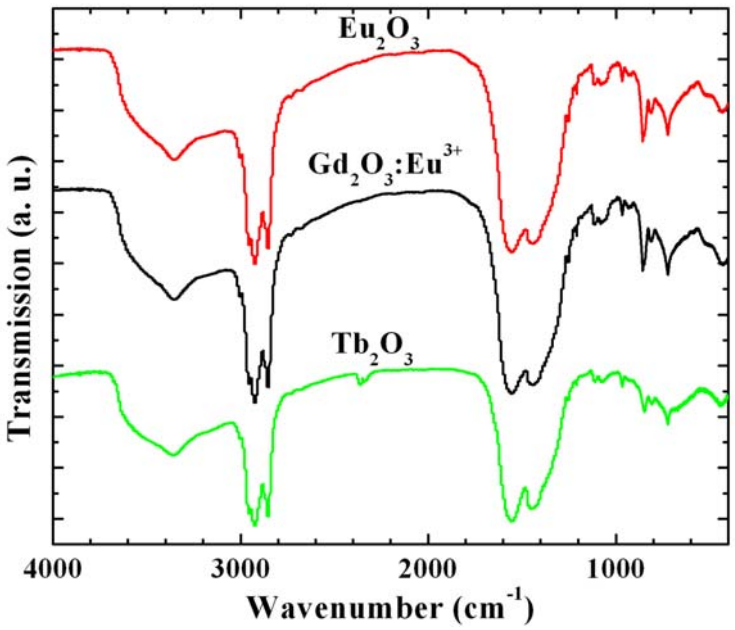

Figure 2.8: FT-IR spectra of Eu_2O_3, Gd_2O_3:Eu^{3+}, and Tb_2O_3 nanocrystals. The peaks at 1440 cm^{-1} and 1550 cm^{-1} are assigned to the symmetric $\nu_s(COO^-)$ stretch and asymmetric $\nu_{as}(COO^-)$ stretch vibrational modes, respectively. The FT-IR spectra are shifted vertically for clarity.

was subtracted from the spectrum of the nanocrystal/RE-oleate suspension by the data collection software to obtain the photoluminescence characteristics of the nanocrystals and the RE-oleate complexes.

Figure 2.9(a) exhibits PL spectra of the Eu-oleate and Eu_2O_3 nanocrystals. The spectra were collected upon excitation with a xenon lamp (254 nm). The PL spectra represent the luminescence peaks arising from a collection of the $^5D_0 \rightarrow {}^7F_J$ (J = 0 - 4) emission transitions within Eu^{3+} ions (Figure 1.7). Detailed explanation of these emission transitions is provided in section 1.3.2. The electronic transitions $^5D_0 \rightarrow {}^7F_{2,4}$ are particularly sensitive to the local environment of the Eu^{3+} ions. Eu^{3+} ions arranged within a bcc crystal structure of Eu_2O_3 have luminescence characteristics that differ from those of the Eu^{3+} oleate complex. For the sensitive $^5D_0 \rightarrow {}^7F_2$ transition, the Eu_2O_3 nanocrystals exhibited two strong, narrow peaks (612 nm and 620 nm) and one weaker peak (625 nm) compared to a single strong peak (616 nm) for the Eu-oleate complex as clearly observed in figure

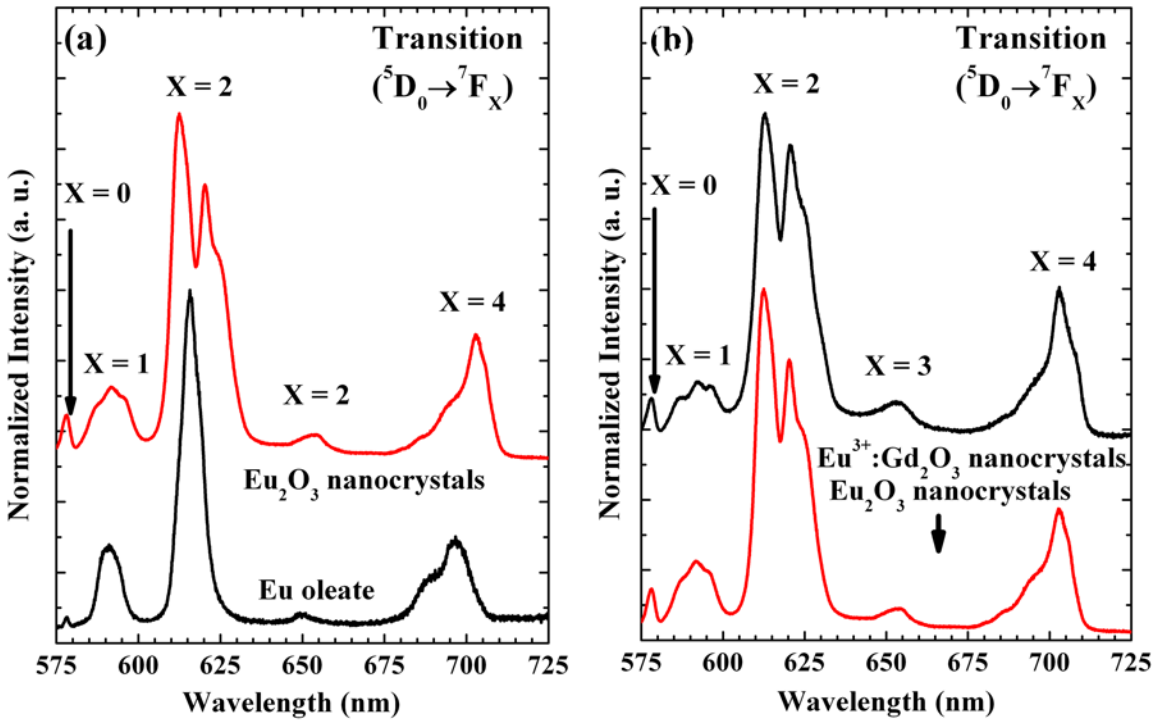

Figure 2.9: (a) PL spectra of Eu oleate and Eu_2O_3 nanocrystals. A completely different optical signature for nanocrystals, in comparison to Eu oleate, confirms the formation of oxide nanocrystals. (b) PL spectra of Eu_2O_3, and Gd_2O_3:Eu^{3+} nanocrystals. All the above mentioned spectra are normalized and shifted vertically for clarity.

2.9(a). Eu^{3+} ions in the Eu_2O_3 nanocrystals are in a crystallographic lattice. The energy levels of the Eu^{3+} ions split into multiple energy manifolds because of the crystal field. The transition of electrons into these multiple energy manifolds corresponds multiple luminescent peaks in the PL spectrum. The splitting of energy levels of Eu^{3+} ions in Eu-oleate complex does not occur because the ions are not in a crystallographic environment. Similarly for the other transitions [^7F_J: J = 0, 1, 3, 4], different luminescence characteristics were observed for the Eu_2O_3 nanocrystals compared to the Eu oleate complex. When we compared the spectrum of our Eu_2O_3 nanocrystals with spectra reported in the literature for nanocrystalline and bulk cubic Eu_2O_3, we observed a new luminescence peak at 620 nm for our nanocrystals.[12,14,39] The origin of this peak is discussed in the section 2.3.3.

Figure 2.9(b) shows the PL spectrum of the Gd_2O_3:Eu^{3+} nanocrystals juxtaposed with that of the Eu_2O_3 nanocrystals. Similarity between the two spectra is clearly observed. The spectral positions of the luminescence peaks for these two nanocrystal types were largely unaffected. Similarity between the respective unit cells [bcc crystal structure, space group: $Ia\overline{3}$, lattice constants: Eu_2O_3: 10.86 $\AA$ & Gd_2O_3: 10.81 $\AA$] provided similar atomic environment to the Eu^{3+} ions. Thus, the electron transition energy levels within Eu^{3+} ions of the Gd_2O_3:Eu^{3+} and Eu_2O_3 nanocrystals and, therefore, the corresponding luminescence peaks were identical as expected.

The photoluminescence studies of our very small Tb_2O_3 nanocrystals were also performed. The PL spectra of the Tb oleate and Tb_2O_3 nanocrystals are shown in figure 2.10. The PL spectra represent the luminescence peaks arising from a collection of the $^5D_4 \rightarrow {}^7F_J$ (J = 6 - 3) emission transitions within Tb^{3+} ions (Figure 1.8). Similar to Eu_2O_3, Tb^{3+} ions arranged within a bcc crystal structure of Tb_2O_3 have luminescence characteristics that differ from those of the Tb^{3+} oleate complex. For the $^5D_4 \rightarrow {}^7F_5$ transition, the Tb_2O_3 nanocrystals exhibited one strong peak (542 nm) and one weaker peak (548 nm) compared to a single strong peak (542 nm) for the Tb-oleate complex (Figure 2.10). The crystal field dependent energy level splitting was responsible for this effect in

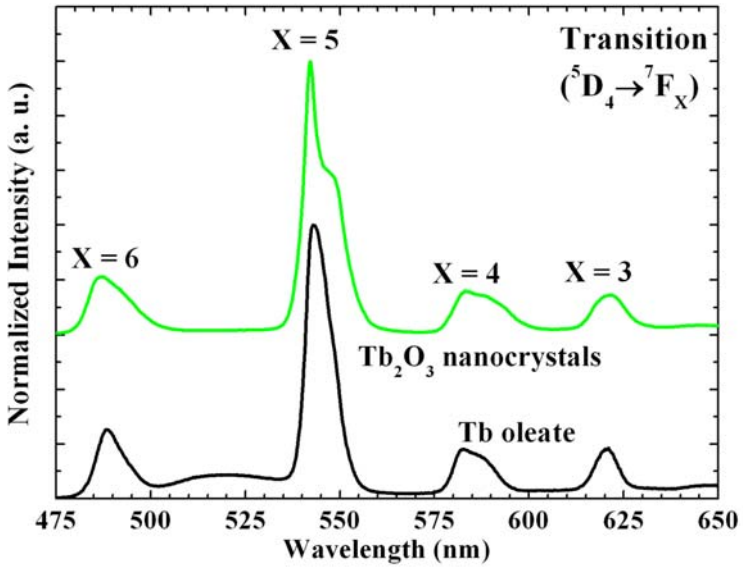

Figure 2.10: PL spectra of Tb oleate and Tb_2O_3 nanocrystals. A peak at 548 nm observed for nanocrystals, in comparison to Tb oleate, confirms the oxide nanocrystals formation. The spectra above mentioned are normalized and shifted vertically for clarity.

Tb_2O_3 nanocrystals.

2.3.3 New luminescence peak: a size effect

The emergence of a new luminescence peak at 620 nm from our Gd_2O_3:Eu^{3+} and Eu_2O_3 nanocrystals was of substantial interest to us because this peak had not been reported for other Eu^{3+}-based rare-earth oxide nanostructures. To investigate origin of the new luminescence peak, the nanocrystals of different sizes were synthesized to probe a potential size effect, if any.[49] The nanocrystals of different sizes were synthesized by varying the amount of oleic acid added to the reaction mixture during synthesis. The effect of oleic acid on nanocrystal size relied on nucleation and growth mechanism. The addition of oleic acid helped to redissolve a portion of oxide nuclei and, thus, conserved precursor (RE-oleate) for the nanocrystal growth. Therefore, an increased amount of oleic acid produced larger nanocrystals within a small size regime (Figure 2.11). However, an increase in the amount of oleic acid led to lower reaction yields. A low reaction yield (<30%) was observed when we employed 1 mM of oleic acid. Table 2.1 lists the amount of oleic acid used in the reaction

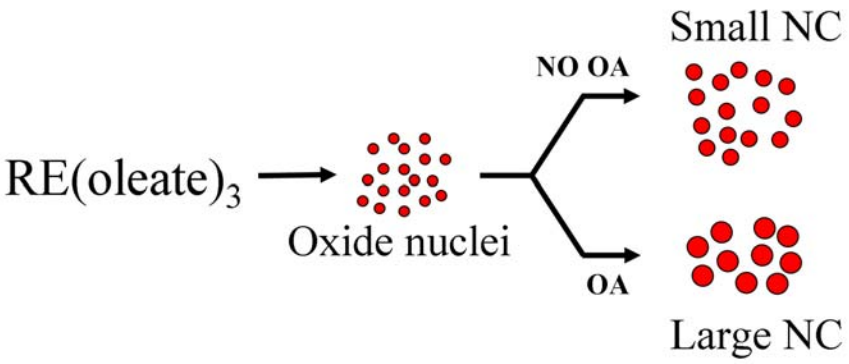

Figure 2.11: Schematic of the nanocrystal size control process via addition of oleic acid. Addition of oleic acid redissolves oxide nuclei during synthesis and facilitates growth of large nanocrystals.

Table 2.1: Comparison of synthesis reaction mixture and nanocrystal size.

RE precursor (mM)	Oleic acid (mM)	tri-*n*-octylamine (mM)	Nanocrystal size (nm)
0.50	0.00	16.0	~ 1.8
0.50	0.25	16.0	~ 2.4
0.50	1.00	16.0	~ 3.0

mixture and corresponding nanocrystal size produced.

PL measurements were performed on the three different nanocrystal sizes (1.8 nm, 2.4 nm, and 3.0 nm) of the two nanocrystal types (Eu_2O_3 & Gd_2O_3:Eu^{3+}). Figure 2.12 a and b show the size-dependent photoluminescence spectra for the Eu_2O_3 and Gd_2O_3:Eu^{3+} nanocrystals. Each spectrum was normalized to the peak at 612 nm and shifted vertically for clarity. We focused our attention on the peaks at 612 nm, 620 nm, and 625nm, which were attributed to the most sensitive transition ($^5D_0 \rightarrow {}^7F_2$) of Eu_2O_3 and Gd_2O_3:Eu^{3+} nanocrystals. The observed peak broadening for our nanocrystals is consistent with that observed for the other nanocrystalline Eu_2O_3 and Gd_2O_3:Eu^{3+}.[3,10,12,15,36] When the spectra of our nanocrystals were compared with the spectra reported for nanocrystalline and bulk Eu_2O_3 materials, we identified the conventional peak for cubic Eu_2O_3 at 612 nm. The peak at 625nm has been reported for cubic Eu_2O_3 nanodisks, which the authors attributed to the occupation of Eu^{3+} ions in a unique surface site because of ultrathin thickness (1.6 nm)

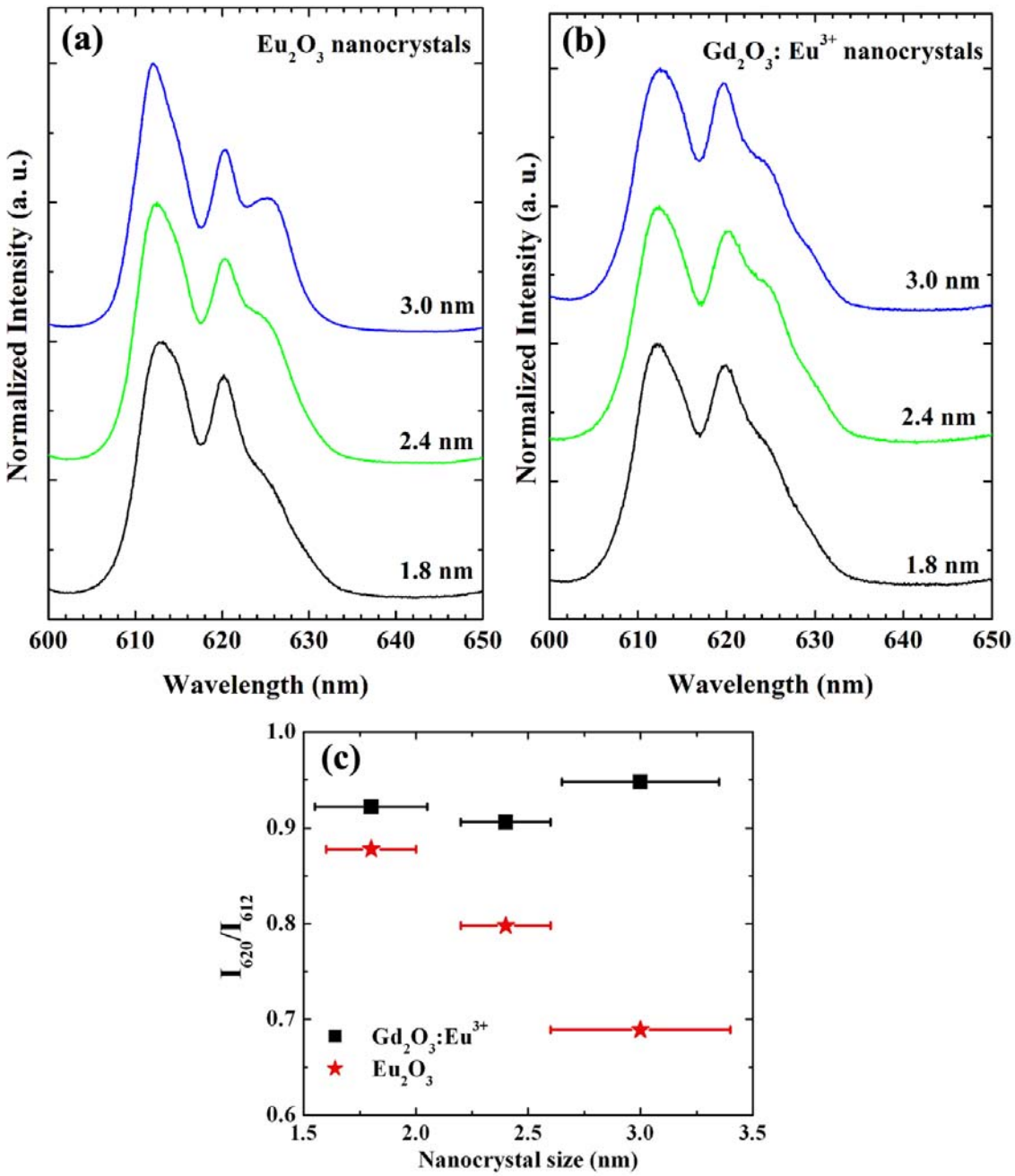

Figure 2.12: PL spectra of Eu_2O_3 (a) and Gd_2O_3:Eu^{3+} (b) nanocrystals synthesized with varying amount of oleic acid. The spectra are normalized to the peak at 612 nm and shifted vertically for clarity. (c) The intensity variation of the new peak (620 nm) with respect to the 612 nm peak determined from the above PL spectra.

of nanodisks.[14] The presence of the new spectral feature in PL spectra of our nanocrystals suggests a similar size-dependent effect on the $^7F_2$ states in our nanocrystals. A comparable number of surface lattice sites in comparison with the core lattice sites are present in very small-size nanocrystals due to an increased surface-to-volume ratio (SVR). Eu^{3+} ions occupying the nanocrystal surface sites experience different crystal field compared to the ions occupying the nanocrystal core sites because of the different atomic arrangements surrounding them. Since luminescence of the Eu^{3+} ions is sensitive to the crystal field that they experience, the new luminescence peak should be from the Eu^{3+} ions occupying the nanocrystal surface. We observed a variation in the intensity of the peak (620 nm) juxtaposed with the stronger primary peak (612 nm) for different nanocrystal sizes and, hence, we monitored the intensity for both nanocrystal types as a function of the nanocrystal size. Figure 2.12(c) shows a graph of the ratio of intensities of the two peaks ($R = I_{620\,nm}/I_{612\,nm}$) as a function of nanocrystal size. The ratio R decreased from 0.88 to 0.70 as the size of Eu_2O_3 nanocrystals increased. We expected the intensity variation of the peak as a function of nanocrystal size in Gd_2O_3:Eu^{3+} nanocrystals too. In contrast, we noticed a different trend compared to that for the Eu_2O_3 nanocrystals. Since the number of surface lattice sites in comparison with the core lattice sites changes as a function of nanocrystal size, the observed intensity modification of the peak with nanocrystal size should be from the Eu^{3+} ions occupying a new surface site in our ultra-small nanocrystals.

2.3.4 Concentration quenching in nanocrystals

To gain an insight into the effect of concentration quenching in our nanocrystals, we investigated relationship between the integrated PL intensity and the absorbance of the Eu_2O_3 and Gd_2O_3:Eu^{3+} nanocrystals. For this study, we selected the two nanocrystal sizes, $\sim$ 1.8 nm and $\sim$ 2.4 nm as shown in figure 2.13(a-d). The nanocrystal suspensions of different concentrations were prepared in hexane. Absorption measurements were performed on the nanocrystal suspensions using a Varian Cary 5000 spectrophotometer. Absorbance

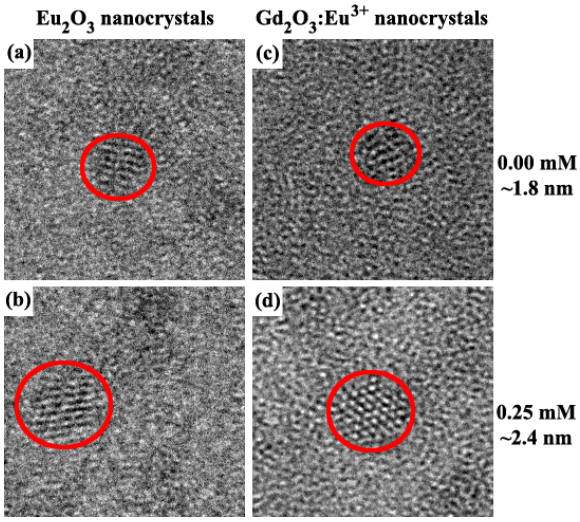

Figure 2.13: TEM images of the nanocrystals of Eu_2O_3 (a and b) and Gd_2O_3:Eu^{3+} (c and d) synthesized using 0.00 and 0.25 mM oleic acid. Each image is 10 nm × 10 nm.

of the nanocrystal suspension at 254 nm was determined from the corresponding spectrum. Low absorbance values (or low nanocrystal concentration) were considered for the analysis to avoid reabsorption/scattering of light in nanocrystal suspension. PL spectra of these nanocrystal suspensions were recorded. The PL spectrum was integrated over 525-725 nm wavelength range to determine integrated PL intensity. The integrated PL intensity of nanocrystals is plotted as a function of nanocrystal absorbance, which is shown in figure 2.14(a-b). The relationship between integrated PL intensity of nanocrystals and absorbance was linear. For a given absorbance, integrated PL intensity of Gd_2O_3:Eu^{3+} nanocrystals was higher than that of the Eu_2O_3 nanocrystals for the two nanocrystal sizes as seen from figure 2.14. Luminescence efficiency is directly proportional to ratio of the integrated PL intensity to the absorbance. Thus, the Gd_2O_3:Eu^{3+} nanocrystals had better luminescence efficiency than the Eu_2O_3 nanocrystals, which confirmed the presence of concentration quenching effects in our Eu_2O_3 nanocrystals.

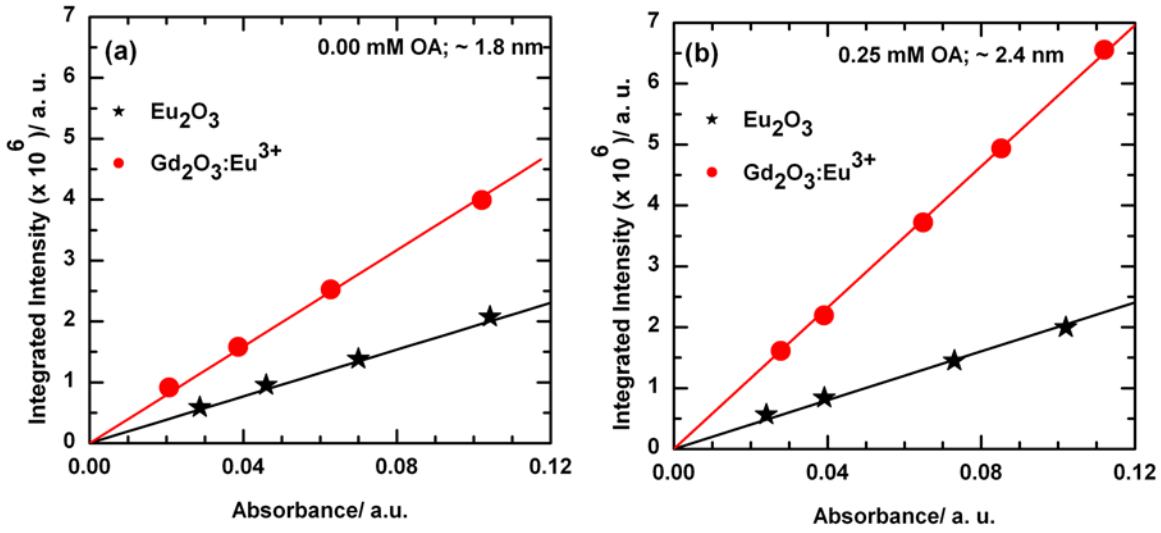

Figure 2.14: (a) Integrated PL intensity of (a) 1.8 nm (no OA) and (b) 2.4nm (0.25mM OA) Eu_2O_3 and Gd_2O_3:Eu^{3+} nanocrystals. The X and Y error bars for the data are within the data point. The solid lines represent liner fit to each dataset.

2.4 Summary

A new synthesis technique to produce colloidally stable, monodisperse rare-earth oxide nanocrystals was developed successfully. The versatile technique produced sub-3 nm Eu_2O_3, Tb_2O_3, and Gd_2O_3:Eu^{3+} nanocrystals via the thermal decomposition of their respective oleate complexes in tri-*n*-octylamine. The addition of oleic acid to the synthesis mixture provided control over the nanocrystal size within a small size regime (sub-3 nm). The appropriate choice of precursor and synthesis temperature enabled controlled nucleation and growth of the sub-3 nm nanocrystals. A new luminescence peak at 620 nm was observed in Eu_2O_3 and Gd_2O_3:Eu^{3+} nanocrystals. Intensity modifications of this peak as a function of nanocrystal size suggested size-dependent effect. Emergence of the new peak should be due to the occupation of Eu^{3+} ions in a new surface site of sub-3 nm nanocrystals, which needs to be explored with further experiments. Concentration quenching effects were observed in our Eu_2O_3 nanocrystals when compared with Gd_2O_3:Eu^{3+} nanocrystals.

CHAPTER III

ELECTROPHORETIC DEPOSITION: A PARTICLE ASSEMBLY TECHNIQUE

3.1 Introduction

Electrophoretic deposition (EPD) technique is not only of scientific interest but also of technological importance in the area of particle assembly. In EPD, charged particles are assembled under the influence of an electric field. EPD offers a number of advantages over the other particle assembly techniques, which include simple setup, substantial thickness control, high deposition rate, ability to deposit particles site-selectively, capability to deposit on the different shapes of substrate, and cost-effectiveness.[50] In addition, particles of different types (metallic, semiconducting, dielectric, and polymeric) can be deposited by EPD as long as they acquire charge when suspended in a liquid medium. Such particles, when forming well-stabilized suspensions, can produce homogeneous assemblies of particles, i.e films/coatings.

In the field of ceramic processing, ceramic particles are assembled to produce coatings with different shaping techniques, which include dip casting, slip casting, and EPD. Of available shaping techniques, EPD is employed widely to process advanced ceramics and their coatings for past three decades. Various ceramic particles (oxides, boride, carbides, nitrides) have been deposited successfully from their suspensions in polar solvents to form ceramic coatings.[51,52] Also, functionally graded ceramics and layered ceramics have been produced by EPD.[53–55] For biomedical applications, coatings of hydroxyapatite have been produced by EPD.[56,57] Over the years, several studies have been performed to understand the fundamental mechanisms of the development of surface charge on ceramics that are suspended in polar solvents. Also, parameters that influence EPD of ceramics that are have

been investigated.[51] Thus, EPD of ceramics in polar solvents is well understood.

In nanotechnology, the controlled assembly of nanomaterials into microscopic and macroscopic structures is one of the most important and continuously growing research directions. Efficient bottom-up assembly approaches are essential to the development of next-generation optical, magnetic, electronic devices that utilize the unique properties of metallic, semiconducting, or insulating nanomaterials. Currently employed nanomaterials assembly techniques include drop-casting, spin-casting,[58] self-assembly,[59–61] Langmuir-Blodgett,[62,63] and EPD.[17,64,65] Of these techniques, EPD is the promising technique to assemble nanomaterials because of its several advantages. EPD has been employed successfully to deposit films of metallic (Au, Pt),[66,67] semiconducting (CdSe, ZnO),[17,68] insulating (TiO_2, SiO_2, Eu_2O_3)[69–73] and magnetic (Fe_3O_4, Fe_2O_3,)[65,74] nanocrystals from their suspension in polar or non-polar solvents. Other types of nanomaterials, such as polymer nanoparticles[75,76] and carbon nanotubes (CNTs),[65,77–82] have been assembled via EPD. Homogeneous and smooth films of the nanocrystals have been reported for the nanocrystals functionalized with surface capping ligands such as CdSe, Fe_2O_3, Fe_3O_4, and Eu_2O_3, which were dispersed in non-polar solvents.[17,65,71,83] EPD of particles, suspended in non-polar solvents, is relatively new, and the underlying mechanisms are not well understood.

This chapter provides a brief overview of the EPD technique. Since the EPD of particles in polar solvents has been widely employed and throughly studied, fundamentals of this technique, such as the development of surface charge and the interaction between particles, are described in a concise manner. Important aspects and findings of this recently introduced technique, performed in non-polar solvents, are discussed. Experimental details of EPDs that are performed within the scope of this dissertation are specified.

3.2 Electrophoretic deposition (EPD)

Electrophoretic deposition involves locomotion of charged particles, suspended in a liquid medium, under the influence of an applied electric field and their deposition on an

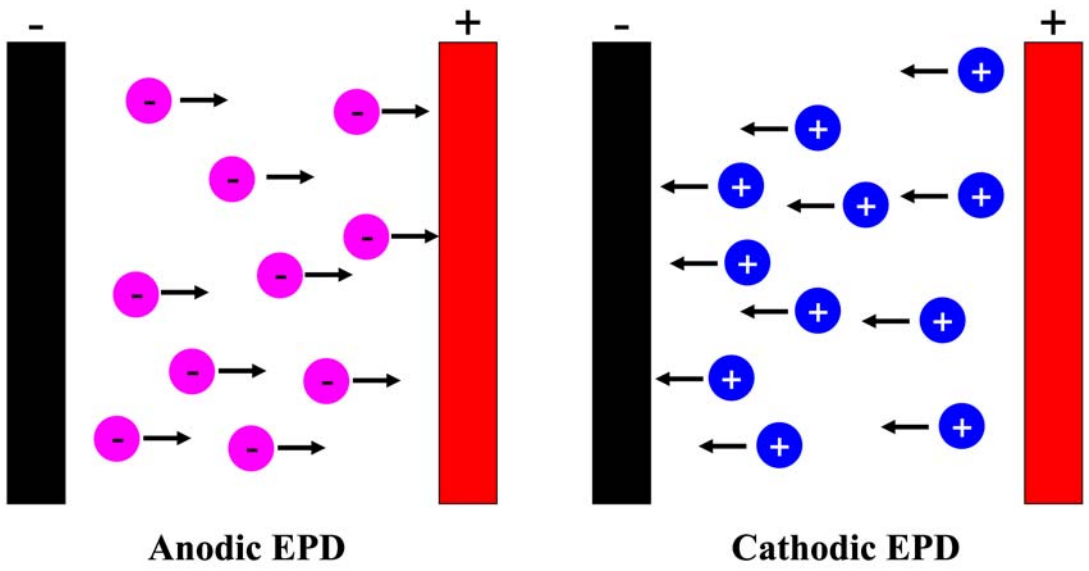

Figure 3.1: Schematic of (a) anodic EPD and (b) cathodic EPD. In anodic EPD, film is deposited on the anode, while the particles are deposited on cathode in the cathodic EPD.

electrically conductive substrate of opposite polarity. The particles can be deposited even on an insulating layer, provided the layer is sufficiently thin so that an applied voltage do not entirely drop across the insulating layer. Traditionally, EPD is classified into two types based on the electrode on which particles deposit: anodic EPD and cathodic EPD. Figure 3.1 shows schematic of the two types of EPD. In anodic EPD, negatively charged particles deposit on the anode. The deposition of positively charged particles occurs on the cathode in cathodic EPD. The surface charge on particles can be modified to achieve one of the two EPD conditions. The particles that posses or can acquire surface charge, when suspended in a liquid medium, and form stable suspension, can be deposited with EPD technique.

In EPD technique, multiple parameters influence the deposition process and the deposit. These parameters can be classified into two categories: a) EPD suspension parameters, and b) EPD process parameters. Hamaker and Avgustnik studied the influence of these parameters on the amount of particles deposited (deposit yield, w) during EPD of ceramic particles.[84,85] Hamaker developed the equation (Equation 3.1) that relates the deposit yield, w to different influencing parameters such as the electrophoretic mobility

(μ), the electric field ($\left|\vec{E}\right|$), the electrode area (A), the particle mass concentration in the suspension (C), and the deposition time (t).

$$w = \mu \cdot \left|\vec{E}\right| \cdot A \cdot C \cdot t \tag{3.1}$$

Avgustnik developed a relation between deposit yield and the influencing parameters (Equation 3.2), but for the specific configuration of electrodes in EPD setup: a cylindrical, coaxial, electrode configuration.

$$w = \frac{l \cdot \left|\vec{E}\right| \cdot \epsilon \cdot \zeta \cdot C \cdot t}{3\, ln(a/b) \cdot \eta} \tag{3.2}$$

In this equation, electrophoretic mobility is represented in terms of the permittivity (ϵ), the zeta-potential (ζ), the viscosity (η) of the suspension. The length (l) and the radius (a) of the deposition electrode, and the radius (b) of the counter electrode (b > a) are the design parameters of EPD setup. Of the aforementioned parameters, EPD suspension parameters are the electrophoretic mobility, zeta-potential, viscosity, and permittivity, while electrode design (l, a, b, A), electric field, deposition time, and particles concentration are the EPD process parameters. The effect of these parameters on the deposition process (in polar solvents) has been investigated extensively.[51] EPD suspension parameters are optimized to form well-dispersed suspension of particles, while EPD process parameters are tuned to produce homogeneous deposits of required thickness. A solvent plays an important role in forming well-dispersed particle suspensions and thus, solvent is a suspension parameter. EPD technique can be classified based on the type of solvent used: EPD in polar solvents and EPD in non-polar solvents.

3.2.1 EPD in polar solvents

Polar solvents are commonly employed as the particle suspension media for EPD technique. Typically, the particles suspended in such solvents acquire the surface charge easily, which is important for EPD. Common polar solvents used for EPD are water (H_2O), ethanol (C_2H_6O), acetone (C_3H_6O), propanol (C_3H_8O), acetylacetone ($C_5H_8O_2$), and acetone-

ethanol/ethanol-water mixtures.[51] EPDs, performed in polar solvents, are further classified in the two types: aqueous EPD and non-aqueous EPD.[86,87] In aqueous EPD, water is used as the particle suspension medium. Since water is non-toxic, non-flammable, and abundant, this technique is environmentally safe and cost-effective. However, this technique is susceptible to electrochemical reactions at the electrodes, which affects the quality of the EPD film.[88] Even at low applied voltages, aqueous suspensions of particles conduct high currents due to high electrolytic currents, passing through water. If the electric fields are high enough, electrolysis of water occurs, and gas bubbles (H_2 & O_2) are formed at the electrodes, which affects the homogeneity of the deposited films. Hence, the range of operating voltages for aqueous EPD is very limited. In non-aqueous EPD, organic solvents are employed as the particle suspension media. Generally, the possibility of electrolysis is significantly minimized or completely absent in these solvents because of their low dielectric constants and the minimal presence of water combined. Also, these solvents have higher dielectric breakdown potentials than that of water, which facilitate the larger operating voltage range. In addition, low conductivity and good chemical stability are typical characteristics of these solvents. However, toxicity, flammability, and high costs are among the drawbacks of these liquids. Both aqueous and non-aqueous EPDs are employed commercially.[51]

Irrespective of the type of solvent used (aqueous or non-aqueous) for EPD, the ability to acquire charge on the surface of particles, suspended in the solvent, is essential for deposition. When particles are suspended in a polar solvent, usually a charge develops at the solid-liquid interface.[89] Mechanisms for the development of charge on particles in water are well understood, which include adsorption of polar molecules at the interface, selective adsorption of free ions from liquid onto the particle surface, and dissociation of solid ions from the surface of particles into the solvent.[51,52] Protons have been identified as the charge determining ions in aqueous suspensions of ceramic particles, specifically oxides.[90] Thus, the surface charge of the particles can be modified by controlling pH of an aqueous EPD suspension.

Unlike aqueous EPD suspensions, knowledge of the mechanisms that are responsible for the development of surface charge in non-aqueous EPD suspensions is limited. The concept of hydrogen concentration (pH) as a measure of acidity or alkalinity looses its validity in non-aqueous solvents because of the absence of hydrogen ions. Wang et al observed that alumina particles acquire the surface charge in ethanol by addition of acetic acid or tetra-methyl-ammonium-hydroxide.[91] The surface charge characteristics of alumina particles suspended in ethanol were similar to that of the oxide particles suspended in water.[92] Vandeperre et al performed potentiometric titration experiments to determine the charging of various ceramic particles (oxides, borides, carbides, nitrides), and the charging characteristics were compared to the sign of the electrophoretic mobility measured in acidic and alkaline non-aqueous solvents.[93] These experiments confirmed that the charging of ceramic particles in a non-aqueous medium is analogous to charging in water. The small amount of residual water in non-aqueous solvents has been suggested to play a role in charging of yttria-stabilized zirconia (YSZ) particles.[94] The addition of iodine, a charging agent, in acetone or acetylacetone facilitates the formation of protons, which are adsorbed onto the surface of suspended particles.[95,96] Thus, the ceramic research community has acquired a working knowledge of the control of the surface charge of particles suspended in non-aqueous solvents.

Particles with surface charge, suspended in liquid media, experience interparticle forces, such as the van der Waals attractive force, electrostatic repulsive force, and steric repulsive force. Stability of the particle suspension is governed by the net interparticle forces. Well-stabilized, non-agglomerated particle suspensions are necessary for EPD. The repulsive forces between the particles should exceed the van der Waals attractive forces to achieve well-stabilized particle suspension. The classical DLVO theory, developed by Derjaguin and Landau[97] and Verwey and Overbeek,[98] describes the relationship between the interparticle forces and energies of interaction to stabilize the suspensions. This theory considered only the electrostatic and van der Waals forces. The DLVO theory was primarily

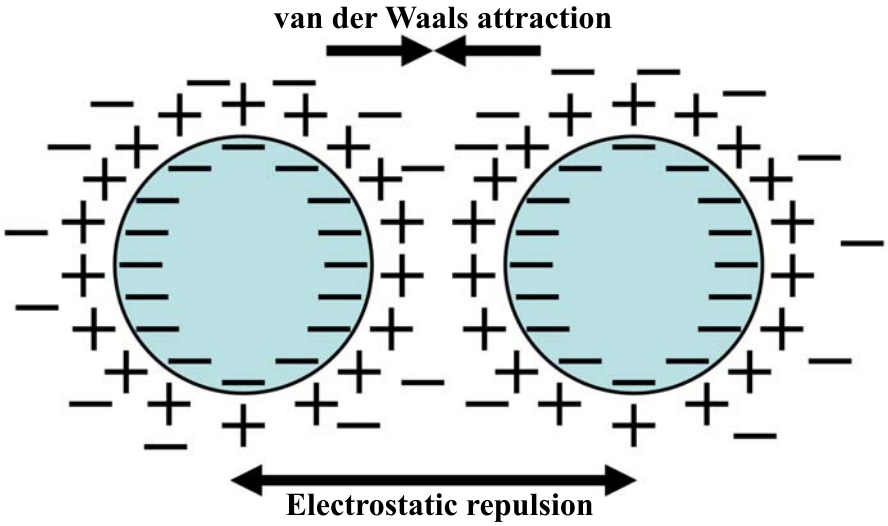

Figure 3.2: Schematic of electrostatically stabilized particles in suspension. Electrostatic repulsive forces between the particles supersede van der Waals attraction forces to obtain well-stabilized suspension.

developed for the electrostatically stabilized suspensions, i.e particle suspensions in polar media. Figure 3.2 shows schematic of the electrostatically stabilized particles.

In a well-stabilized particle suspension, the charged particles move with a velocity under the influence of an electric field, a phenomenon which was first studied by Smoluchowski[99] The mobility (μ) of the particles under electrophoretic forces, known as electrophoretic mobility, is related to the zeta potential of the particle (ζ), the solvent viscosity (η), relative permittivity of the solvent (ϵ_r), and the permittivity of vacuum (ϵ_0) through the Hückel equation (Equation 3.3).

$$\mu = \frac{2 \cdot \epsilon_0 \cdot \epsilon_r \cdot \zeta}{3 \cdot \eta} \tag{3.3}$$

Typically, electrophoretic mobility of the particles is measured by dynamic light scattering (DLS) experiments. The particles can have positive or negative electrophoretic mobility based on their zeta potential. Negatively charged particles have negative electrophoretic mobility, while positively charged particles have positive electrophoretic mobility. Thus, the sign of electrophoretic mobility indicates where the particles deposit (anode/cathode).

Typically, all the particles suspended in polar solvents have one type of electrophoretic mobility (positive or negative). Hence, the particles deposit only on one electrode (e.g. cathode EPD and anodic EPD).

Recently, carbon nanotubes (CNTs) have been deposited successfully with aqueous and non-aqueous EPD technique.[77] Typically, CNTs require a post-synthesis treatment to remove impurities and to isolate individual tubes from their aggregates.[100–102] The CNTs are functionalized with acidic surface groups, which are developed during the post synthesis purification treatment.[101,102] These acidic group electrostatically stabilize the CNTs in water or other non-aqueous polar solvents, by developing a negative surface charge. The resulting repulsion between the CNTs suspended in the solvent forms a well-stabilized CNT suspension. Similar to the EPD of ceramics, the CNTs have been deposited with different polar solvents.[77] EPD of the CNTs explored in this dissertation involved suspension of the CNTs in water.[Section 6.2.2]

3.2.2 EPD in non-polar solvents

Recently, the non-polar solvents, such as hexane and hexane-octane mixture have been employed to suspend the particles for EPD. This technique is primarily employed for the deposition of nanocrystals, which are surface functionalized with ligands such as oleic acid and TOPO. A large number of nanocrystal synthesis techniques employ ligands to control nanocrystal growth during synthesis and to prevent their agglomeration. Generally, the hydrophobic ends of these ligands extend outward from the surface of nanocrystals when the nanocrystals are surrounded by a hydrophobic medium (non-polar solvent). In contrast, these ligands collapse and the nanocrystals flocculate when the hydrophobic ends of these ligands interact with polar solvent molecules (hydrophilic). Therefore, such nanocrystals form stable suspensions in the non-polar solvents such as hexane, hexane-octane mixture. In such systems, steric repulsive forces, developed between the nanocrystals by the ligands, overcome the van der Waals attraction forces as depicted in figure 3.3.[103] Since sterically

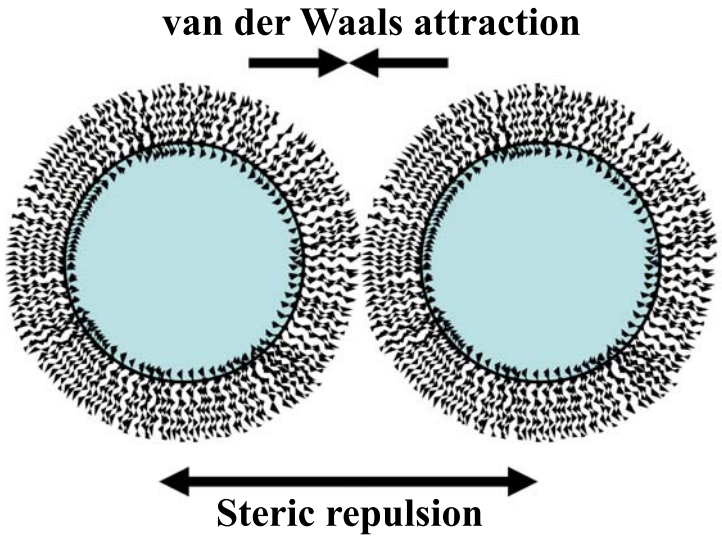

Figure 3.3: Schematic of sterically stabilized particles in suspension. Steric repulsive forces between the particles overcome van der Waals attraction forces to obtain well-stabilized suspension.

stabilized nanocrystals form stable suspensions in non-polar solvents, these suspensions are employed for EPD.

The origin of surface charge on sterically stabilized nanocrystals is relatively unknown. The charging mechanisms in sterically-stabilized nanocrystal suspensions should be different from that of electrostatically-stabilized particle suspensions. In electrostatically-stabilized systems, surface charges develop because of adsorption of polar solvent molecules, protons, and free ions in the solvent as described in the previous section.[51,52,89] The polar solvent molecules, protons, and free ions are absent or are present in negligible amounts as impurities in non-polar solvents. The role of such impurities, if present, in charging of nanocrystals is not known. Thermal charging of nanocrystals in suspension has been debated as origin of charge in CdSe, ZnSe, Au, Fe_3O_4, and Ag nanocrystals.[83,104] Also, charge tuning on the nanocrystals was observed through the addition of ligands and/or removal of ligands via cleaning steps.[59] Since a fraction of the ligands is detached during each step of nanocrystal cleaning, the nanocrystal surface charge can be altered. The number of nanocrystal cleaning steps was optimized to deposit homogeneous CdSe films. A simi-

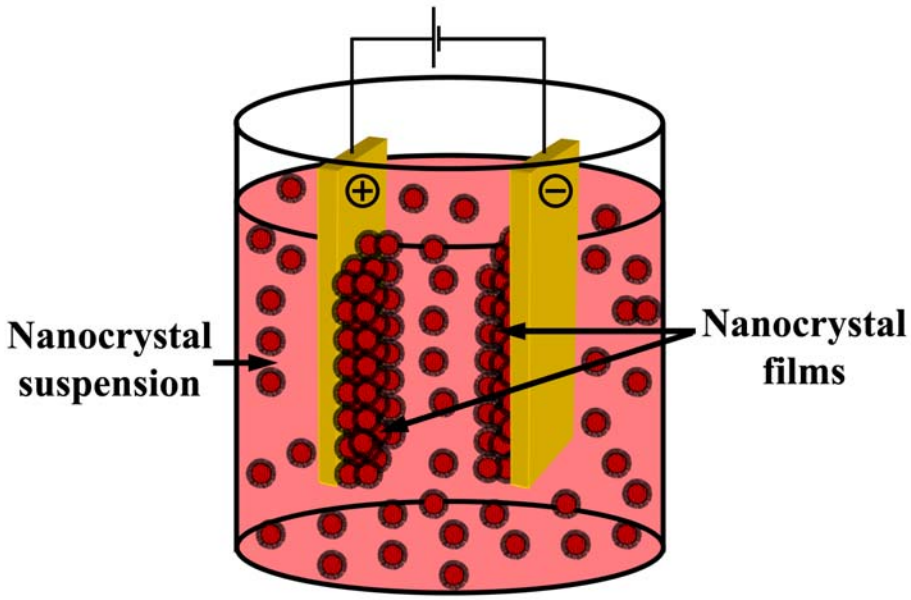

Figure 3.4: Schematic of EPD in non-polar solvent. Typically, surface functionalized nanocrystals are deposited with this technique. Nanocrystal films are generally formed on both the electrodes, suggesting the presence of positively and negatively charged nanocrystals.

lar nanocrystal cleaning approach was taken to process the rare-earth oxide nanocrystals, which were deposited by EPD as described later in this dissertation.

Unlike conventional EPDs of particles performed in polar solvents, EPDs of nanocrystals performed in non-polar solvents have produced films on both electrodes (anode & cathode) as depicted in figure 3.4.[17,74,83,105] Typically, the nanocrystal films of similar thicknesses were deposited on both the electrodes, suggesting comparable number of positively and negatively charged nanocrystals in suspension. Islam *et al.* found interesting phenomenon when they performed EPD with mixtures of different nanocrystals (CdSe, Au, and γ-Fe_2O_3).[74] The addition of Fe_2O_3 nanocrystals to CdSe nanocrystal suspension deposited composite nanocrystals films on both the electrodes. In contrast, the deposition of CdSe nanocrystals was inhibited on the negative electrode when Au nanocrystals were mixed in the suspension. The CdSe nanocrystals did not deposit on the negative electrode when the density of Au nanocrystals in the suspension was ~ 1.2 % of the CdSe nanocrystal density. The plausible explanations for the observed inhibition phenomenon were as follows:

(a) inhibit the charge-transfer process of positively charged CdSe nanocrystals at the electrode, (b) inhibit the sticking of these nanocrystals on the electrode, and (c) decrease the density of positively charged CdSe nanocrystals by transfer of charge to the Au nanocrystals in suspension. Significant research efforts are warranted to understand origin of charge on the nanocrystals, suspended in non-polar media. The success in such research efforts will allow further control over the nanocrystal charge and their deposition.

3.3 Experimental details

3.3.1 Electrodes

Electrically conductive electrodes of the following types were employed for EPDs.

1. Gold electrodes : Gold electrodes were prepared by evaporating gold onto glass substrate. Fisherfinest premier plain microscope glass substrates of 25 mm × 75 mm × 1 mm size were purchased from Fisher Scientific Inc. These substrates were cut into approximately 25 mm × 13 mm size pieces using a diamond scriber. To clean the glass pieces, they were sonicated sequentially in DI water, acetone, and propanol for 15 min each with an intermediate drying step with a stream of dry nitrogen. Next, the glass pieces were baked in an oven at 120 °C for 10 min. These glass pieces were employed for the thermal evaporation of chromium and gold. The gold pellets (99.99%) were purchased from J & J Materials Inc. and chromium-plated tungsten rods (4 in length) were purchased from Kurt J. Leskar Company. Since gold does not adhere well to glass, a thin layer of chromium, as an adhesive, was deposited on glass. First, ∼ 20 nm of chromium was evaporated onto the cleaned glass pieces, followed by the evaporation of ∼ 120 nm of gold. The base pressure was maintained between 2 - 5 μTorr throughout the thermal evaporation. These electrodes were employed for the deposition of Eu_2O_3 nanocrystals. [Chapter 4]

2. Indium-Tin-Oxide (ITO) electrodes : ITO-coated polished float glass substrates (SiO_2 passivated) of 25 mm × 75 mm × 1.1 mm size were purchased from Delta Technologies. Sheet resistance, R_S, of these substrates was 15-25 Ω. Similar to the gold

substrate, these substrates were cut into approximately 25 mm × 13 mm size pieces. These electrodes were cleaned with sequential sonication in acetone, ethanol, and hexane for 15 min each with an intermediate drying step with a stream of dry nitrogen and baked as described previously. Since ITO is a transparent and conducting material, the ITO electrodes were transparent. These electrodes were employed for the deposition of Eu_2O_3 nanocrystals. [Chapter 4]

3. Silicon electrodes : 5″ diameter p-type silicon wafers of 650 μm thickness with (100) crystallographic orientation were purchased from MEMC Electronic Materials Inc. The wafers had high electrical resistivity, 20-40 Ω·cm epitaxial layer grown on top of the low electrical resistivity, 0.005-0.025 Ω·cm substrate. The silicon electrodes of 25 mm × 13 mm size were cleaved from these wafers. The silicon electrodes were cleaned and baked as per the procedure for ITO electrodes. These electrodes were employed for the deposition of Gd_2O_3 nanocrystals. [Chapter 5]

4. Steel electrodes : 316L grade stainless steel sheets of 8″ × 12″ × 0.008″ size were purchased from McMaster Carr. The sheet was cut to form the electrodes of 25 mm × 13 mm size. These electrodes were sonicated sequentially in acetone and DI water for 15 min each with an intermediate drying step with a stream of dry nitrogen and baked as described previously. These electrodes were employed for the deposition of carbon nanotubes, Eu_2O_3 nanocrystals, and Fe_3O_4 nanocrystals. [Chapter 6]

3.3.2 Electrode assembly

A vertical parallel-plate electrode assembly with a gap was created for EPD. The electrodes of the same type were used as the anode and cathode in an electrode assembly. Figure 3.5 shows schematic of the electrode assembly. Conductive sides of the electrodes, depicted in black color in figure 3.5, are opposite of each other. To maintain the gap and electrical insulation between the two electrodes (anode and cathode), they were separated by a stack of the electrical grade Teflon sheets, purchased from McMaster Carr. To establish

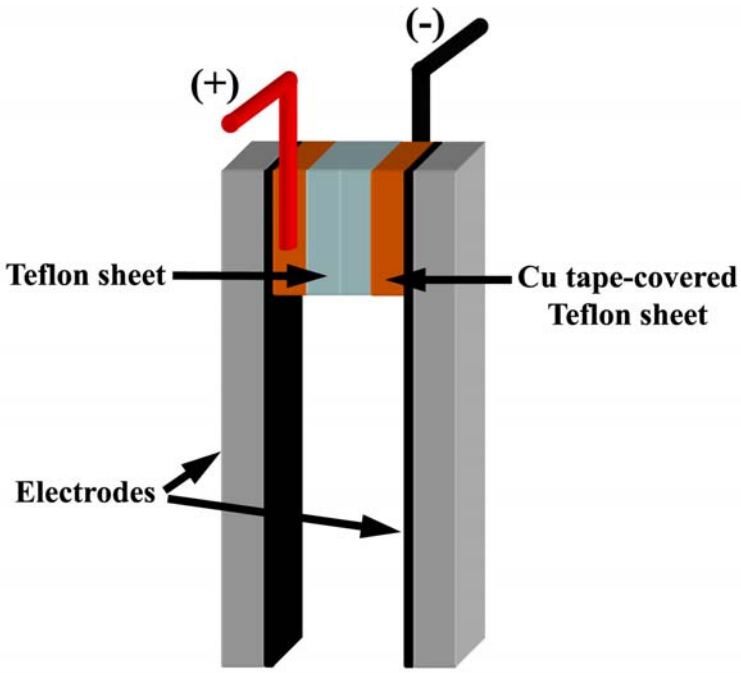

Figure 3.5: Schematic of an electrode assembly employed for EPD. Conductive sides of the electrodes, depicted in black color, are opposite of each other. A stack of Teflon sheets is used to maintain the gap and electric insulation between the electrodes (anode and cathode). Cu tape-covered Teflon sheets are used as a part of the stack to establish electrical contact between the voltage source and the electrodes.

electrical contact with the electrodes, two copper tape-covered Teflon sheets were used as a part of the Teflon sheet stack (Figure 3.5). These sheets were connected to wires, to which the electrical leads (positive & negative) from a power source were attached. Typically, a stack of six Teflon sheets produced the spacing of 5 mm between the electrodes. A clamp was used to hold the entire electrode assembly together. This electrode assembly technique was easy, quick, and consistent.

3.3.3 EPD system

A computer-controlled EPD system is used to perform all the EPD experiments. Figure 3.6 shows the EPD system, which comprises the EPD chamber, XYZ stage and controller, voltage sources, computer, and the custom LabView program. The EPD experiments were performed inside the EPD chamber, which is made of 0.5 inch thick Plexiglass. Since high voltages and flammable solvents are used in EPD experiments, the EPD chamber acts primarily as a safety chamber. In addition, the chamber can be purged with inert gas to perform EPD experiments in an oxygen-free environment. All the EPD experiments conducted and reported in this thesis were performed in an air environment. A computer-controlled XYZ stage is used to mount the electrode assembly and control its movement precisely during deposition. The dc voltage sources, a Keithley 6517A and a BK Precision 1787B, are integrated into the EPD system for application of the dc voltage. Also, these sources measure current flowing through EPD suspension during deposition. A Keithley 6517A electrometer is capable of applying dc voltage between 0-1000 V and measuring current between 200 pA - 20 mA. A BK Precision 1787B voltage supply can apply dc voltage in the range of 0-72 V and can measure current in the range of 0-1.5 A. The voltage sources are interfaced with a Windows XP desktop computer via RS-232 interface, while XYZ stage is interfaced via a National Instruments controller. A custom EPD program, written in LabView, accepts the deposition parameters and executes the deposition. Figure 3.7 shows visual interface of the EPD program. The EPD parameters (beaker position, deposition

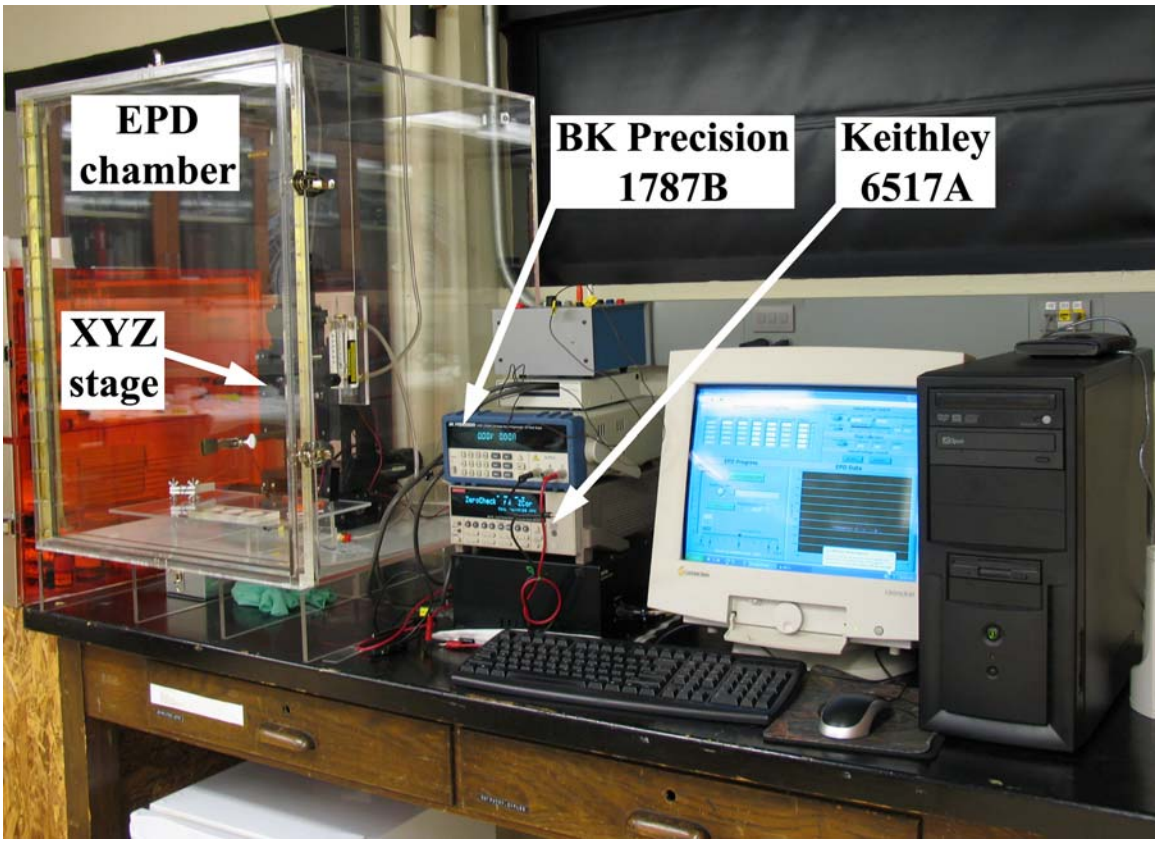

Figure 3.6: A computer-controlled EPD system used for depositions. EPD chamber acts primarily as a safety chamber. An electrode assembly is mounted on the XYZ stage for its precise movement during deposition. One of the two voltage sources, a Keithley 6517A and a BK Precision 1787B, is used to apply dc voltage and measure current during deposition.

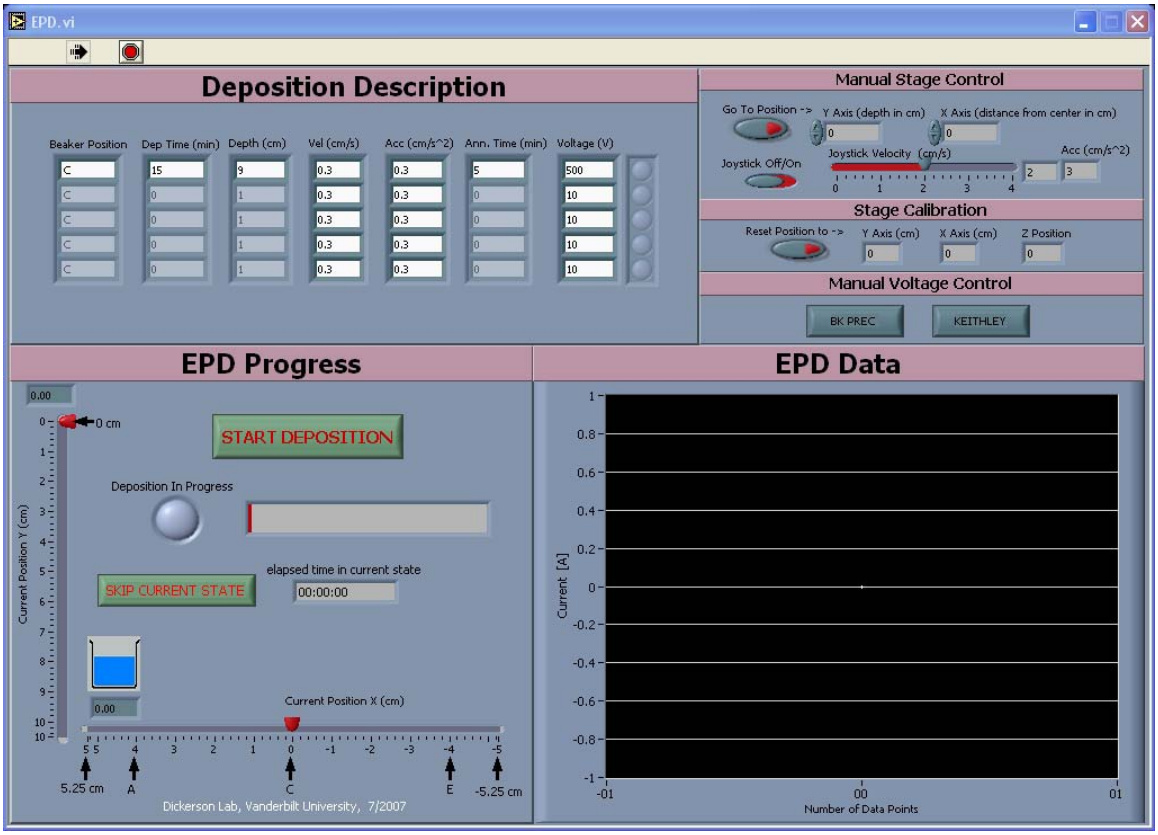

Figure 3.7: Visual interface of the EPD program, written in LabView software. The deposition parameters are entered into the program and deposition sequence is executed. Profile of current flowing through the EPD suspension during deposition is displayed in real-time.

time, applied voltage, annealing time, electrode insertion/extraction speed, acceleration and depth) are entered into the "Deposition Description" section. Each row of "Deposition Description" section represents parameters for a single deposition. The EPD system is capable of executing sequential depositions. The "EPD Progress" section shows real-time electrode position and elapsed time of deposition/annealing stage. The "EPD Data" section displays real-time profile of current flowing through EPD suspension. Jonathan Hood, a REU student, implemented the computer-controlled capabilities of the EPD system and developed the EPD program.

3.3.4 EPD experiment

In a typical EPD experiment, an electrode assembly is built, mounted on the XYZ stage, and electrical connection with the required voltage source is established. Next, 15 ml suspension of the nanomaterials (nanocrystals/nanotubes) of required concentration is prepared with the suitable solvent (hexane for nanocrystals and water for carbon nanotubes) in a 15 ml glass beaker. All deposition parameters are entered into the EPD program, which is then executed. The deposition sequence is as follows: application of the dc voltage, insertion of the electrode assembly into the EPD suspension (approximate deposition area: 18 mm $\times$ 13 mm), deposition for the specified time (typically 10 - 60 min), and extraction of the electrode assembly from the suspension, and drying in air for the specified time (typically 5 - 15 min) while maintaining the applied voltage. Within the scope of this dissertation, Eu_2O_3, Gd_2O_3, iron oxide (Fe_3O_4) nanocrystals and carbon nanotubes were deposited by EPD, as described later in the dissertation.

CHAPTER IV

GROWTH OF TRANSPARENT & LUMINESCENT FILMS OF Eu_2O_3 NANOCRYSTALS

4.1 Introduction

The Eu_2O_3, Tb_2O_3, and Gd_2O_3:Eu^{3+} materials have strong absorption in UV region and have weak absorption in visible region. Small-diameter nanocrystals of these oxides should scatter a small fraction of visible light. When these nanocrystals are assembled into films, the films should have minimal light scattering losses, and thereby, enhance the transmission of light throughout the visible spectrum as observed for cerium-doped yttrium aluminum garnet (YAG:Ce^{3+}) nanocrystals.[106] These nanocrystal films have potential applications in UV absorption coatings, photoactive coatings, and solid-state lighting devices.[107,108] In these applications, the deposition of transparent films facilitates efficient transmission of visible light. As a test case, we selected Eu_2O_3 nanocrystals to assemble their films via electrophoretic deposition and to study their optical properties via transmission and photoluminescence spectroscopies. Since the synthesis reaction that produced $\sim$ 3.0 nm diameter nanocrystals had low yield (< 30 %), we selected ~ 2.4 nm diameter Eu_2O_3 nanocrystals between the two remaining nanocrystal sizes as a test case. Electrophoretic deposition, employed to produce Eu_2O_3 nanocrystal films, offers control over thickness of the film and the uniformity via EPD process parameters (applied voltage, deposition time, and nanocrystal concentration). Investigation of the effect of these parameters on the thickness and uniformity of transparent films of the Eu_2O_3 nanocrystals is important to understand the growth of these films.

In this chapter, the investigation of the fabrication of the transparent films of Eu_2O_3 nanocrystals via electrophoretic deposition is discussed. Morphologies of these films were

analyzed with scanning electron microscopy and atomic force microscopy and our findings are discussed. Optical properties of the nanocrystals and their films were characterized with absorption, transmission, and photoluminescence spectroscopies and are described here. We investigated the effect of EPD processing parameters (applied voltage, deposition time, and nanocrystal concentration) on the uniformity of the transparent films and the results are discussed, which provided insight into the growth of the films.

The research described in this chapter has been published in the following journal article:

- S. V. Mahajan and J. H. Dickerson, Understanding the growth of Eu_2O_3 nanocrystal films made via electrophoretic deposition, *Nanotechnology*, **21** 145704, (2010)

4.2 Experimental details

4.2.1 Film deposition

Colloidal Eu_2O_3 nanocrystals ($\sim$ 2.4 nm dia.), capped with oleic acid, were produced as per the synthesis technique described in Chapter II [Section 2.2.1 & 2.2.2]. A typical precipitation-centrifugation procedure, described in Chapter II (Section 2.2.3), was employed to clean the nanocrystals. The 10×-cleaned Eu_2O_3 nanocrystals were suspended in hexane for electrophoretic deposition. The Eu_2O_3 nanocrystal films were deposited onto two types of electrodes: gold electrode and ITO electrode (Section 3.3.1). A typical EPD sequence, as mentioned in Chapter III (Section 3.3.4), was followed for all the depositions. We performed EPD of the Eu_2O_3 nanocrystals at different applied voltages (250, 500, 750, and 1000 V) and with different nanocrystal concentrations (1×10^{15} NC/cm^3, 2×10^{15} NC/cm^3 and 4×10^{15} NC/cm^3).

4.2.2 Characterization techniques

Optical properties of the Eu_2O_3 nanocrystals, employed for film deposition, were measured with absorption and photoluminescence spectroscopy. Electrophoretic mobility of

the nanocrystals was measured in hexane from dynamic light scattering (DLS) experiments, performed on a Malvern Nano ZS system. A Leitz microscope connected to CFM-USB-2 camera from Angstrom Sun Technologies Inc was used to acquire optical micrographs of the nanocrystal films. Morphological surface analyses of the films were performed using a Hitachi S-4200 scanning electron microscope and a Digital Instruments Nanoscope III atomic force microscope in tapping mode. Elemental analyses of the electrodes were conducted using energy dispersive spectroscopy on the electrodes to confirm the nanocrystal deposition. We measured film thickness using a Veeco Dektak 150 surface profiler. The transmission and photoluminescence spectra of the nanocrystal films were acquired using a Cary 5000 spectrophotometer and a Fluorolog-3-FL3-111 spectrophotofluorometer, respectively.

4.3 Results and discussion

4.3.1 Nanocrystal characterization

The Eu_2O_3 nanocrystals, employed for film depositions, were characterized with absorption and photoluminescence spectroscopies. Figure 4.1(a) shows the absorption spectrum of the nanocrystals. The strong absorption in the ultra-violet (UV) region was observed from these nanocrystals, while the absorption was weak in the visible region. The strong absorption peak at 225 nm was attributed to the transition between the ground state and the charge-transfer state of the Eu-O bond.[3,29,30] In addition, the weak absorption peak at 395 nm, shown in the inset to figure 4.1(a), arose from the $4f \rightarrow 4f$ transition.[30] Figure 4.1(b) shows the photoluminescence spectrum of the Eu_2O_3 nanocrystals exhibiting the characteristic luminescence peaks [Figure 2.9(a)].[41]

4.3.2 Film characterization

Figure 4.2(a) shows a typical optical micrograph of a Eu_2O_3 nanocrystal film, deposited on a gold electrode (anode). The nanocrystal film was assembled with an applied voltage of 250 V and a nanocrystal concentration of 2×10^{15} NC/cm^3. The film had yel-

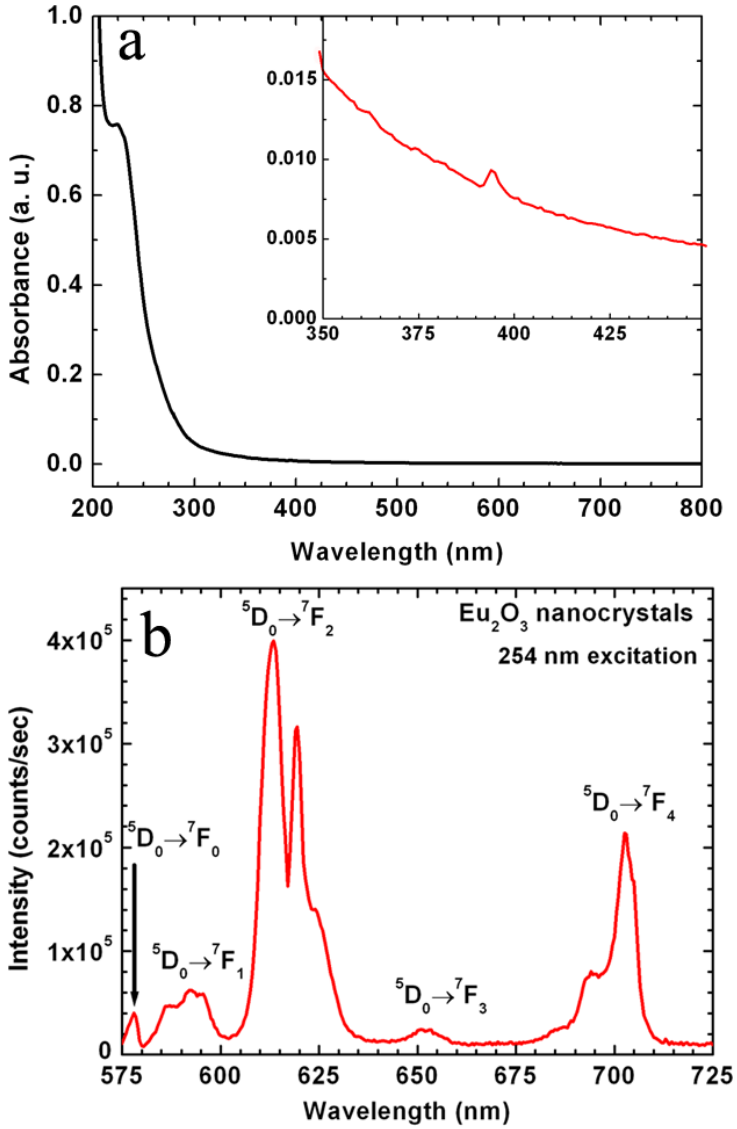

Figure 4.1: (a) Absorption spectrum of the Eu_2O_3 nanocrystals, exhibiting strong absorption in UV region due to a transition from the ground state to the charge-transfer-state of the Eu-O bond and (inset) a weak absorption peak at 395 nm due to the $4f \rightarrow 4f$ transition; (b) Photoluminescence spectrum of the nanocrystals, exhibiting peaks arising due to $^5D_0 \rightarrow {}^7F_J$ (J = 0-4) transitions.

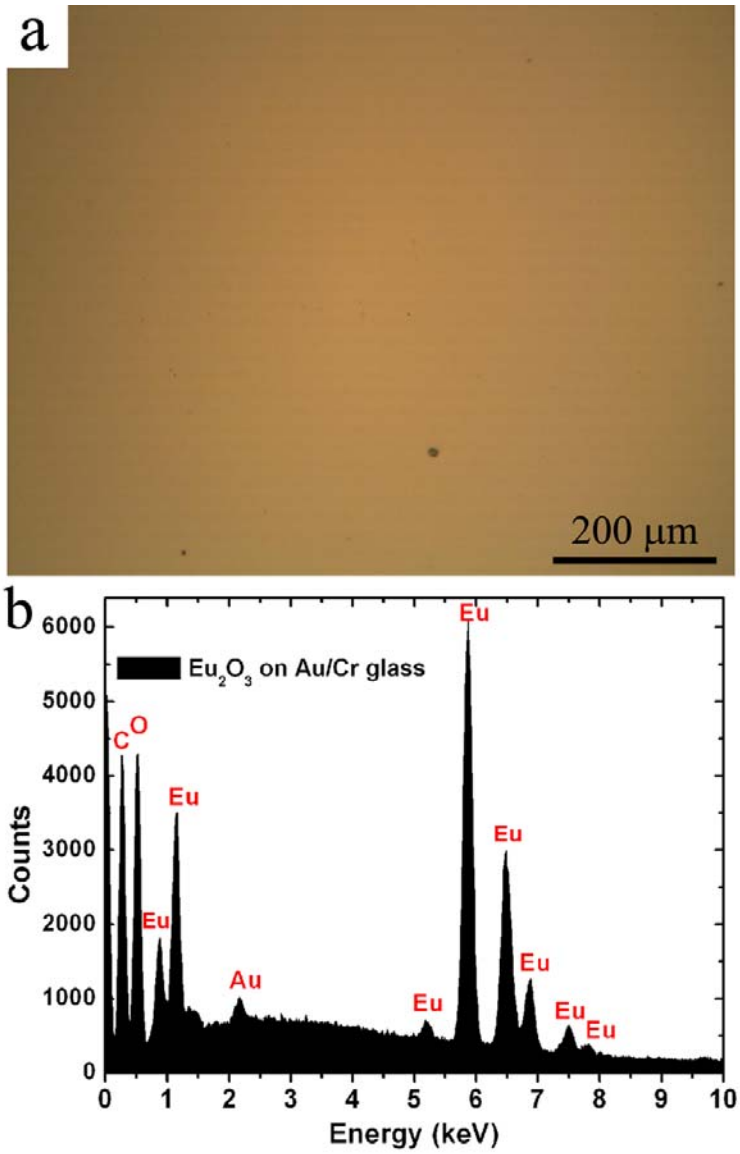

Figure 4.2: (a) Optical micrograph of the Eu_2O_3 film deposited on a gold substrate, which appears golden in color because of the background gold substrate and the high transparency of the film; (b) EDS spectrum of the film deposited on a gold substrate, which reveals the presence of europium, oxygen, and carbon that originates from the oleic acid-functionalized Eu_2O_3 nanocrystals and the gold from the substrate.

lowish color when observed under the optical microscope. (Figure 4.2) The observed color was attributed to the color of the underlying gold substrate because of high transparency of the film. The film was continuous with no visible defects larger than approximately 5 μm, which confirmed uniformity of the film of nanocrystals over a large size (film size >>> nanocrystal size). The film that was deposited on the cathode had a comparable appearance. To verify deposition of the Eu_2O_3 nanocrystals on the gold-electrodes, we performed EDS for elemental analysis. 4.2(b) shows the EDS spectrum of the nanocrystal film, deposited on the anode. We observed the characteristic X-ray emission peaks of europium (L & M), oxygen (K), and carbon (K), which confirmed the deposition of the oleic acid-functionalized Eu_2O_3 nanocrystals. Also, the characteristic peak of gold was detected because of the underlying gold substrate. Similarly, deposition of the Eu_2O_3 nanocrystals was confirmed on the cathode. The thickness of the film was $\sim$ 110 nm, which was measured using surface profilometry.

The Eu_2O_3 nanocrystal films, excited with UV light, exhibited characteristic red luminescence as seen in figure 4.3. Figure 4.3(a) shows a photograph of the nanocrystal-deposited ITO-electrodes (anode & cathode) and bare ITO-electrode, illuminated with a UV light source (254 nm). The red luminescence is clearly visible from both the electrodes. Bare ITO-electrode do not exhibit any photoluminescence. To excite the nanocrystal films, the electrodes were kept face-down to avoid absorption of UV light in glass. Figure 4.3(b) shows the PL spectra of the anode and cathode upon UV excitation (254 nm). The spectra showed all of the peaks corresponding to the $^5D_0 \rightarrow {}^7F_J$ (J = 0-4) energy transitions of the Eu^{3+} ion. The spectra were identical to the spectrum of the Eu_2O_3 nanocrystals [Figure 4.1(b)] confirming deposition of the Eu_2O_3 nanocrystals. Thus, the PL spectra of cathode and anode confirmed the deposition of the Eu_2O_3 nanocrystal film on both electrodes.

Surface morphology of the nanocrystal film was investigated with SEM and AFM. Figure 4.4(a) shows the SEM image of the nanocrystal film, deposited on the anode. The nanocrystal film was topologically smooth and uniform. The film on the cathode had

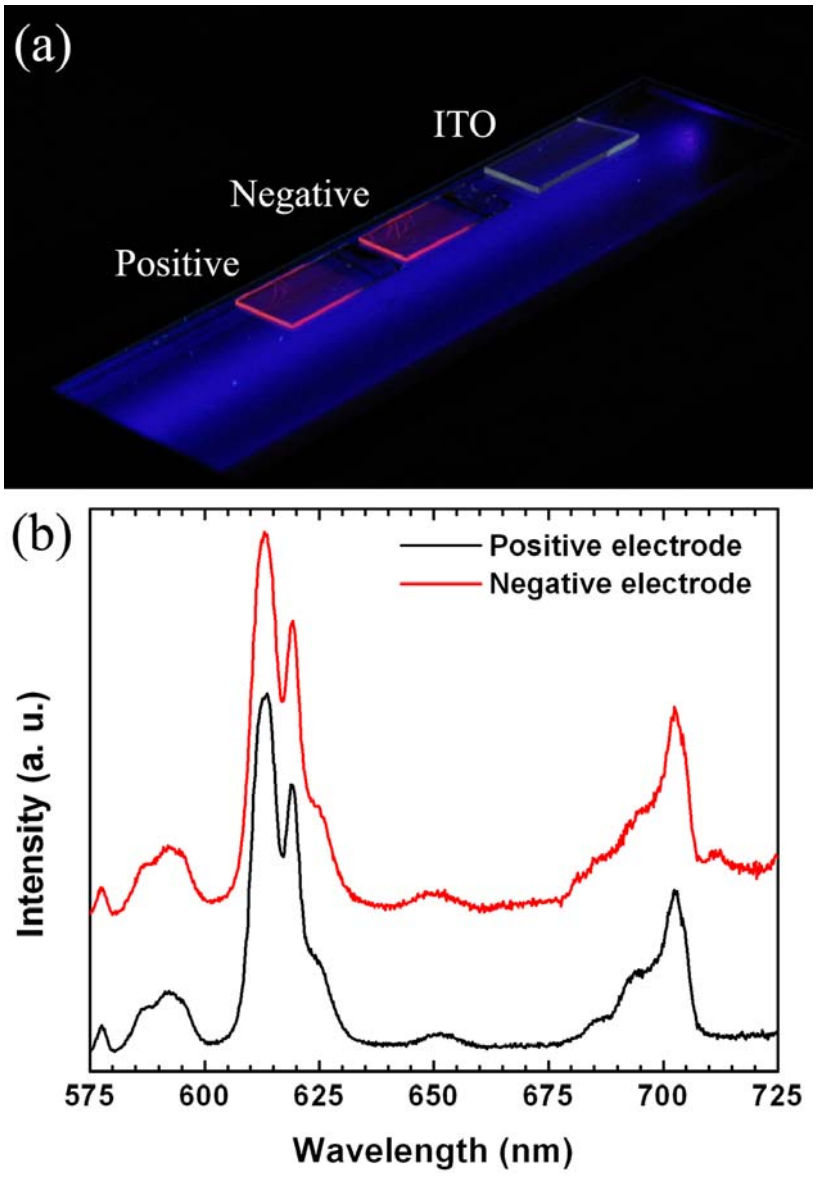

Figure 4.3: (a) Photograph of the Eu_2O_3 nanocrystals films, deposited on the anode and cathode that were excited with UV source (254 nm). Red luminescence is clearly visible from both the electrodes. Bare ITO-coated glass do not exhibit any photoluminescence; (b) PL spectra of the Eu_2O_3 nanocrystal films deposited on the anode and cathode. The spectra are identical to the spectrum of the Eu_2O_3 nanocrystals. PL spectra are shifted vertically for clarity.

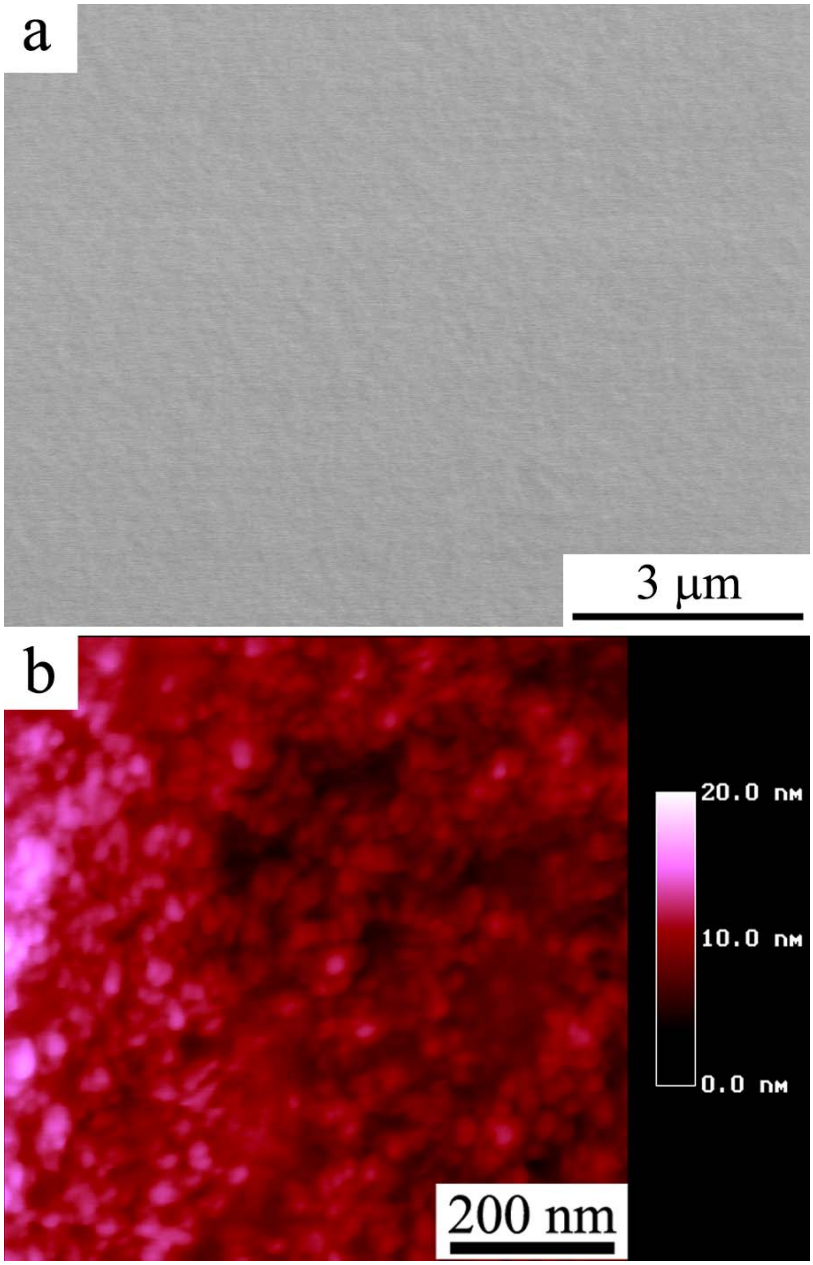

Figure 4.4: (a) SEM image of the nanocrystal film; (b) AFM image of the nanocrystal film, which reveals deposition of the nanocrystal agglomerates of $\sim$ 15 nm size. RMS roughness of the film determined from the AFM image is 1.4 nm.

comparable surface morphology. We performed high-resolution surface topological analysis of the nanocrystal film with AFM. The AFM image, shown in figure 4.4(b), revealed that the film was composed of agglomerates of the Eu_2O_3 nanocrystals, approximately 15-20 nm in diameter. The apparent deposition of agglomerates of the nanocrystals instead of individual nanocrystals motivated us to identify the formation of any agglomerates in EPD suspension prior to the deposition. We prepared new TEM samples for imaging by dropcasting the EPD suspensions onto the grids. These new samples confirmed the absence of any agglomerates of the Eu_2O_3 nanocrystals in the EPD suspension. Thus, the agglomeration of the nanocrystals likely occurred under the influence of the electric field during EPD. The agglomeration may have occurred at one or more of the following stages: a) immediate agglomeration upon application of the voltage to the electrodes in the EPD suspension; b) agglomeration near the electrodes following an increase in the nanocrystal concentration due to locomotion of charged nanocrystals towards the respective electrodes; c) reorganization of the deposited nanocrystals at the electrode leading to agglomeration. Even though the nanocrystals agglomerated under the influence of an electric field, the extent of agglomeration was limited because of sufficient ligand coverage on the nanocrystal surface. The deposited agglomerates packed close to each other, forming a continuous and densely arranged film [Figure 4.4(b)]. Nonetheless, these films were particularly smooth. The root mean square (RMS) surface roughness, determined from the AFM image of the film, was ~ 1.4 nm, which was smaller than the diameter of one nanocrystal. A plausible reason for the high smoothness of the films is that a small fraction of the nanocrystals was deposited along with the agglomerates of the nanocrystals. Thus, SEM and AFM imaging confirmed the formation of smooth, uniform, and densely packed film of the agglomerates of the Eu_2O_3 nanocrystals.

To demonstrate transparency of the Eu_2O_3 nanocrystal film, an optical micrograph of a patterned silicon substrate was recorded through the nanocrystal film that was deposited on the ITO electrode [Figure 4.5(a)]. The patterned substrate was clearly visible,

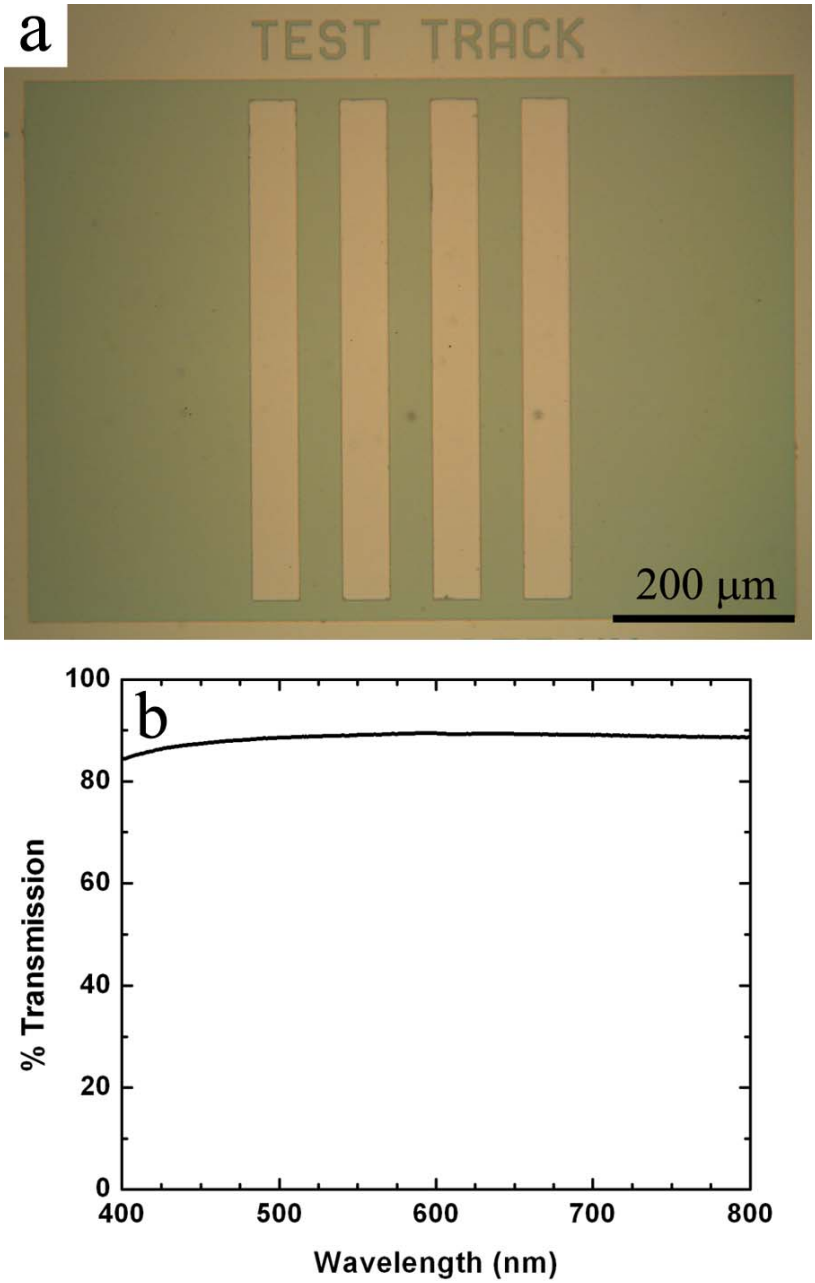

Figure 4.5: (a) Optical micrograph of the patterned silicon substrate recorded through the nanocrystal film deposited on ITO-coated glass substrate, which reveals high transparency of the EPD film; (b) Transmission spectrum of a cast film of the Eu_2O_3 nanocrystals, showing high transparency in visible region.

which confirmed the formation of highly transparent film. We performed transmission spectroscopy on the same film to determine its transmission properties in the visible region. Intensity oscillations of transmitted light were seen in the visible transmission spectrum, which were due to Bragg interference because of the thickness of the film ($\sim$ 110 nm thick). To measure the transmission of the film, it was difficult to make a thick film ($>$ 2 μm) with high uniformity using EPD. Hence, we deposited a $\sim$ 500 μm film on a glass substrate using a drop-cast technique. The nanocrystal film released from the substrate upon drying in air and could be handled to transfer onto another substrate. A small piece of the film was mounted on a sample holder such that it covered the transmission window completely. Prior to recording transmission spectrum of the nanocrystal film, a background transmission spectrum of air was collected and subtracted automatically from the spectrum of the nanocrystal film. Figure 4.5(b) shows the transmission spectrum of the drop-cast film, which reveals high transparency in visible region (>80%). Electrophoretically deposited thin film should have a comparable transmission considering the high transparency of the thick film. High transparency of the film was achieved by minimizing scattering loss of visible light within the nanocrystal film. The intensity of scattered light off of a nanoparticle within the visible region is best expressed with Rayleigh scattering equation, which is appropriate within the small size parameter limit x = $\pi d_{NC}/\lambda$, x << 1. For the average size (15 nm) of agglomerates of the Eu_2O_3 nanocrystals, x ranges between 0.12 - 0.06 in the visible spectral region. Hence, the use of Raleigh scattering theory is valid. Rayleigh scattering intensity per particle, I_s, is written as

$$I_s = \left(\frac{2\pi}{\lambda}\right)^4 \left(\frac{n^2-1}{n^2+2}\right)^2 \left(\frac{1+cos^2\theta}{2R^2}\right) \left(\frac{d_{NC}}{2}\right)^6 I_0 \tag{4.1}$$

where λ is the wavelength of the incident light, n is the refractive index of the particle, θ is the scattering angle, R is the distance to the particle from the point of observation, d_{NC} is the particle diameter, and I_o is the intensity of the incident light. Clearly, the small size of the Eu_2O_3 nanocrystal agglomerates within the film facilitated a reduction in scattering losses of visible light since the scattering intensity is proportional to sixth power

of the particle size. Thus, the small size of the Eu_2O_3 nanocrystal agglomerates and the low surface roughness was the key to achieve highly transparent films.

4.3.3 Growth of transparent films & EPD process parameters

Ability to control the thickness of our films is extremely important while maintaining the film quality. The Hamaker equation (Equation 3.1) along with the Hückel equation (Equation 3.3) correlates the deposit yield, w during EPD to the EPD suspension parameters (ζ, η, and ϵ_r) and the EPD process parameters (E, C, and t), which is written as,

$$w = \frac{2 \cdot \epsilon_0 \cdot \epsilon_r \cdot \zeta \cdot E \cdot A \cdot C \cdot t}{3 \cdot \eta} \tag{4.2}$$

Since the solvent (hexane) and electrode set-up (deposition area, $A = 18$ mm $\times$ 13 mm, 5 mm gap) for EPD were the same, the parameters (ϵ_r, η, and A) remained constant. The number of cleaning steps, employed to clean the nanocrystals, affected the coverage of surface capping ligands on the nanocrystals. Net charges possessed by the nanocrystals in solution are related to the coverage of ligands on the nanocrystal surface (steric stabilization). The Eu_2O_3 nanocrystals in solution were cleaned by the same process to maintain a similar zeta potential of the nanocrystals for all EPDs. The deposit yield (and film thickness) can be controlled via the EPD process parameters such as the electric field (E), the particle concentration (C), and the deposition time (t). For a deposition sequence with a constant applied voltage and a fixed initial concentration, the deposition rate decreases as the deposition time increases.[109] A decreasing particle concentration within the EPD suspension and an increasing voltage drop across the growing film of insulating/semiconducting nanoparticles also decreases the deposition rate. Zhitomirsky *et al* reported that the current density and deposition rate of hydroxyapatite decreased as a function of deposition time in non-aqueous polar solvent (isopropyl alcohol).[110] A decreasing current density through the particle suspension is an indication of a decreasing deposition rate. We have observed that the current density through our Eu_2O_3 nanocrystal suspension dropped at least 80% within ten minutes of the beginning of the deposition run. Since the deposition rate was expected

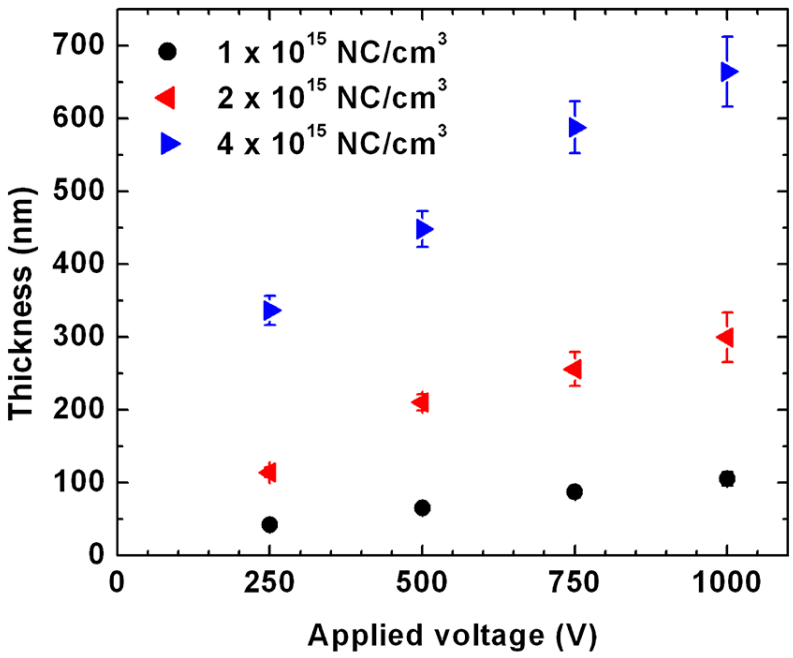

Figure 4.6: Thickness of the EPD film as a function of the applied voltage for different nanocrystal concentrations. Average film thickness is reported from the thickness measurements at different locations, and standard deviation is employed as the error bar. The large error bar indicates decreased film uniformity.

to be low at times beyond fifteen minutes of deposition time, we maintained the deposition time fixed at fifteen minutes for all EPD experiments and varied the applied voltage and the nanocrystal concentration to monitor the uniformity and thickness of the films.

We performed EPD of the Eu_2O_3 nanocrystals at different applied voltages (250, 500, 750, and 1000 V) and with different nanocrystal concentrations (1×10^{15} NC/cm^3, 2×10^{15} NC/cm^3 and 4×10^{15} NC/cm^3) to understand their effect on thickness and uniformity of the nanocrystal film. Thickness measurements were conducted at five locations on three different samples, and the average thickness was determined with the standard deviation of the thicknesses as the error bar. Hence, the error bar conveys the thickness uniformity of the film. Figure 4.6 shows the graph of the nanocrystal film thickness as a function of the applied voltage for different nanocrystal concentrations. The film thickness increased as a function of the applied voltage and nanocrystal concentration, as expected. When we increased the applied voltage, more nanocrystals moved toward the electrodes under the

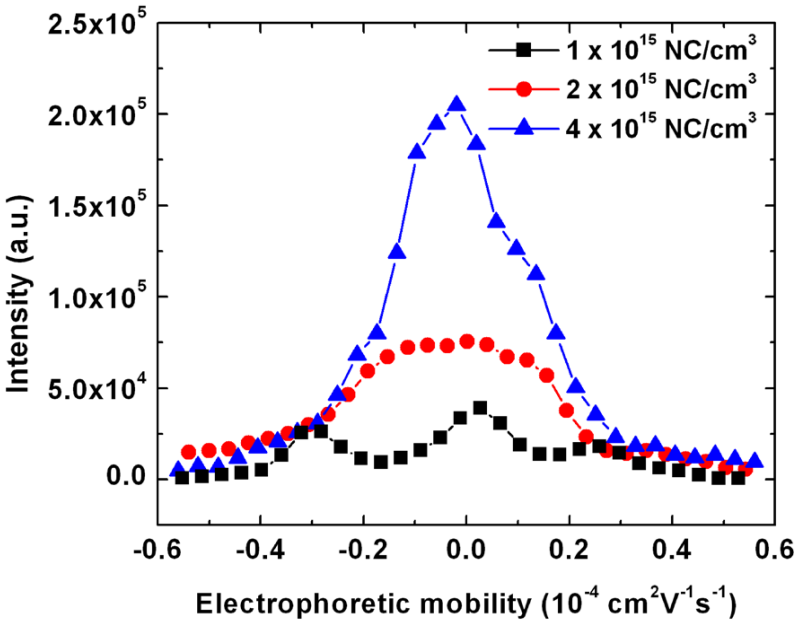

Figure 4.7: Electrophoretic mobility measurements of the EPD suspensions with different nanocrystal concentrations.

influence of increased electric field and deposited to form films. Similarly when we increased the nanocrystal concentration, more charged nanocrystals were available for the deposition, which led to the formation of thicker films. By performing electrophoretic mobility measurement on the EPD suspensions of different nanocrystal concentration, we confirmed that more nanocrystals were available for deposition as the nanocrystal concentration increased. Figure 4.7 shows that the scattering intensity of the particles increased with the nanocrystal concentration for a given electrophoretic mobility. Subsequently, the thickness of the nanocrystal film increased with the EPD process parameters (applied voltage and nanocrystal concentration). During EPD, a constant applied voltage was maintained, but the nanocrystal concentration of the EPD suspension decreased with time as the Eu_2O_3 nanocrystal film grew. The growth of the film slowed as the EPD progressed. The two factors that slowed down the growth were: a) the increasing voltage drop across the growing film of the insulating Eu_2O_3 nanocrystals; b) the depletion of charged nanocrystals from the EPD suspension. Since the voltage drop across the film increased as the film grew, effective volt-

age across the EPD suspension decreased because the applied voltage was constant. For a given nanocrystal concentration, thicker nanocrystal films were deposited when higher applied voltages were employed. The application of higher voltage between the electrodes facilitated increased effective voltage across the EPD suspension, resulting in thicker films. Since thicker films were deposited with the higher applied voltages for a given nanocrystal concentration, the nanocrystal suspension was not entirely depleted of charged nanocrystals. Also, the charged nanocrystals were not depleted because more nanocrystals were deposited from the same suspension when the electrodes were re-inserted. Thus, the increasing voltage drop across the growing Eu_2O_3 nanocrystal film was primarily responsible for restricting growth of the film.

EPD process parameters (applied voltage and nanocrystal concentration) altered the uniformity of the Eu_2O_3 nanocrystal film (Figure 4.6). For a given nanocrystal concentration, film uniformity decreased (larger error bar) as the applied voltage increased. Also, the thickness uniformity decreased (larger error bar) for higher nanocrystal concentrations for a given applied voltage. Although the films were increasingly non-uniform, we observed a particular pattern in thickness variation. The films were thick towards the edges of the electrode and were thin in the center of the electrode, which suggested the presence of strong fringe electric fields near the edges of the electrode. Naturally, the fringe field increased with the applied voltage; therefore, more nanocrystals deposited near the edges of the electrode, increasing non-uniformity of the film. Also, the non-uniformity of the film increased when the nanocrystal concentration increased. Since the same EPD set-up (deposition area: 18 mm $\times$ 13 mm electrode, 5 mm gap) was employed for all the depositions, variation in the thickness uniformity of the film was purely a result of changes in the EPD process parameters. Thus, the nanocrystal concentration and the applied voltage can be increased to increase deposition rate or film thickness, but at the expense of film uniformity.

The microscopic morphology and the elemental composition of our EPD films were analyzed as a function of film thickness. This study identifies whether the nanocrystals

underwent any compositional or topological modification while being deposited under the EPD electric field. We chose to investigate films produced from our highest nanocrystal concentration, 4×10^{15} NC/cm^3, as they yielded the most substantial deviations from uniformity in the topology, substrate coverage, and roughness in our films when assessed at macroscopic level. Since these films were deposited with different applied voltages, effect on their elemental composition, if any, would be identified. We surmised that such film characteristics would yield largest changes in microscopic/nanoscale topology, morphology, and compositional changes, if any such change existed. We performed AFM imaging and EDS analysis on the four films with different thicknesses, which were deposited at four different applied voltages. Figure 4.8(a-d) shows SEM images of the EPD films deposited at 250 V, 500 V, 750 V, and 1000 V, respectively. The films were composed of agglomerates of the Eu2O3 nanocrystals, which were approximately 130-160 nm in diameter. These agglomerates formed from 4×10^{15} NC/cm^3 nanocrystal concentration were much larger than the observed agglomerates deposited from the lower 2×10^{15} NC/cm^3 nanocrystal concentration (Figure 4.4(b)). The agglomerate size was consistent across individual films and was nearly identical for different applied voltages [Figure 4.8(a-d)]. The smoothness of all the films was comparable. The RMS surface roughness, determined from an analysis of the AFM images of the films, varied between $\sim$ 1.6 and 1.8 nm. This roughness was still smaller than the diameter of one nanocrystal. Thus, the films maintained a smooth topography as a function of film thickness/applied voltage.

Additionally, we performed EDS analysis of the films to juxtapose their compositions. EDS analyses were performed on small, cleaved sections of the EPD films placed onto silicon substrates rather on the original ITO-coated glass substrates. This step was necessary since the contribution of the oxygen signal from the substrate dominated the oxygen signal from the Eu_2O_3 nanocrystal films. Silicon substrates were chosen because their EDS peaks do not coincide with the europium and oxygen peaks. Figure 4.8(e-h) shows the EDS graphs of the EPD films, deposited at 250 V, 500 V, 750 V, and 1000 V,

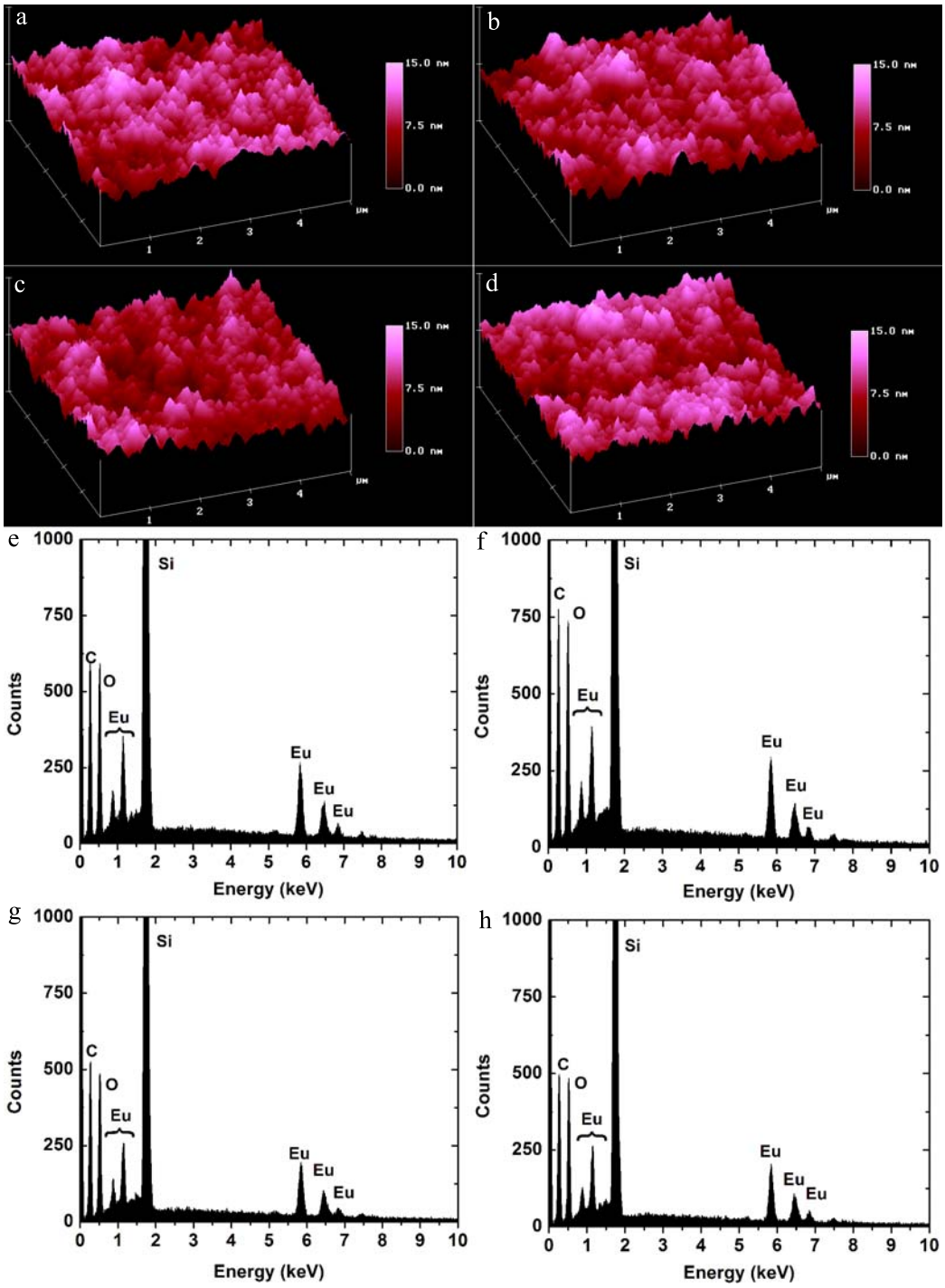

Figure 4.8: AFM images (a, b, c, and d) and EDS (e, f, g, and h) of the nanocrystal films deposited with the nanocrystal suspension concentration of 4×10^{15} NC/cm^3 at the applied voltages of 250 V, 500 V, 750 V and 1000 V, respectively. The AFM images of the films reveal the agglomerate size of $\sim$ 130-160 nm and RMS roughness of $\sim$ 1.6-1.8 nm. The morphology and composition of the films were comparable.

respectively. To compare the composition of the nanocrystals, we monitored the intensity of the oxygen peak (K line: 0.52 keV) relative to the intensity of the europium peak (M line: 5.84 keV). The average ratio of intensities, 2.32 $\pm$ 0.13, was within five percent of all four of the intensity ratios, which confirmed that the composition of the nanocrystals in the films did not change as a function of or because of the applied voltage. Thus, these analyses confirmed that the morphology, composition, and topology on the film at microscopic level remained consistent as the film thickness increased.

4.4 Summary

Transparent films of $\sim$ 2.4 nm diameter Eu_2O_3 nanocrystals were produced successfully using EPD technique. The films composed of agglomerates ($\sim$ 15 nm) of Eu_2O_3 nanocrystals, which likely formed under the influence of the electric field applied during EPD. The small size of the agglomerates scattered a small fraction of visible light, which reduced light scattering losses, and thus, enhanced transparency of the film (>80%) in visible region. The films were uniform, smooth, and densely-packed. The films maintained very low RMS surface roughness ($\sim$ 1.4 nm). The effect of the EPD process parameters (applied voltage and nanocrystal concentration) on growth of the transparent films was studied. To increase deposition rate or film thickness, the nanocrystal concentration and the applied voltage can be increased, but at the expense of film uniformity. The growth of transparent films was limited by increasing voltage drop across the growing film of Eu_2O_3 nanocrystals. The nanocrystal agglomerates of larger size were formed when the nanocrystal concentration was increased. Morphology at nanoscale and elemental composition of the films for different applied voltages were comparable.

CHAPTER V

Gd_2O_3 NANOCRYSTAL FILMS: UNDERSTANDING THE DIELECTRIC PROPERTIES

5.1 Introduction

Gadolinium oxide (Gd_2O_3) in its crystalline and amorphous phases has been considered as a replacement gate oxide material for silicon dioxide. The high dielectric constant ($\kappa = 14$) and the large band gap ($E_g = 5.5$ eV) are the two characteristic properties of Gd_2O_3 that are important and that have motivated this consideration. Dielectric properties of the amorphous and crystalline Gd_2O_3 films as the gate oxide in metal-oxide-semiconductor (MOS) and metal-oxide-semiconductor-field-effect-transistor (MOSFET) structures have been investigated.[4,111–113] Recently, dielectric studies of amorphous Gd_2O_3 films, embedded with Gd_2O_3 nanocrystals, revealed intriguing charge-storage characteristics of the nanocrystals.[114] Similarly, charge-storage characteristics were observed in other nanocrystal-based materials, such as metallic (Au, Ru, Ni, and Co)[115–117] and semiconducting (Si and Ge)[118,119] nanocrystal-embedded MOS architectures for non-volatile memory (NVM) applications. In such structures, nanocrystal-confined states, the states at the interface of nanocrystal-dielectric (i. e. nanocrystal surface), and the defect sites inside nanocrystals are responsible for the charge-storage behavior.[115,120,121] Our colloidal Gd_2O_3 nanocrystals may exhibit comparable charge-storage characteristics because of the unpassivated surface states that can arise due to the detachment of some fraction of the nanocrystals' surface capping ligands during nanocrystal cleaning procedure.[17,41] Investigation of dielectric properties of films composed entirely of colloidal Gd_2O_3 nanocrystals may provide insight into this subject.

In this chapter, investigation of the dielectric properties of our Gd_2O_3 nanocrystal

films is discussed. MOS capacitor structures with a colloidal Gd_2O_3 nanocrystal film as the gate oxide layer were fabricated for the study. The nanocrystal films are produced by electrophoretic deposition. High-frequency capacitance-voltage (C-V) measurements of these MOS structures were conducted to probe the dielectric properties. The observed hysteresis in the C-V curve illustrates the charge-storage behavior of the nanocrystal films. The effective dielectric constant of the nanocrystal films (κ) is determined and packing density of the nanocrystal film is calculated.

The research described in this chapter has been published in the following journal article:

- S. V. Mahajan and J. H. Dickerson, Dielectric properties of colloidal Gd_2O_3 nanocrystal films fabricated via electrophoretic deposition, *Appl. Phys. Lett.*, **96** 113105, (2010)

5.2 Experimental details

5.2.1 Materials and methods

The $\sim$ 2.4 nm diameter colloidal Gd_2O_3 nanocrystals, capped with oleic acid, were synthesized via the synthesis technique described in Chapter II [Section 2.2.1 & 2.2.2]. Since the synthesis reaction that produced $\sim$ 3.0 nm diameter nanocrystals had low yield ($<$ 30 %), we selected $\sim$ 2.4 nm diameter Gd_2O_3 nanocrystals as a test case. The nanocrystals were cleaned in ethanol using a typical precipitation-centrifugation procedure, described in Chapter II (Section 2.2.3). After cleaning the Gd_2O_3 nanocrystals, we suspended them in hexane for electrophoretic deposition. To fabricate MOS capacitor structures, the p-type silicon electrodes were employed. (Section 3.3.1)

Figure 5.1 shows a schematic of MOS capacitor architecture, fabricated using electrophoretic deposition and e-beam evaporation techniques. First, the oxide layer (Gd_2O_3 nanocrystal film) was deposited using EPD followed by the deposition of aluminum gate contacts by e-beam evaporation. We fabricated MOS capacitors with different nanocrystal

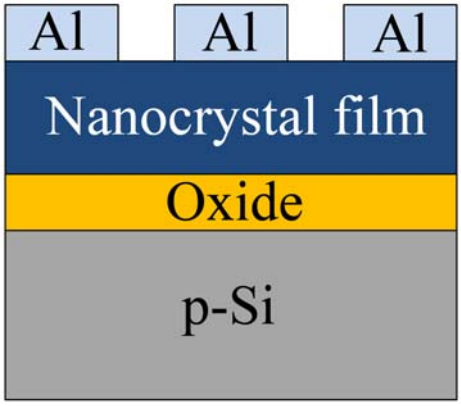

Figure 5.1: Schematic of MOS capacitor architecture. Nanocrystal film was deposited using electrophoretic deposition and aluminum gate contacts were deposited by e-beam evaporation.

film thicknesses. A typical EPD procedure, as mentioned in Chapter III (Section 3.3.4), was employed to deposit the Gd_2O_3 nanocrystal films. The films were deposited with a 500 V dc voltage. To vary nanocrysyal film thickness, we employed EPD suspensions of different nanocrystal concentrations (1.0×10^{15} NC/cm^3, 1.5×10^{15} NC/cm^3, 2.0×10^{15} NC/cm^3, and 2.5×10^{15} NC/cm^3). The nanocrystal films of the following thicknesses were deposited, which were measured with surface profilometry: 116 $\pm$ 10 nm, 179 $\pm$ 10 nm, 276 $\pm$ 10 nm, and 397 $\pm$ 15 nm. To complete the fabrication of the MOS capacitors, aluminum contacts (500 μm diameter and 300 nm thick) were deposited on the nanocrystal films via e-beam evaporation of aluminum using a shadow mask. Aluminum was employed as the gate material because of its suitable work function and cost effectiveness.

5.2.2 Characterization techniques

Elemental analyses of the electrodes using X-ray energy dispersive spectroscopy were conducted on the electrodes to confirm the nanocrystal deposition. Surface morphologies of the Gd_2O_3 nanocrystal films were probed using scanning electron microscopy and atomic force microscopy techniques. The film thicknesses were measured with surface profilometry. A small section of the film was wiped off with hexane-soaked cotton tip to expose the

underlying silicon substrate. A step profile was recorded with reference to the the exposed substrate to measure film thickness. High-frequency capacitance-voltage characteristics of the capacitors were collected at a frequency of 1 MHz and at a sweep rate of 50 mV/s, using a Keithley 590 CV analyzer on a Signatone probe station.

5.3 Results and discussion

5.3.1 Materials characterization of nanocrystal film

We performed EDS analyses of the electrodes to verify the deposition of Gd_2O_3 nanocrystal films. Figure 5.2(a) shows an EDS graph of the Gd_2O_3 nanocrystal film deposited on the anode. The EDS spectrum exhibits the X-ray emission peaks of the gadolinium (L & M), oxygen (K), carbon (K), and silicon (K), which are present due to the oleic acid-capped Gd_2O_3 nanocrystals on the silicon substrate. We observed comparable EDS spectrum of the film deposited on the cathode. Figure 5.2(b) shows an SEM image of the nanocrysrtal film (anode). This image provides a view of the assembly of the ultra-small nanocrystals at microscopic level. The film was topologically uniform and continuous over the large area (nanocrystal diameter $<<<$ image width). To probe the surface morphology of the film at nanoscale, we employed atomic force microscopy. The AFM image, shown in figure 5.2(c), revealed the presence of agglomerates of the Gd_2O_3 nanocrystals within the film. The agglomerates were approximately 10 - 15 nm in diameter and were densely packed together. The agglomeration of the Gd_2O_3 nanocrystals was similar to that of the Eu_2O_3 nanocrystals, reported in Chapter IV (Section 4.3.2). The RMS roughness of the film determined from an analysis of the AFM image was $\sim$ 1.6 nm, which also was smaller than the diameter of one nanocrystal. Thus, the Gd_2O_3 nanocrystal films deposited on the silicon electrodes were uniform, smooth, and densely packed.

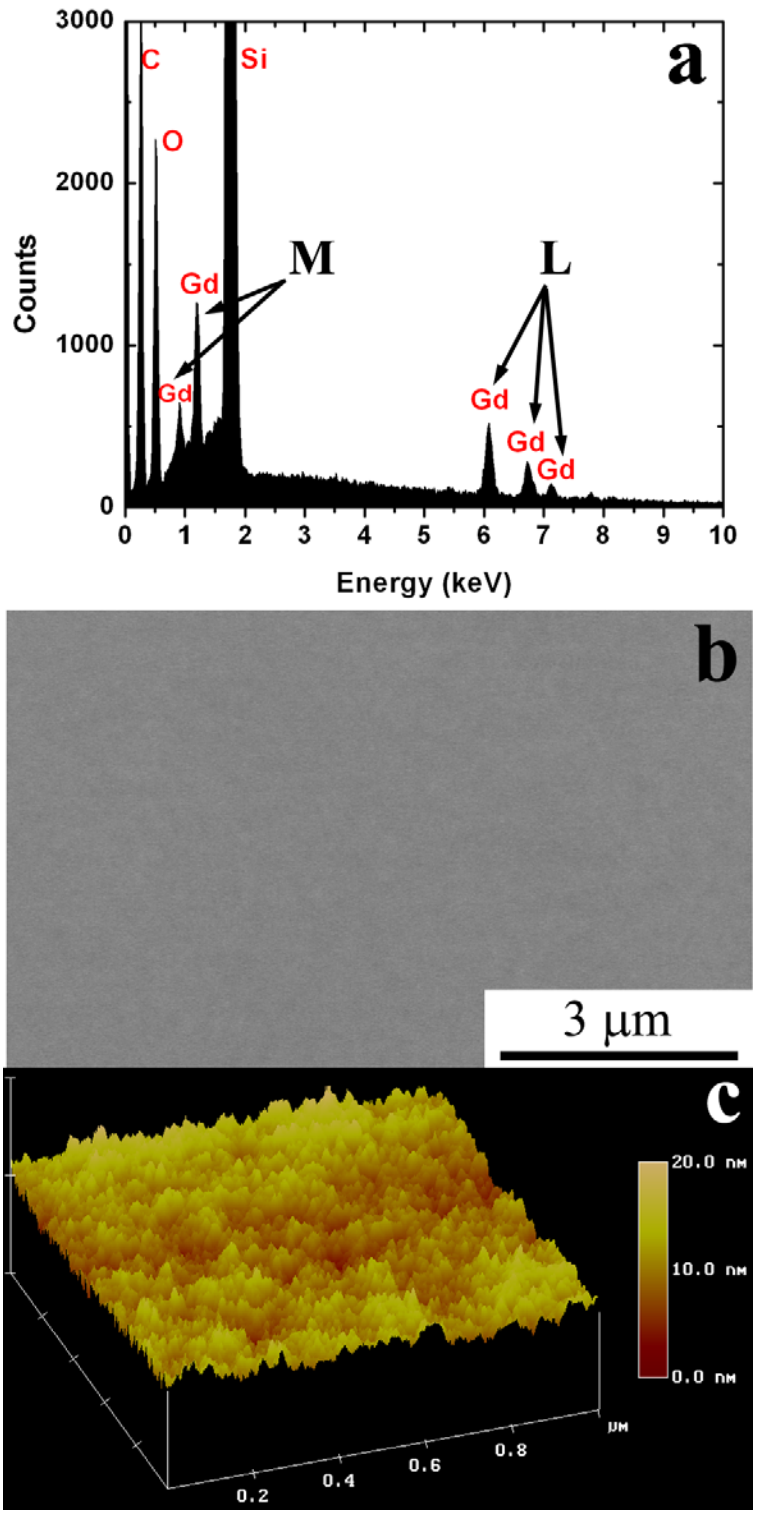

Figure 5.2: (a) EDS graph of the electrode shows the peaks of gadolinium, oxygen, carbon, and silicon, which confirms the deposition of oleic acid functionalized Gd_2O_3 nanocrystals. (b) SEM image of the nanocrystal film. (c) AFM image of the nanocrystal film, which reveals the deposition of agglomerates ($\sim$ 10-15 nm) of the Gd_2O_3 nanocrystals.

5.3.2 Electrical characterization of MOS capacitor

High-frequency *C-V* analysis is an excellent technique to probe dielectric properties of an insulator. Briefly, the fundamentals of *C-V* analysis of a MOS capacitor are reviewed here. In an ideal MOS structure, the metal and the semiconductor form two plates of a parallel-plate capacitor. At thermal equilibrium, the capacitor is charged to a voltage equivalent of the difference between the metal and the semiconductor work functions. The amount of charge stored on the capacitor is changed when a bias voltage is applied between the metal and the semiconductor. The applied voltage compensates the difference between the metal and the semiconductor work functions at a particular value. At this applied voltage, the charge stored on the capacitor is zero and the energy bands in the semiconductor are flat. Since this applied voltage produces flat energy bands in the semiconductor, this voltage is called *flat-band* voltage (V_{FB}). The *flat-band* voltage varies with the metal used and the doping density in the semiconductor. The *flat-band* voltage of an ideal MOS capacitor is defined as ideal *flat-band* voltage (${V_{FB}}^{Ideal}$).

In reality, there are different types of charges that are present in oxide-semiconductor system unlike in an ideal system. The presence of these charges shifts the experimental *C-V* curve with respect to the ideal *C-V* curve along the voltage axis. The ideal and the experimental *C-V* curves of the MOS capacitor are compared at the *flat-band* capacitance (C_{FB}). The capacitance at the *flat-band* voltage is known as the the *flat-band* capacitance. The *flat-band* capacitance of a MOS capacitor is given by equation 5.1, where C_{FB} is the capacitance at the *flat-band* voltage, C_{OX} is the oxide capacitance in the accumulation region, κ_s is the dielectric constant of the semiconductor, ϵ_o is the permittivity of vacuum, and L_D is Debye length.

$$C_{FB} = C_{OX}\left[\frac{\kappa_s\,\epsilon_o}{L_D\,(1+(\kappa_s\,\epsilon_o/L_D C_{OX}))}\right] \tag{5.1}$$

Debye length is given by equation 5.2, where k is Boltzmann's constant, T is the tempera-

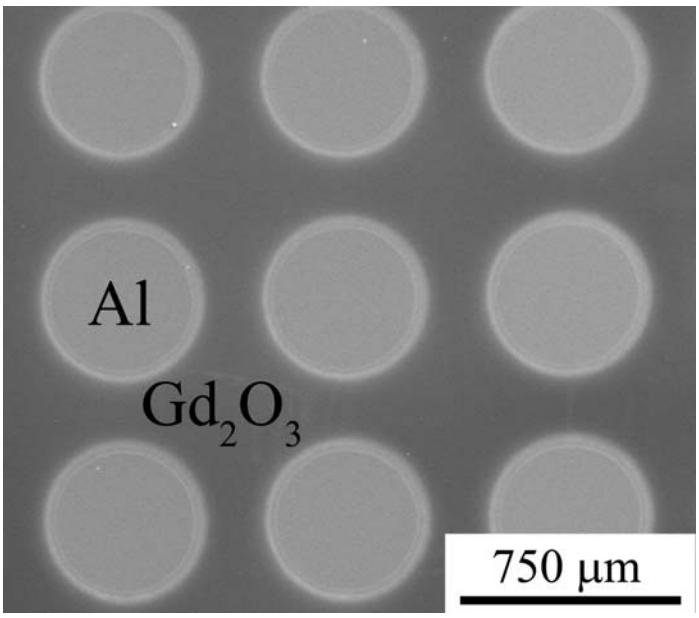

Figure 5.3: SEM image (Top view) of the MOS capacitor structure, exhibiting the Gd_2O_3 nanocrystal film and aluminum contacts.

ture, q is the electronic charge, and N_S is the doping concentration in semiconductor.

$$L_D = \sqrt{\frac{kT\kappa_s\epsilon_o}{q^2 N_S}} \tag{5.2}$$

Thus, the *flat-band* capacitance is calculated based on the oxide capacitance in accumulation (C_{OX}). This C_{FB} value is used to determine V_{FB}.

We performed *C-V* measurements on the MOS capacitors, fabricated with the Gd_2O_3 nanocrystal film as the gate oxide layer [Figure 5.3 (Top view)]. The *C-V* characteristics were recorded by sweeping the gate voltage from -10 V (accumulation) to +5 V (inversion) and back to -10 V (accumulation). The capacitance did not change much beyond this voltage range. The capacitors were biased at -10 V for 15 min prior to the forward sweep [-10 V $\rightarrow$ +5 V] and were biased at +5 V for 1 min prior to the reverse sweep [+5 V $\rightarrow$ -10 V] for their complete charging and discharging. Figure 5.4 shows the *C-V* characteristics of capacitors fabricated from the 116 $\pm$ 10 nm thick nanocrystal films, deposited on the anode and cathode. The *C-V* characteristics were similar to that of a typical MOS capacitor with distinct accumulation, depletion, and inversion regions. The MOS capacitors exhibited a

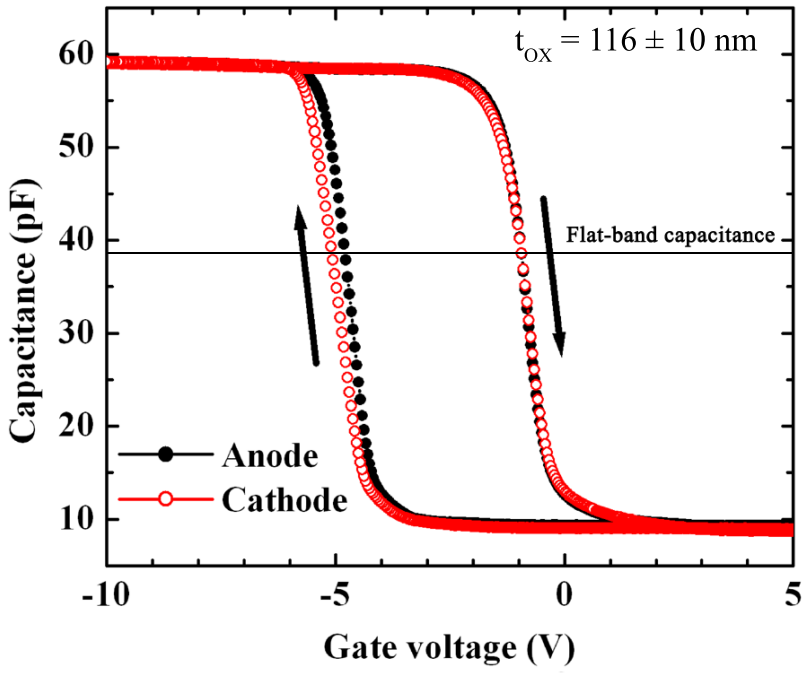

Figure 5.4: *C-V* characteristics of the MOS capacitors, fabricated from NC films that were deposited on the anode and cathode. The thickness of the film was 116 nm ± 10 nm, and the average area of the capacitors was 1.96×10^5 μm^2.

clockwise hysteresis in their *C-V* characteristics as they were biased through the accumulation → inversion → accumulation regions. A clockwise hysteresis was observed in the *C-V* characteristics even when the capacitors were biased through the inversion → accumulation → inversion regions. The observed hysteresis in the *C-V* characteristics indicated the presence of charge carriers within the nanocrystal film. The charge carriers could be immobile charges, arising from the unpassivated surface sites (Gd^{3+} and O^{2-}) of the nanocrystals, or mobile charges (electrons or holes), injected into the nanocrystal film. The presence of positive charges shifts the flat-band voltage (V_{FB}) of a MOS capacitor in negative direction compared to the ideal flat-band voltage, while the presence of negative charges shifts it in positive direction. The ideal flat-band voltage ($V_{FB}{}^{ideal}$) of our MOS architecture was -0.88 V, which was based on the work functions of Al and Si and the doping concentration in the epitaxial layer, and assuming no charges in the nanocrystal film. A larger negative shift in V_{FB} ($\Delta V_{FB} \sim$ - 3.92 V, anode) during reverse sweep (inversion → accumulation)

than the positive shift in V_{FB} ($\Delta V_{FB} \sim 0.05$ V, anode) during forward sweep (accumulation $\rightarrow$ inversion) suggested the presence of more positive charges in the nanocrystal film. Electrons were injected into the nanocrystal film from the gate electrode in the accumulation region, while electrons were subsequently extracted (equivalent to injection of holes) from the nanocrystal film into the gate electrode in the inversion region. We explored the charge-storage in the nanocrystal films deposited on the anode and cathode by comparing the width of the hysteresis window (ΔV) for the two nanocrystal films [3.97 V (anode) and 4.19 V (cathode)]. These values were found to be within the statistical uncertainty ($\pm$ 0.13 V) when multiple MOS capacitors were tested. The observed charge-storage in our Gd_2O_3 nanocrystal films was consistent with the other metal,[116] semiconductor,[118,119] and insulator[114] nanocrystal-embedded MOS capacitor structures.

Figure 5.5 shows *C-V* characteristics of the MOS capacitors, fabricated with the Gd_2O_3 nanocrystal films (oxide layer) of different thicknesses. The film capacitance, C_{film}, in the accumulation region decreased with increased nanocrystal film thickness, as was expected. For a given gate insulator material, the insulator capacitance (in accumulation) has a linear relationship with the inverse of the gate insulator thickness, as stated in equation 5.3.

$$C_{insulator} = \frac{A \times \epsilon_{insulator}}{t_{insulator}} \tag{5.3}$$

In this expression, $C_{insulator}$ is the insulator capacitance (F), A is the gate area (cm^2), $t_{insulator}$ is the insulator thickness (cm), and $\epsilon_{insulator}$ is the permittivity of the insulator material (F/cm). The Gd_2O_3 nanocrystal film is the gate insulator material in the present MOS architecture. Since the nanocrystal film comprised three constituents (Gd_2O_3, oleic acid, and air), its permittivity dependent on the volumetric fractions of those constituents. Since the volumetric fractions of the constituents within the film were not known, the permittivity of the nanocrystal film had to be determined experimentally. The permittivity of the Gd_2O_3 nanocrystal film was determined using the thickness and capacitance of the nanocrystal film. It was essential to determine the permittivity of the nanocrystal film

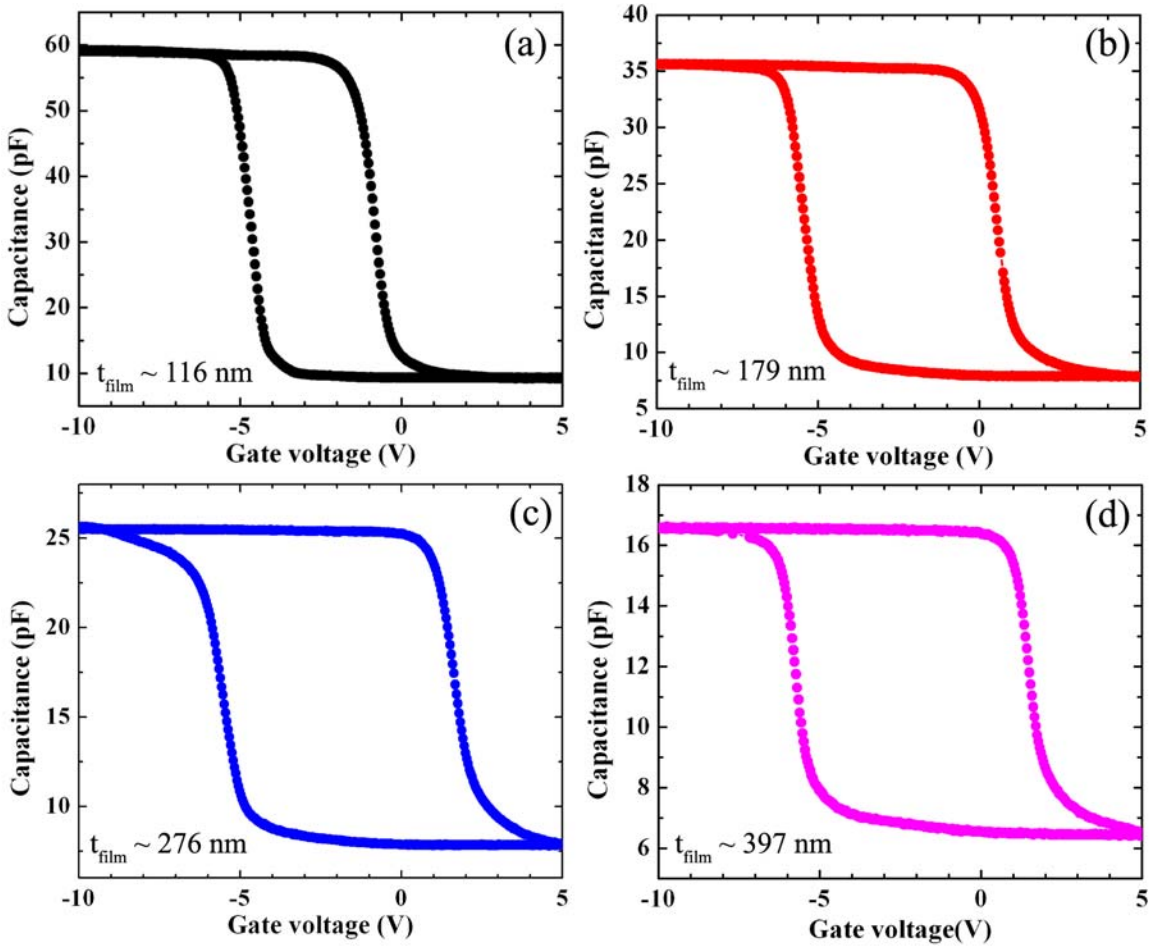

Figure 5.5: *C-V* characteristics of the MOS capacitors with different thicknesses of the nanocrystal films (oxide layer).

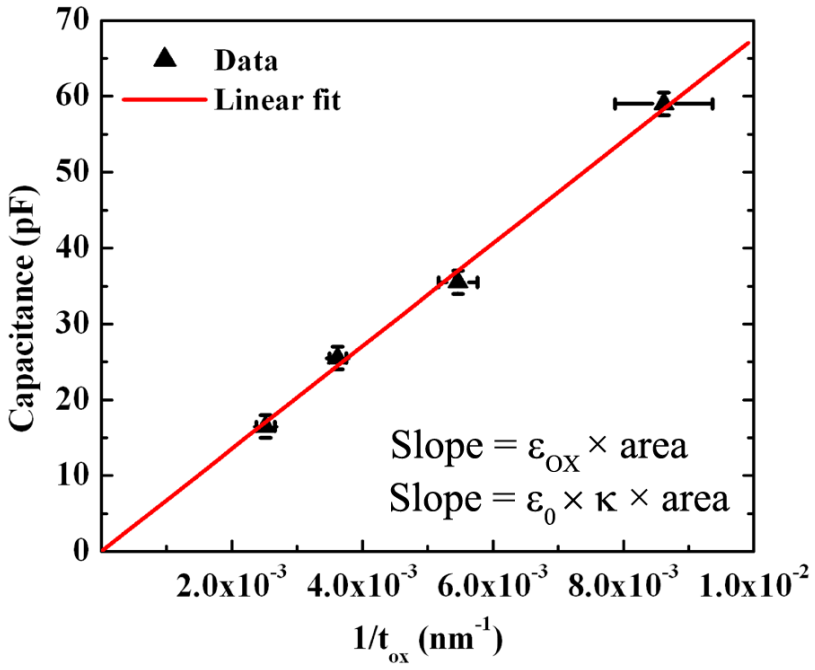

Figure 5.6: Graph of the film capacitance versus inverse of the nanocrystal film thickness for four different MOS capacitors. The slope of the linear regression fit was proportional to the permittivity of the nanocrystal film and, hence, to the film's dielectric constant, $\kappa = 3.90$.

because the permittivity of an insulator film is an important dielectric property. Figure 5.6 shows a graph of the film capacitance as a function of the inverse of the nanocrystal film thickness for MOS capacitors with different nanocrystal film thicknesses. The data exhibited good agreement with the linear trend. The dielectric permittivity of the nanocrystal film was extracted from slope of the linear fit, given the area of the gate. The dielectric constant,κ, of the Gd_2O_3 nanocrystal film was calculated using the relation, $\kappa = \epsilon_{insulator}/\epsilon_0$ and was found to be 3.90 ± 0.06. The dielectric constant of the nanocrystal film is the effective dielectric constant because films are composed of Gd_2O_3 nanocrystal core, oleic acid as surface capping ligand, and interstitial air.

5.3.3 Packing fractions of nanocrystal film

Since the nanocrystal film comprised Gd_2O_3 (κ= 14.0), oleic acid ($\kappa = 2.5$), and air ($\kappa = 1.0$), the effective dielectric constant of the nanocrystal film depended on the volumetric

fractions of each component in the film. Thus, packing fractions of nanocrystal films can be calculated based on the known effective dielectric constant of film and of the constituents. We observed good agreement between the data and the liner fit (Figure 5.6), which suggested that all of the nanocrystal films possessed comparable nanocrystal packing fractions even though they were assembled from solutions with different nanocrystal concentrations. We calculated the volumetric packing fractions of the nanocrystal film using a three-component Bruggeman model for the dielectric constant (Equations 5.4 and 5.5).

$$f_{air}\left[\frac{\kappa_{air}-\kappa_{film}}{\kappa_{air}+2\kappa_{film}}\right]+f_{OA}\left[\frac{\kappa_{OA}-\kappa_{film}}{\kappa_{OA}+2\kappa_{film}}\right]+f_{Gd_2O_3}\left[\frac{\kappa_{Gd_2O_3}-\kappa_{film}}{\kappa_{Gd_2O_3}+2\kappa_{film}}\right]=0 \qquad (5.4)$$

$$f_{air}+f_{OA}+f_{Gd_2O_3}=1 \qquad (5.5)$$

In the expression, volume fractions of air, nanocrystal film, oleic acid, and Gd_2O_3 are given as the f_{air}, f_{film}, f_{OA}, and $f_{Gd_2O_3}$, respectively. Dielectric constants of air, nanocrystal film, and Gd_2O_3 are given as the κ_{air}, κ_{film}, κ_{OA}, and $\kappa_{Gd_2O_3}$, respectively. Based on the coverage of oleic acid on the surface of a spherical nanocrystal core, we formulated a relationship between the volumetric fractions of the oleic acid surfactant and the Gd_2O_3 nanocrystal core as stated in equation 5.6, where R_1 is radius of the Gd_2O_3 nanocrystal core ($R_1 = 1.2 \pm 0.1$ nm), and R_2 is the radius of nanocrystal core (R_1) plus thickness of the oleic acid layer, t_{OA} ($t_{OA} = 0.3 \pm 0.1$ nm).

$$f_{OA}=f_{Gd_2O_3}\left[\left(\frac{R_2}{R_1}\right)^3-1\right] \qquad (5.6)$$

Volumetric fractions, $f_{air} = 0.34 \pm 0.08$, $f_{OA} = 0.32 \pm 0.10$, and $f_{Gd_2O_3} = 0.34 \pm 0.02$ were calculated from equations 5.4-5.6. The summed packing fraction for the nanocrystals (Gd_2O_3 nanocrystal core plus oleic acid) is 0.66 ± 0.08 and resides within the glassy packing regime for closely packed spheres.[122] Thus, EPD can produce densely packed, glassy films of ultra-small Gd_2O_3 nanocrystals that exhibit potential charge-storage capabilities.

5.4 Summary

The dielectric properties of the colloidal Gd_2O_3 nanocrystal films were probed with C-V analyses. MOS capacitor structures with colloidal Gd_2O_3 nanocrystal film as oxide layer were produced. Electrophoretic deposition produced uniformly deposited films of the cleaned Gd_2O_3 nanocrystals. A hysteresis in C-V curves of the MOS capacitors suggested charge-storage within the nanocrystal films. The nanocrystal films, deposited on the anode and cathode, had similar charge-storage properties. MOS capacitor structures with different nanocrystal film thicknesses exhibited charge-storage characteristics. Effective dielectric constant ($\kappa = 3.90$) of the nanocrystal films was calculated from the C-V measurements of the MOS capacitors. Packing density of the nanocrystals within the film (0.66 ± 0.08) was calculated from the effective dielectric constant of the nanocrystal film and was found to be within glassy-packing regime, as expected for the films deposited via electrophoretic deposition.

CHAPTER VI

NANOCRYSTAL-CARBON NANOTUBE HETEROSTRUCTURES: DEVELOPMENT & CHARACTERIZATION

6.1 Introduction

Since the widespread recognition of carbon nanotubes (CNTs) and nanocrystals (NCs) in the early 1990s, interest in basic and applied research of these materials has grown exponentially. Carbon nanotubes have attractive electronic properties, superior tensile strength, and low density.[123–125] Similarly, metallic, semiconducting, and insulating NCs have been investigated for their unique size-dependent optical, magnetic and catalytic properties.[41,126,127] The research area of CNT-NC composites, which investigates the integration of CNTs and NCs into single materials for various device architectures, has garnered much attention for potential applications in next-generation luminescent, magnetic, and energy-storage devices.[64,128–136] This area comprises three major trajectories: the functionalization of the surface of the CNT surface with NCs; the co-deposition CNTs and NCs into thin films; and the alternating, multilayered deposition of CNTs and NCs. Of these areas, the NC-functionalized CNTs trajectory has received most attention.[132] Metallic NCs of Pt, Ru, Ag, Au, and Pd have successfully been functionalized onto CNTs for their catalytic properties for use in fuel cell devices.[135,136] Electrically-addressable, iron and iron oxide-infused CNTs have been explored for their application in gas sensors and memory devices.[129] The functionalization of TiO_2 and Pt NCs onto CNTs also has been accomplished through electrodeposition.[133,134] The second trajectory focuses on the production of NC-CNT composites using co-deposition and co-densification of NCs and CNTs into thin film composites for biocompatible materials applications.[64,128] The third research trajectory involves alternate deposition of CNTs and NCs to create multilayered architectures, which

are integral to several existing and proposed optical and energy-storage devices. The idea of employing nanocrystals and CNTs in alternating layer architectures is very recent. The fabrication of the layered structures of CNT and SiO_2/TiO_2 nanocrystals have been reported for their potential use in tissue engineering and biomedical implants applications.[78,137] In these layered structures, interfaces between the NC-CNT layers were not sharp, which is essential in various applications.

A layered architecture is an integral design of optical and electrochemical energy-storage devices. In electrochemical energy-storage devices such as supercapacitors, Li-ion batteries, and fuel cells, charges are stored on active electrodes that are isolated by a charge separator. Conducting material is required for the active electrodes, and an electrical insulator is needed as a separating layer.[131] CNTs are known for their conductive properties and have been investigated as a material for electrodes in fuel cells and supercapacitors.[131,133,135] Apart from the light emissive properties, Eu_2O_3 is known for its dielectric properties.[138,139] Eu_2O_3 has been proposed as a promising candidate material for high-κ gate dielectrics for transistors ($\kappa \sim 12$).[138,139] These properties of CNTs and Eu_2O_3 motivated our investigation on integrating CNTs and Eu_2O_3 nanocrystals into a layered architecture. Implementation of Eu_2O_3 nanocrystal film as a separator between CNT layers is a possible architecture for energy-storage device applications. A separator layer is typically thicker than 10 μm. The separator layer thickness can be reduced if a high-κ dielectric material, such as Eu_2O_3, is used. Use of thinner separator layers would facilitate increased charge-storage per unit volume. It is important to achieve good electrical insulation between the electrodes when reducing the separator layer thickness. For the proposed prototype, production of a high quality layered structure of CNTs and NCs is required.

In this chapter, we describe the successful production of layered *CNT mat-Eu_2O_3 NC film-CNT mat* heterostructure using the alternating *low field - high current* and *high field - low current* EPD technique. Homogeneous CNT mats were deposited from an aqueous CNT suspension, while uniform Eu_2O_3 nanocrystal films were produced from nanocrystal

suspension in hexane. Capacitance-voltage characteristics of the heterostructure are discussed. To explore the versatility of this fabrication technique, nanocrystals of different type and size ($\sim$ 20 nm dia. Fe_3O_4 vs $\sim$ 2.4 nm dia. Eu_2O_3) were employed to produce the *CNT mat-NC film-CNT mat* heterostructures. The surface morphology, coverage, and roughness of this heterostructure were analyzed.

The research described in this chapter has been published in the following journal articles:

- S. V. Mahajan, S. A. Hasan, J. Cho, M. S. P. Shaffer, A. R. Boccaccini and J. H. Dickerson, Carbon nanotube-nanocrystal heterostructures fabricated by electrophoretic deposition, *Nanotechnology*, **19** 195301, (2008)

- S. V. Mahajan, J. Cho, M. S. P. Shaffer, A. R. Boccaccini and J. H. Dickerson, Electrophoretic deposition and characterization of Eu_2O_3 nanocrystal-carbon nanotube heterostructures, *J. Eur. Ceram. Soc.*, **30** 1145, (2010)

6.2 Experimental details

6.2.1 Materials

A chemical vapor deposition (CVD) technique was employed to grow multi-walled CNTs of approximately 50 nm diameter, as reported elsewhere.[140] Briefly, a ferrocene-toluene mixture was injected into a quartz tube furnace, which was filled with a hydrogen:argon (1:9) gas mixture and was maintained at 760 °C. Arrays of aligned CNTs formed on the inside surface of the quartz tube. Upon removal of the CNTs from the quartz tube's surface, the CNTs were purified with an acid-treatment.[81,140] The purification process involved refluxing 1 g of as-grown CNTs in a mixture of nitric acid (100% grade, 10 ml) and sulfuric acid (100% grade, 30 ml) at 120 °C for 30 min. Next, the CNTs were washed with DI water until the suspension showed no changes in acidity. The aqueous CNT suspension

was sonicated for a few hours and centrifuged at 3500 rpm for 15 min. The CNTs, employed in this research, were provided by our research collaborator, Prof. Milo S. P. Shaffer.

The $\sim$ 2.4 nm diameter Eu_2O_3 nanocrystals ($\sim$ 2.4 nm dia.), capped with oleic acid, were synthesized as per the technique reported in Chapter II [Section 2.2.1 & 2.2.2]. Since the synthesis reaction that produced $\sim$ 3.0 nm diameter nanocrystals had low yield (< 30 %), we selected $\sim$ 2.4 nm diameter Eu_2O_3 nanocrystals between the two remaining nanocrystal sizes as a test case. A typical precipitation-centrifugation procedure, described in Chapter II [Section 2.2.3], was employed to clean the nanocrystals with ethanol. The 10×-cleaned Eu_2O_3 nanocrystals were suspended in hexane for EPD because these nanocrystals produced homogeneous films.

The iron oxide (Fe_3O_4) nanocrystals were synthesized via a hot solution-phase technique, as described elsewhere.[42] Briefly, the iron-oleate complex was prepared when iron chloride hexahydrate (2 mM) reacted with sodium oleate (6 mM) in a water-ethanol-hexane mixture at 70°C for four hours. This Fe-oleate complex was washed with DI water, before being mixed with 0.5 mM of oleic acid in 10 ml of tri-*n*-octylamine and refluxed at 320 °C for 30 minutes. The nanocrystals nucleated and grew to approximately 20 nm diameter during this stage. The nanocrystals were precipitated by addition of 10 ml ethanol to the 1 ml reaction mixture and were isolated by centrifugation at 3500 rpm for 15 minutes. In some trials, this precipitation process was repeated after redispersion in fresh hexane. These nanocrystals were easily dispersed in hexane for deposition by EPD.

6.2.2 Heterostructure development

To develop layered carbon nanotube-nanocrystal heterostructures, an alternating sequence of EPD of CNTs and NCs was employed. First, a CNT mat was deposited on the steel electrode. Next, the CNT mat was used as an anode during the deposition of NCs. Subsequently, the NC-deposited CNT mat was employed as the anode for the deposition of the second CNT mat. Thus, *CNT mat-NC film-CNT mat* heterostructures were

Table 6.1: EPD parameters for carbon nanotubes (CNTs) and nanocrystals (NCs).

Material	Suspension	Electrode gap (mm)	Voltage (V)	Deposition time (min)	Drying time (min)
CNTs	Water	10	20	10	15
Eu_2O_3 NCs	Hexane	2	1000	15	5
Fe_3O_4 NCs	Hexane	2	1000	30	5

fabricated using this sequence. Typically, metallic substrates are employed to fabricate electrochemical energy-storage devices. We selected stainless steel as the substrate to produce heterostuctures because of its low cost and anti-corrosive property. Anti-corrosive property of the substrate is important during EPD of CNTs. Since suspension of CNTs in water was slightly acidic, it attacked the ITO and gold electrodes degrading uniformity of the film. The deposition of CNTs and NCs is described below and the EPD parameters are listed in Table 6.1.

EPD of CNTs

An electrode assembly of the stainless steel electrodes was used for the deposition of CNTs [Section 3.3.2]. Well-stabilized suspension of functionalized CNTs was prepared in water. A BK Precision 1787B power supply was used to apply a constant dc voltage of 20 V across a 10 mm wide electrode gap. The EPD was performed for 10 minutes, and a current density of approximately 4 mA/cm^2 was measured throughout the EPD experiment. The electrodes then were air-dried for 15 minutes, while maintaining the applied voltage, to remove any residual water and for densification. The EPD parameters employed for this deposition are listed in Table 6.1. For the EPD of CNTs, the flow of current through the suspension comprises an electrolytic current due to water and free ions, and an electrophoretic current due to the CNTs. The CNT suspension conducts a large current even at low electric fields due to the large contribution of electrolytic current from water. The use of higher electric fields produces inhomogeneous CNT films due to the dissociation of water and the evolution of gases at the deposition electrodes.[141] Therefore, the operating

voltage was chosen such that electrolysis of water was minimized and homogeneous CNT films were deposited. The deposition of homogeneous CNT mats was classified into *low field - high current* regime based on the electric field and current flowing through the EPD suspension.

EPD of NCs

The CNT mat was used as an anode to deposit nanocrystals onto the mat. Well-dispersed suspensions of NCs were prepared in hexane. A Keithley 6517A Electrometer was used to apply a dc voltage and to measure the current flowing through the suspension. A NC film deposition consisted of the application of a constant 1000 V across a 2 mm electrode gap for a duration of 15 minutes. Typically, a peak current density of approximately 1 μA/cm^2 was measured during the deposition. After the deposition, the NC film was air-dried for five minutes while maintaining the applied voltage to remove residual hexane and for densification. During EPD of NCs, the NC suspension conducts small current even at high electric fields due to a negligible contribution of electrolytic current from hexane (Pure hexane: $\sim$ 0.3 nA/cm^2). Therefore, the deposition of uniform NC films was classified into the *high field - low current* regime based on the applied electric field and current flowing through the EPD suspension.

6.2.3 Characterization techniques

The dimensions of the CNTs were measured from the images of the CNT mat captured using SEM. The sizes of the Eu_2O_3 and Fe_3O_4 nanocrystals were measured from TEM images of the nanocrystals. The corresponding hydrodynamic diameter of Fe_3O_4 nanocrystals, suspended in hexane, was determined from a DLS measurement. The nanocrystal suspension was stabilized in the dark overnight prior to the DLS measurement. Surface morphologies of the CNT mats and nanocrystal films were characterized using SEM. High resolution surface morphologies of the films were analyzed using AFM. Elemental analyses of the EPD films were completed with X-ray EDS. Photoluminescence measurements of the

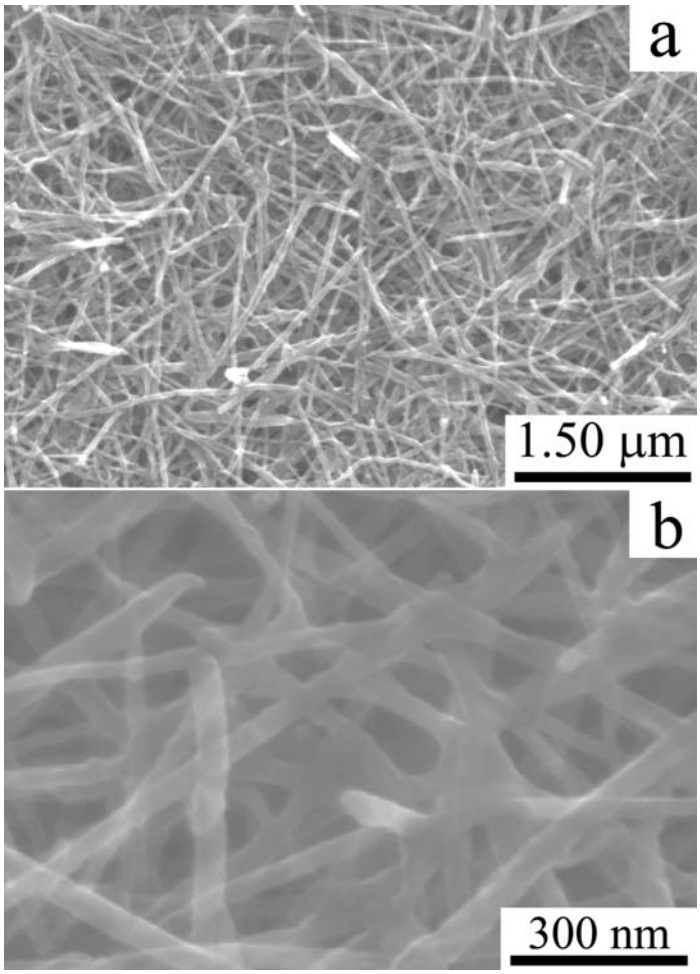

Figure 6.1: Low magnification (a) and high magnification (b) SEM images of the EPD films of the purified CNTs. The length of the CNTs varied between 1 - 2 μm and the average diameter of the CNTs was 50 nm.

CNT mats and Eu_2O_3 nanocrystal films were conducted. Capacitance-voltage measurements were performed at a frequency of 1 MHz and at a sweep rate of 50 mV/s.

6.3 Results and discussion

6.3.1 Materials characterization

Figure 6.1 shows the SEM images of the EPD film of the purified CNTs atop the steel substrate. The length of the purified CNTs varied between 1 and 2 μm, as seen in figure 6.1(a). The acid-treatment process, performed to purify the CNTs, has the secondary

effect of shortening the CNTs.[140,142] The high magnification SEM image of the CNT mat [Figure 6.1(b)] confirms the average diameter of $\sim$ 50 nm of the purified CNTs. Figure 6.2(a) shows a TEM image of the Eu_2O_3 nanocrystals of average core diameter 2.4 nm. PL spectrum of the nanocrystals, shown in figure 6.2(b), exhibits the characteristic emission peaks of Eu_2O_3 nanocrystals [Figure 2.9(a)].[41] Figure 6.3(a) shows a TEM image of $\sim$ 20 nm diameter Fe_3O_4 nanocrystal. Figure 6.3(b) shows a DLS measurement of the hydrodynamic diameter of Fe_3O_4 nanocrystals in hexane. The hydrodynamic diameter of the nanocrystals in suspension includes the diameter of the core nanocrystal and twice the thickness of surface capping ligand layer (oleic acid). Based on Gaussian curve fit, the average hydrodynamic diameter of the nanocrystals was 23.7 $\pm$ 6.5 nm. Given the approximately 1.5 nm thickness of the oleic acid ligand layer at the surface,[59] there was good agreement between the DLS result and the TEM image.

6.3.2 CNT mat-Eu_2O_3 NC film-CNT mat heterostructure

The CNT mats were deposited from well-dispersed, aqueous suspension of purified CNTs with EPD technique on steel substrate as reported previously.[81] The negative charges on CNT surfaces were induced during the purification process as a consequence of the functionalization of the CNT surfaces with negatively charged, oxygen-containing acidic groups. Hence, purified CNTs deposited only on the anode to produce a CNT mat. These negatively charged surface groups were also responsible for producing well-stabilized CNT suspension in water. Since the CNT mat was employed as an electrode to deposit the nanocrystals, surface morphology, elemental composition, and luminescent characteristics of the bare CNT mat were investigated using scanning electron microscopy, energy dispersive spectroscopy, and photoluminescence spectroscopy prior to the nanocrystal deposition. Figure 6.4(a) shows the SEM image of a CNT mat deposited on the steel electrode, using the parameters stated in Table 6.1. The majority of the CNTs deposited flat in-plane with the electrode and were uniformly distributed within the mat. The CNTs within the mat

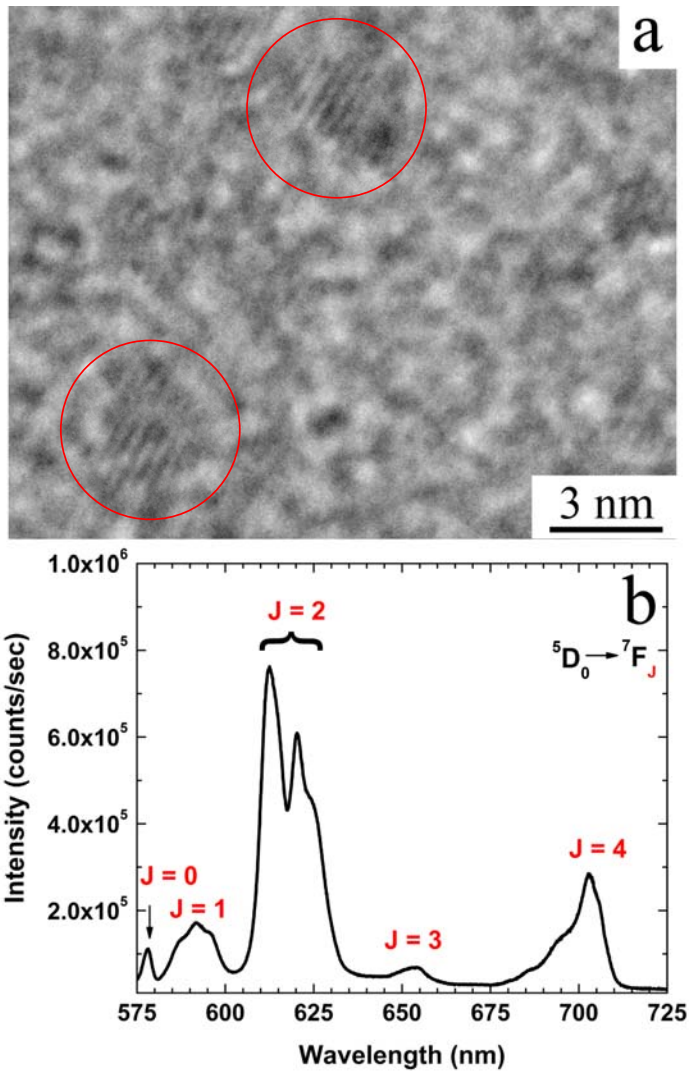

Figure 6.2: (a) TEM image of the Eu_2O_3 nanocrystals, which confirms the average 2.4 nm diameter nanocrystals; (b) PL spectrum of the Eu_2O_3 nanocrystals exhibiting characteristic red emission peaks.

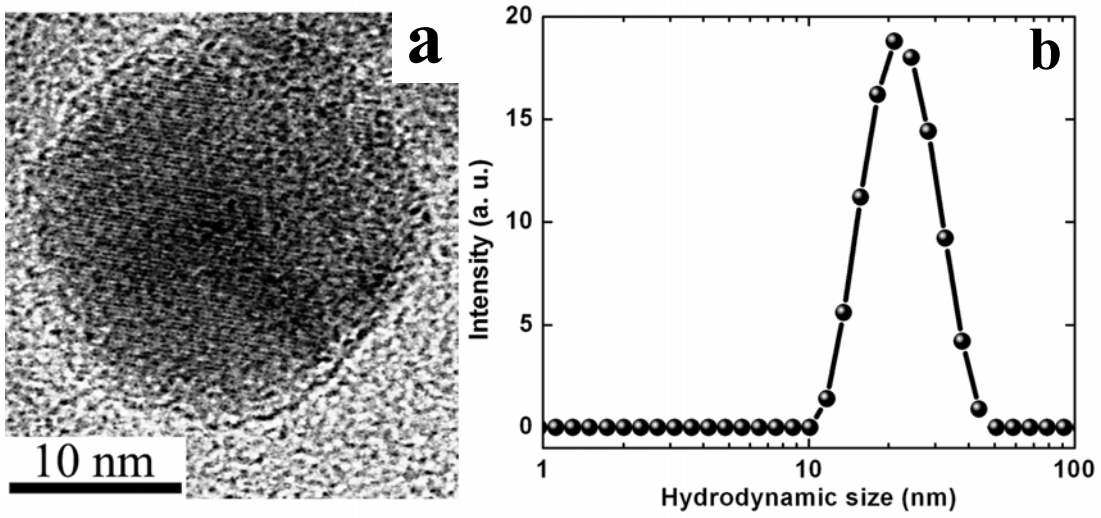

Figure 6.3: (a) TEM image of the Fe_3O_4 nanocrystal with $\sim$ 20 nm core diameter; (b) Dynamic light scattering graph of Fe_3O_4 nanocrystals, with an average hydrodynamic diameter of 23.7 $\pm$ 6.5 nm.

deposited with a random planar orientation producing a porous mat with approximate pore size of 100 nm. The EDS plot of the CNT mat, deposited on the stainless steel substrate, is shown in figure 6.4(b). Besides the presence of the strong peak of carbon, the oxygen peak was detected due to the presence of the oxygen-containing acidic groups on the surface of the purified CNTs, which was confirmed by the absence of these peaks in the EDS of bare steel substrate. The iron, molybdenum, chromium, and silicon peaks were attributed to the underlying stainless steel electrode. The photoluminescence spectrum of the bare CNT mat, prior to the Eu_2O_3 NC deposition, was collected upon UV excitation (254 nm) and is shown in figure 6.4(c). Since the characteristic emission peaks of the Eu_2O_3 nanocrystals are in the 575 - 725 nm spectral region of the visible spectrum, the emission characteristics of the bare CNT mat were measured within the same spectral region. The CNTs exhibited a weak emission peak near 650 nm.

The Eu_2O_3 nanocrystals were deposited on top of the CNT mat via the *high field-low current* EPD method employing the parameters stated in Table 6.1. The Eu_2O_3 nanocrystals, employed for the deposition, were well-dispersed in the non-polar medium, hexane. The

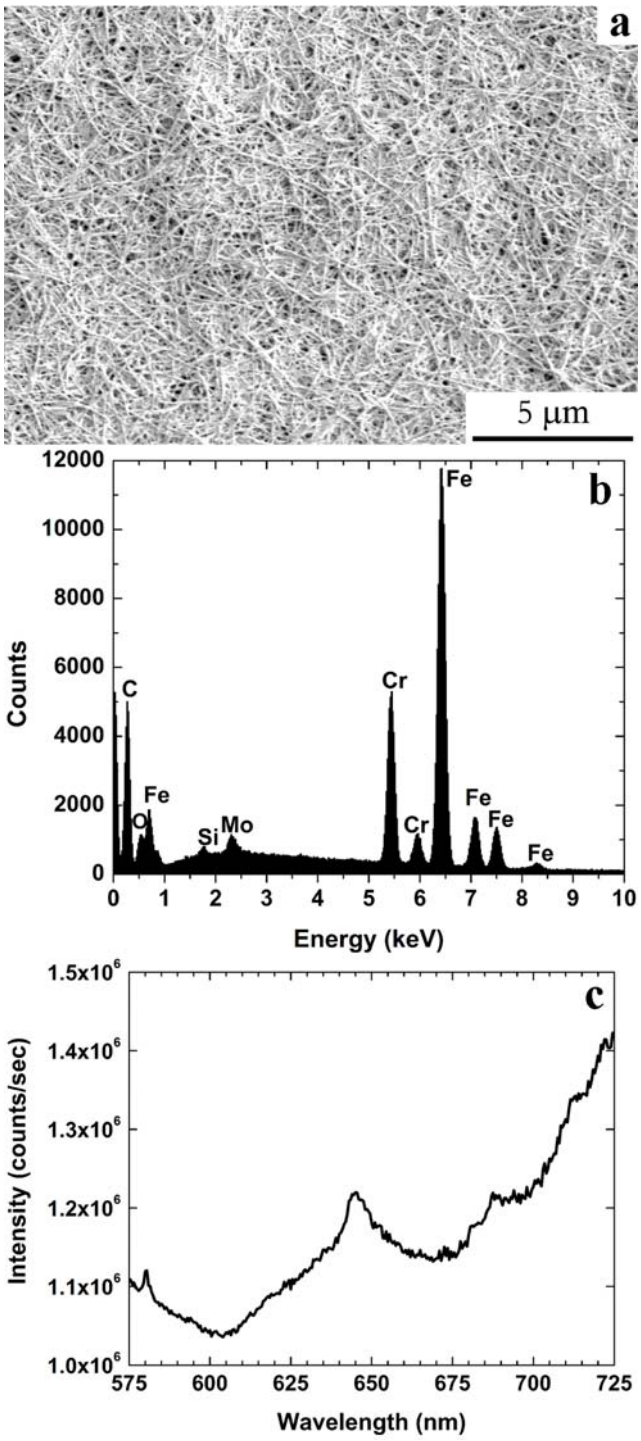

Figure 6.4: (a) SEM image of the CNT mat. The CNTs deposited with a random planar orientation producing a porous mat; (b) EDS graph of the CNT mat. The carbon and oxygen peaks were detected from the CNTs, which were functionalized with the oxygen-containing acidic groups; (c) PL spectrum of the CNT mat, which shows a small peak at $\sim$ 650 nm.

CNT mat-deposited stainless steel electrode was employed as the anode for EPD. Scanning electron microscopy, energy dispersive spectroscopy, and photoluminescence spectroscopy techniques confirmed the deposition of the Eu_2O_3 nanocrystals atop the CNT mat. Figure 6.5(a) shows the SEM image of the nanocrystal film. A uniform nanocrystal film is visible, which covered the porous CNT mat entirely. All the pores present on the surface of the CNT mat were filled by the nanocrystals, forming a continuous film. After the nanocrystal deposition, the morphology and contour of the underlying porous CNT mat was no longer visible. The energy dispersive spectrum, as seen in figure 6.5(b), confirmed the deposition of Eu_2O_3 nanocrystals. The X-ray emission peaks of europium, oxygen, and carbon were detected, as expected. The presence of these peaks was attributed to the deposition of oleic acid functionalized Eu_2O_3 nanocrystals. The PL spectrum of the anode, shown in figure 6.5(c), has the characteristic emission peaks of Eu_2O_3 nanocrystals, which verified the deposition of the nanocrystals. The spectral positions of the photoluminescence peaks of the film were identical to that of the Eu_2O_3 nanocrystals in suspension [Figure 6.2(b)]. This observation suggested that EPD did not change the luminescence characteristics of the nanocrystals. Thus, SEM images, EDS, and PL measurements confirmed the deposition of the homogeneous Eu_2O_3 nanocrystal film atop the CNT mat.

To produce the *CNT mat-Eu_2O_3 NC film-CNT mat* architecture, the NC-deposited CNT mat was employed as the anode to deposit a second CNT mat using the same electrode configuration and operating parameters as for the first CNT mat. Figure 6.6 shows the top view and side view SEM images of the heterostructure. The electrode with the heterostructure was cut in its center to obtain a clear cross-sectional view of said heterostructure. The morphology of the second CNT mat [Figure 6.6(a)] was similar to that of the first CNT mat [Figure 6.4(a)]. However, a significant difference in the thickness of the two mats was observed for the same EPD configuration and deposition parameters. The first CNT mat was approximately 2 μm thick, while the second mat was approximately 500 nm thick, as shown in figure 6.6(b). A part of the applied voltage dropped across the preexisting,

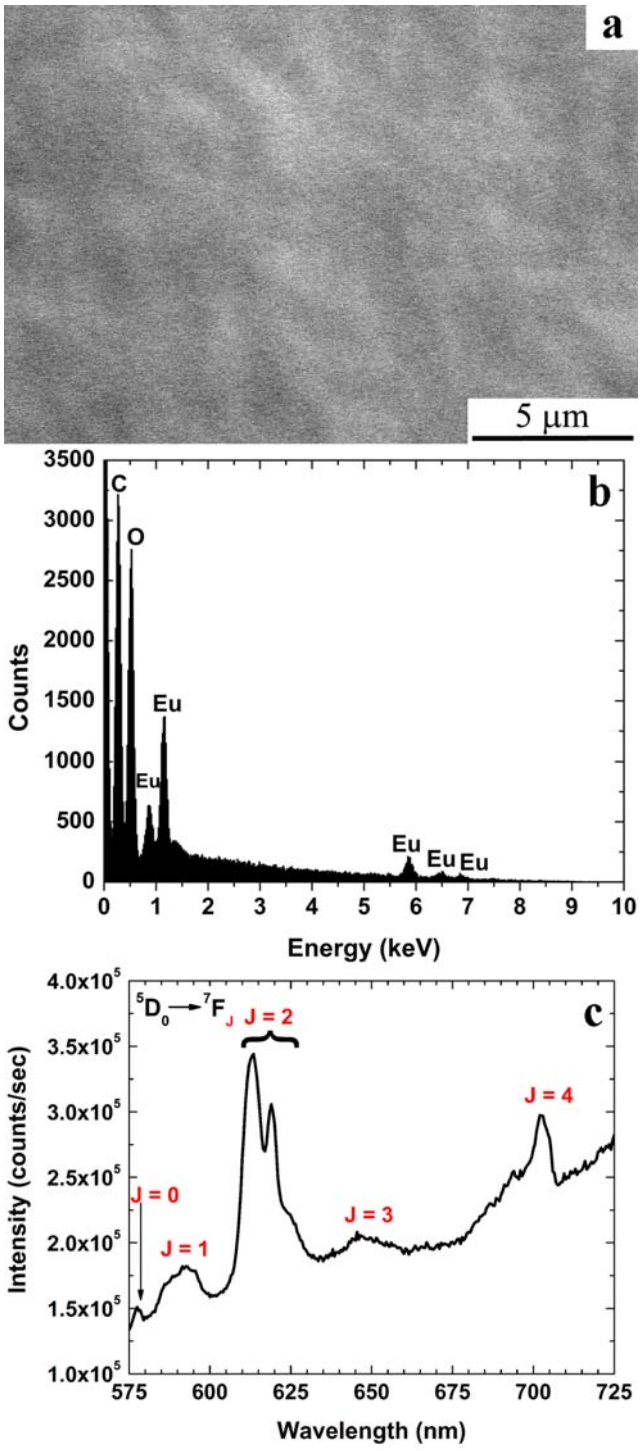

Figure 6.5: (a) SEM image of the nanocrystal film showing uniform and continuous deposition of the nanocrystals atop the CNT mat; (b) EDS graph of the nanocrystal film, which reveals the presence of the europium, oxygen, and carbon peaks; (c) PL spectrum of the Eu_2O_3 nanocrystal film, which exhibits characteristic emission peaks of the Eu_2O_3 nanocrystals.[41]

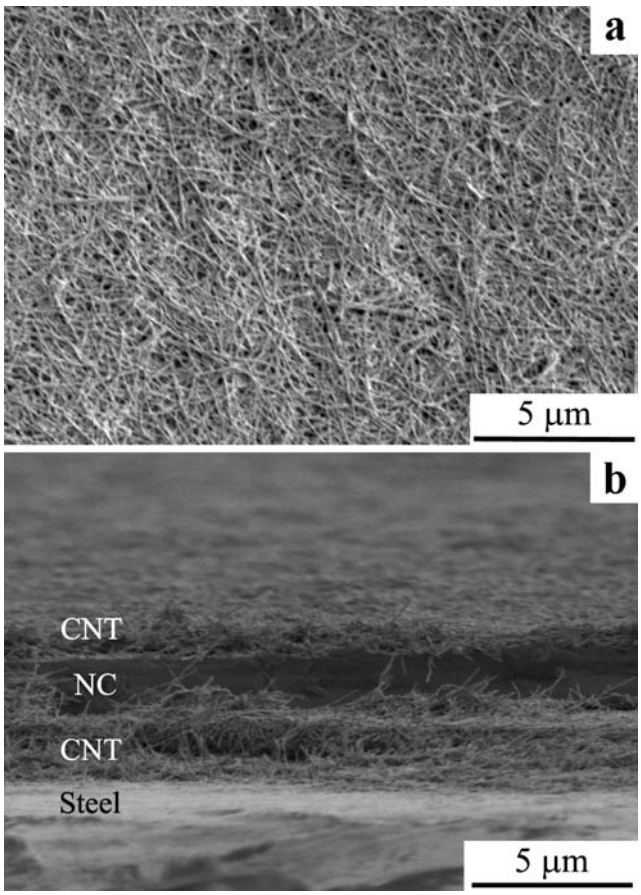

Figure 6.6: (a) Top view SEM image and (b) side view SEM image of the CNT mat-Eu_2O_3 NC film-CNT mat heterostructure.

low-conductivity CNT mat-Eu_2O_3 NC film architecture during the second CNT deposition. Hence, the effective voltage for EPD was reduced, leading to the thinner second CNT mat. To produce the first and second CNT mats of comparable thickness, the deposition time of the first CNT mat should be reduced or the deposition time of second CNT mat and the CNT concentration should be increased. Figure 6.6(b) shows the separating, Eu_2O_3 NC film between the two CNT mats, which was approximately 2 μm thick. The sharp interface between the NC film and the CNT mat is visible. The nanocrystals deposited only on the top surface of the CNT mat and did not penetrate deep inside the mat, forming a sharp interface. This outcome was in contrast to results on EPD of CNT/TiO_2 nanoparticle composites, where TiO_2 nanoparticles were seen to penetrate deep inside the porous CNT mat.[78] The non-dispersibility of CNTs in hexane prevented impregnation of the nanocrystal dispersion inside the mat, which facilitated a sharp interface formation. The impregnation of nanocrystals can not be adjusted by changing EPD process parameters. Thus, high quality *CNT mat-Eu_2O_3 NC film-CNT mat* heterostructures with sharp interfaces were reproducibly formed using the *low field - high current* and *high field - low current* EPD method.

The *CNT mat-Eu_2O_3 NC film-CNT mat* architecture mimics a metal-insulator-metal (MIM) capacitor structure.[143] Electrical characteristics of the heterostructure were probed using *CV* measurements. To perform *CV* measurements on the heterostructure, the probes were connected to the top CNT mat and the steel substrate. The heterostructure was biased from +5 V to -5 V to perform the *CV* measurement. Prior to the *CV* measurement, the heterostructure was biased at +5 V for 5 min to allow sufficient time for its charging. Five different measurements were performed by connecting the probe at five different locations on the top CNT mat. Figure 6.7 shows five representative *CV* curves of the heterostructure, which exhibit a relatively constant, consistent capacitance over the entire $\pm$ 5V voltage range. A constant capacitance over a voltage range is a typical characteristic of a MIM capacitor.[143] Thus, the *CNT mat-Eu_2O_3 NC film-CNT mat* heterostructure ex-

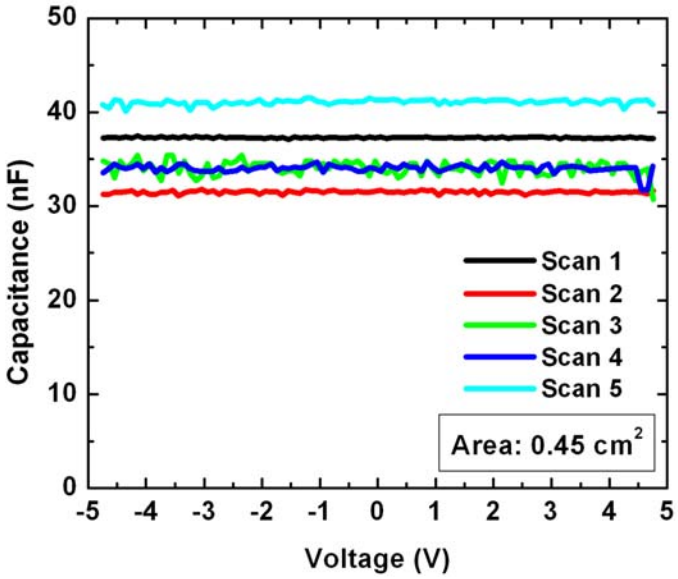

Figure 6.7: Capacitance-voltage (CV) characteristics of the CNT mat-Eu_2O_3 NC film-CNT mat heterostructure.

hibited CV response, which is characteristic of a MIM capacitor. An average capacitance of 35.4 $\pm$ 3.7 nF was measured for the heterostructure. Since the heterostructure exhibited characteristics of a MIM capacitor, it was confirmed that the two CNT mats were electrically insulated from one another. Also, such a *CV* response confirmed that charges were stored in the heterostructure. These results confirmed that a *CNT mat-Eu_2O_3 NC film-CNT mat* architecture could be employed potentially as a structure for an energy-storage device.

6.3.3 CNT mat-Fe_3O_4 NC film-CNT mat heterostructure

To explore versatility of the EPD technique, we produced CNT-NC heterostructure with different type and size of nanocrystals i.e. Fe_3O_4 nanocrystals of approximately $\sim$ 20 nm diameter. We followed the sequential EPD technique to fabricate *CNT mat-Fe_3O_4 NC film-CNT mat* heterostructure by employing the parameters as listed in Table 6.1. The surface morphologies of the CNT mat and Fe_3O_4 nanocrystal films were investigated using SEM and AFM. First, the CNT mat was produced on the steel substrate (anode). Figure

6.8(a) shows the SEM image of the CNT mat produced on the steel substrate. Majority of the CNTs were parallel to the substrate with a random planar orientation, producing the porous CNT mat. The AFM image of the CNT mat, shown in figure 6.8(b), gives a better sense of the depth profile of the mat. A few CNTs, oriented at an obtuse angle with respect to the electrode surface, are seen as bright spots in the AFM image. The ends of these tubes extend approximately 200 nm above the surface of the CNT mat. The RMS surface roughness of the CNT mat, determined from an analysis of the AFM image, was $\sim$ 34.6 nm.

Next, the EPD of Fe_3O_4 nanocrystals was performed with the CNT mat employed as an anode. Figure 6.8(c) shows the SEM image of the anode after the nanocrystal deposition was performed for 30 minutes. The nanocrystals were deposited directly on top of the CNTs as well as within the pores that were on the surface of CNT mat. A number of the pores, though, remained uncovered. The SEM and AFM images [Figure 6.8(c-d)] show that a small fraction of CNTs remained uncoated by the nanocrystals. The measured RMS surface roughness of the film was $\sim$ 31.9 nm, which was lower than the roughness of the CNT mat, as expected. Unlike the Eu_2O_3 nanocrystal film, the Fe_3O_4 nanocrystal film covered the CNT mat partially in a single deposition. In the earlier case, complete surface coverage was achieved during a single deposition of Eu_2O_3 nanocrystals, which was likely due to a small size of the nanocrystals. Smaller nanocrystals tend to have higher surface charge density due to larger surface-to-volume ratio, engendering higher electrophoretic mobility.[144] In the present case, the Fe_3O_4 nanocrystal film coverage was improved further with multiple depositions of the nanocrystals with an intermediate air-drying step. SEM and AFM images of twice-deposited nanocrystal films on a CNT mat are shown in figure 6.8(e-f), respectively. The SEM image shows that the porosity in the nanocrystal film is reduced. Also, we observed a notable improvement in the RMS surface roughness ($\sim$ 20.8 nm) of twice-deposited nanocrystal film over that for singly deposited nanocrystal film ($\sim$ 31.9 nm). We confirmed that multiple depositions improve the nanocrystal film

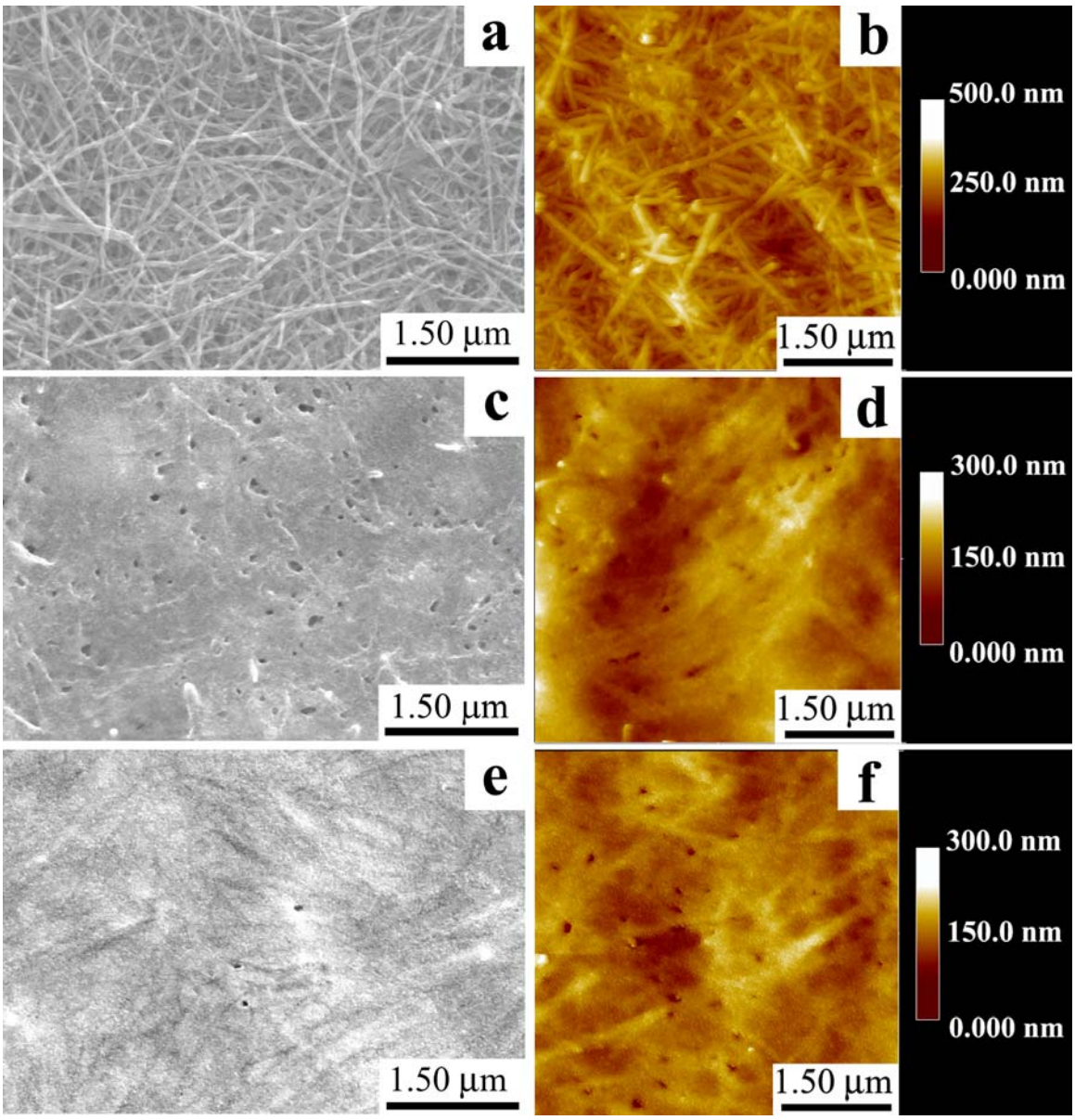

Figure 6.8: (a) SEM image and (b) AFM image of the CNT mat, fabricated on a steel substrate; (c) SEM image and (d) AFM image of the Fe_3O_4 nanocrystal film fabricated atop the CNT mat from a single deposition. The unfilled pores are evident in both images; (e) SEM image and (f) AFM image of the Fe_3O_4 nanocrystal film fabricated atop the CNT mat from a double deposition. The porosity in the nanocrystal film diminished after the second deposition.

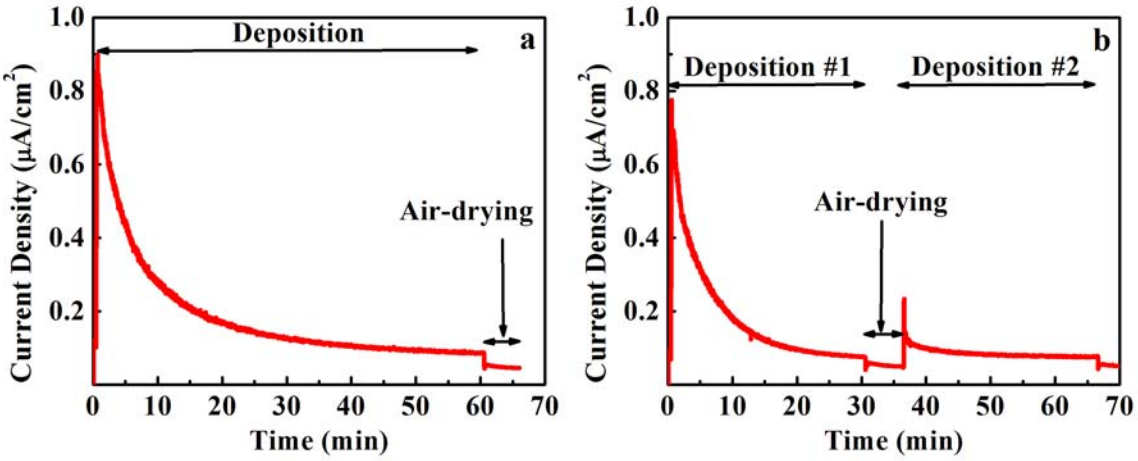

Figure 6.9: Current density profiles during the electrophoretic deposition of nanocrystals (a) single deposition for one hour (b) double deposition for 30 minutes each.

coverage compared to the single deposition. Electrophoretic current densities, measured during the nanocrystal depositions (Figure 6.9), provide an insight into origin of the effect. Figure 6.9(a) shows the current density during the single deposition (one hour), while figure 6.9(b) shows the current density during the double deposition (30 minutes each). As the deposition progress, the current density and, hence the deposition rate decrease due to the voltage drop across the continuously growing nanocrystal film. After air-drying and upon reinsertion into the nanocrystal suspension, the current density jumps to a higher level than before air-drying leading to the deposition of more nanocrystals. This observation suggested possibility of charge-neutralization during air-drying step. Since applied voltage was maintained during air-drying step, surface of the film could be neutralized by charges in air. Thus, double deposition of the nanocrystals reduced the porosity and improved the film coverage.

A view of the arrangement of nanocrystals in the film was provided by the high magnification SEM and AFM images. Both images show densely-packed, homogeneous, yet disordered Fe_3O_4 nanocrystal films [Figure 6.10(a)] with individual approximately 20 nm diameter iron oxide nanocrystals evident in the film. A thickness of approximately 150 nm of the nanocrystal films was measured from the cross-sectional SEM image [Figure 6.10(b)].

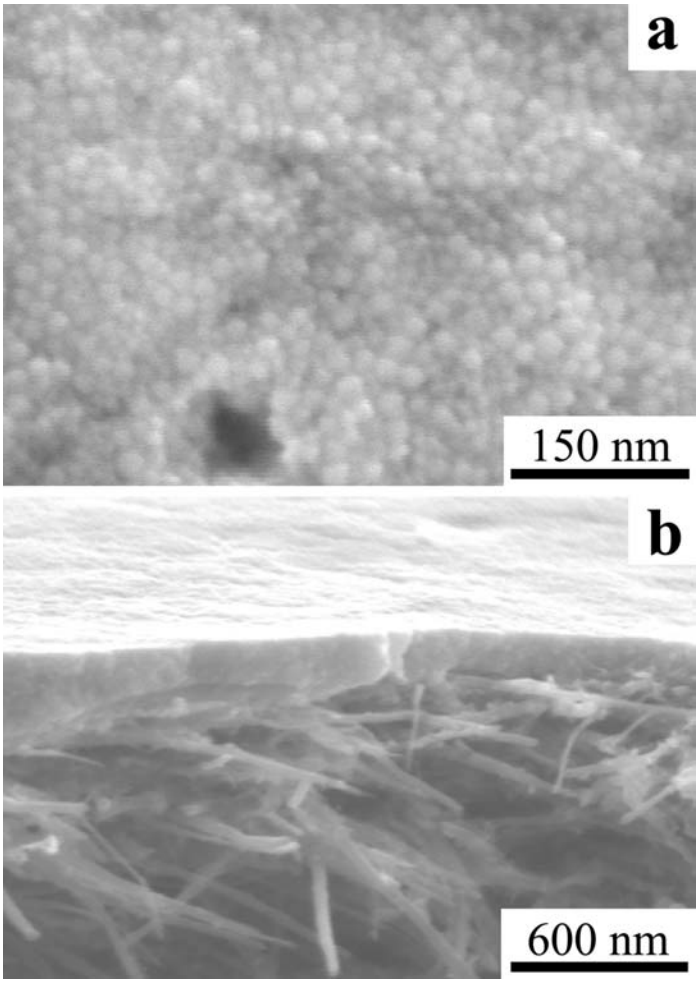

Figure 6.10: (a) High magnification SEM image of a twice-deposited nanocrystal film on a CNT mat. The individual Fe_3O_4 nanocrystals are visible in the image; (b) Cross-sectional SEM image shows the nanocrystal film thickness of $\sim$ 150 nm.

This image also verifies the dense packing of the nanocrystals throughout the film, which was achieved without the addition of a chemical binder or a cross-linking agent.

The *CNT mat-Fe_3O_4 NC film* structure was employed as an anode to deposit a second CNT mat, using the same electrode configuration and EPD *low field - high current* operating parameters as for the first CNT layer. The topology of the mat appears identical under SEM [Figure 6.11(a)] to that of the mat deposited directly onto steel [Figure 6.8(a)], confirming that high-quality CNT mats can be deposited even on the nanocrystal films with high reproducibility. Figure 6.11(b) shows the cross-sectional image of the *CNT mat-Fe_3O_4*

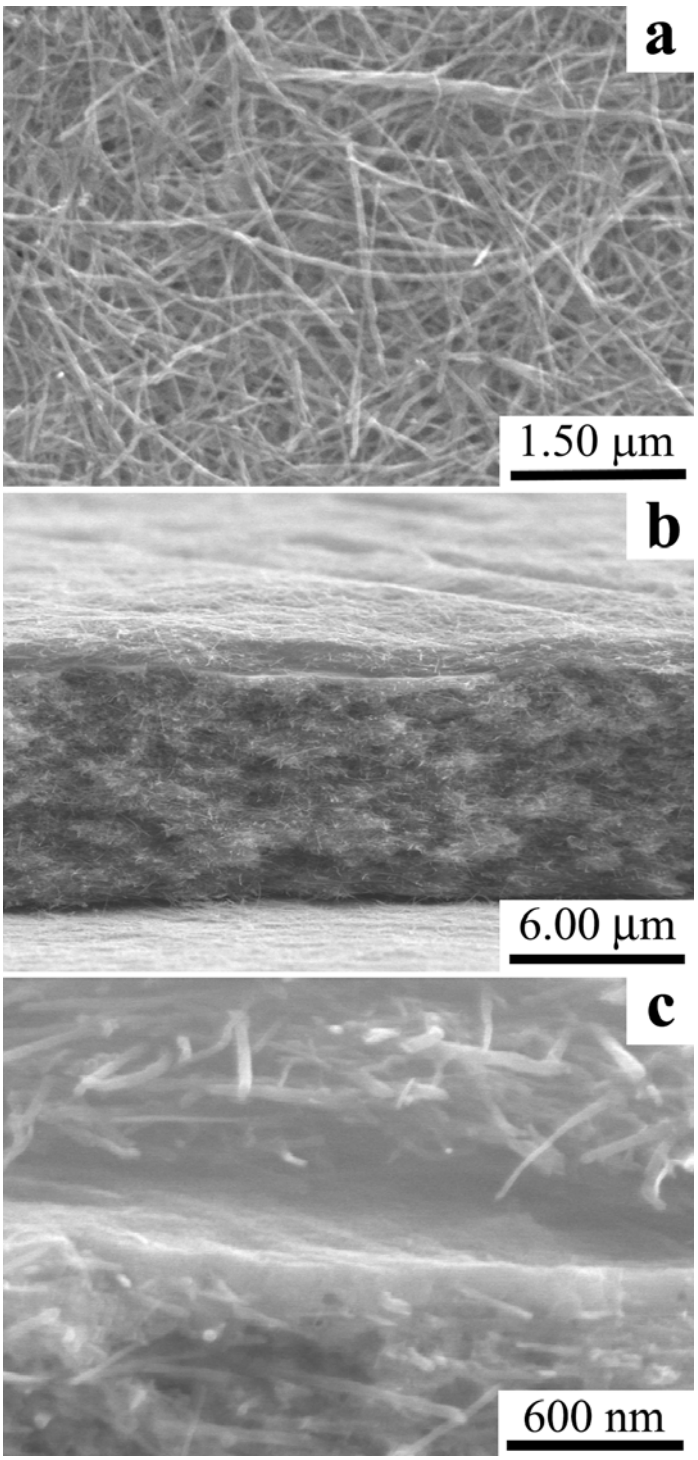

Figure 6.11: (a) SEM image of the top CNT mat of the *CNT mat-Fe_3O_4 NC film-CNT mat* heterostructure; (b) Cross-sectional SEM image of the heterostructure; (c) A magnified SEM image of the nanocrystal film between the two CNT mats.

NC film-CNT mat heterostructure. The approximate 6 μm thickness of the first CNT mat was measured from cross-sectional SEM image. The second CNT mat was approximately 1 μm thick, which was thinner than the first CNT mat deposited with the same EPD configuration and operating parameters. As described previously, much of the applied voltage drops across the preexisting CNT mat and particularly the low conductivity Fe_3O_4 nanocrystal film, resulting in a weaker EPD electric field and, hence, a thinner deposit during the second CNT deposition. The two CNT mats were clearly separated by the densely-packed Fe_3O_4 nanocrystal film, as seen in figure 6.11(c). Thus, the fabrication of *CNT mat-Fe_3O_4 NC film-CNT mat* heterostructure was successfully realized similar to the fabrication of *CNT mat-Eu_2O_3 NC film-CNT mat* heterostructure.

6.4 Summary

Multi-layered architectures, comprising carbon nanotubes and europium oxide or iron oxide nanocrystals, were successfully fabricated on steel substrates via an alternating sequence of *low field-high current* and *high field-low current* EPD techniques. *Low field-high current* EPD facilitated the deposition of uniform porous CNT mats. Densely packed Eu_2O_3 or Fe_3O_4 nanocrystal films were deposited via *high field-low current* EPD atop CNT mat. The nanocrystals deposited homogeneously on the CNT mat producing a smooth and continuous film. Surface coverage of the large Fe_3O_4 nanocrystals was improved with multiple depositions of the nanocrystals. The non-dispersibility of the CNTs in hexane prevented impregnation of the nanocrystal suspension into the CNT mat, leading to a sharp interface between the layers. *CV* measurements of the *CNT mat-Eu_2O_3 NC film-CNT mat* structure confirmed electrical insulation between the two CNT mats and the charge-storage capabilities of the structure. The successful development of energy-storage device prototypes, comprised of layered CNT mat-Eu_2O_3 NC film heterostructure, demands further research efforts in this area.

CHAPTER VII

CONCLUSIONS & FUTURE WORK

This dissertation explored the development of ultra-small (sub-3 nm diameter) rare-earth oxide nanocrystals and the assembly of these nanocrystals into homogeneous films via electrophoretic deposition to characterize their optical and dielectric properties. In addition, possibility of integrating the films of these nanocrystals with the films of carbon nanotubes in a layered architecture was explored for potential energy-storage device applications. Conclusions of the exploratory studies and the guidelines for the future work are outlined here.

The new solution-phase synthesis produced the smallest cubic-phase nanocrystals of the rare-earth oxides (Eu_2O_3, Tb_2O_3, Gd_2O_3, and Gd_2O_3:Eu^{3+}), which were capped with oleic acid as the surface capping ligand. The nanocrystals, produced with this synthesis, were easily cleaned with a simple precipitation-centrifugation procedure, which is an advantage of this synthesis. This synthesis should be applicable for the production of nanocrystals of the other rare-earth oxides. For the first time, homogeneous and smooth films of the rare-earth oxide nanocrystals were assembled successfully by electrophoretic deposition. Optical studies of the europium oxide nanocrystal films revealed their high transparency in visible spectral region and confirmed characteristic red luminescence. High transparency of the films should enhance emission efficiency of the films because scattering losses were minimized within the films, which is important for next-generation light emitting devices. The gadolinium oxide nanocrystals exhibited charge-storage capabilities when dielectric studies of their films were conducted. The charge-storage properties of gadolinium oxide nanocrystals should be useful in next-generation nanocrystal-based memory devices. Carbon nanotubes and nanocrystals were integrated using electrophoretic deposition into

layered architectures, which have potential applications in energy-storage devices.

The research discussed in this dissertation should be explored further. Effect of surface passivation on luminescence efficiency of the nanocrystals should be studied. Since a fraction of surface capping ligands is detached during each cleaning step, luminescence efficiency of the nanocrystals should be measured as a function of number of nanocrystal cleaning steps. Origin of the nanocrystal agglomeration during electrophoretic deposition should be identified so that nanocrystal agglomeration can be avoided. The amount and location of charge stored in gadolinium oxide nanocrystal films should be investigated with further experiments. In carbon nanotube-nanocrystal heterostructures, a systematic procedure needs to be developed to control surface coverage of the nanocrystal films on carbon nanotube mats.

CURRICULUM VITAE

Education:-

- **Doctor of Philosophy (Ph.D.)** in **Materials Science**
  Vanderbilt University, Nashville, TN USA (May 2010)
  Dissertation: "Ultra-small rare-earth oxide nanocrystals: development, film assembly, optical and dielectric studies"

- **Master of Science (M.S.)** in **Materials Science**
  Vanderbilt University, Nashville, TN USA (August 2006)
  Thesis: "Electro-thermal simulation studies of single-event burnout in power diodes"

- **Bachelor of Engineering (B.E.)** in **Metallurgy**
  University of Pune, Pune, MH INDIA (June 2000)
  Project: "Synthesis and characterization of Nickel-Zinc ferrites"

Awards & Honors:-

- Research poster award (2^{nd} place) at 9^{th} Vanderbilt Nanoscience and Nanotechnology Forum (2008)
- Rated "very good" lab instructor by students (Rating: 4.4/5.0) (2008)
- Recipient of Sigma Xi Research-in-Aid grant ($1000) (2008)
- Recipient of "Newport Spectra-Physics Research Excellence Travel Award" (2006)
- Full scholarship to attend Pan-American Advanced Studies Institute (PASI) on transmission electron microscopy at Santiago, Chile (One of the 48 award recipients from the Americas) (2006)
- University rank holder in junior and seniors years (1999, 2000)

Journal Publications:-

1. S. V. Mahajan and J. H. Dickerson, Dielectric properties of colloidal Gd_2O_3 nanocrystal films fabricated via electrophoretic deposition, *Appl. Phys. Lett.*, **96** 113105, (2010)
2. S. V. Mahajan and J. H. Dickerson, Understanding the growth of Eu_2O_3 nanocrystal films made via electrophoretic deposition, *Nanotechnology*, **21** 145704, (2010)
3. S. V. Mahajan, J. Cho, M. S. P. Shaffer, A. R. Boccaccini and J. H. Dickerson, Electrophoretic deposition and characterization of Eu_2O_3 nanocrystal-carbon nanotube heterostructures, *J. Eur. Ceram. Soc.*, **30** 1145, (2010)

4. S. V. Mahajan and J. H. Dickerson, Optical studies of sub-3 nm Eu_2O_3 and Gd_2O_3:Eu^{3+} nanocrystals, *J. Alloys Compd.*, **488** 574, (2009)

5. S. A. Hasan, D. W. Kavich, S. V. Mahajan and J. H. Dickerson, Electrophoretic deposition of CdSe nanocrystal films onto dielectric polymer thin films, *Thin Solid Films*, **517** 2665, (2009)

6. D. W. Kavich, J. H. Dickerson, S. V. Mahajan, S. A. Hasan and J. H. Park, Exchange bias of singly inverted FeO/Fe_3O_4 core-shell nanocrystals, *Phys. Rev. B*, **78** 174414, (2008)

7. S. V. Mahajan, S. A. Hasan, J. Cho, M. S. P. Shaffer, A. R. Boccaccini and J. H. Dickerson, Carbon nanotube-nanocrystal heterostructures fabricated by electrophoretic deposition, *Nanotechnology*, **19** 195301, (2008)

8. S. V. Mahajan, J. Hart, H. Hood, A. Everheart, M. L. Redigolo, D. S. Koktysh, E. A. Payzant, and J. H. Dickerson, Synthesis of $RE(OH)_2Cl$ and REOCl (RE=Eu, Tb) nanostructures, *J. Rare Earths*, **26** 131, (2008)

9. S. V. Mahajan and J. H. Dickerson, Synthesis of monodisperse sub-3 nm RE_2O_3 and Gd_2O_3:Eu^{3+} nanocrystals, *Nanotechnology*, **18** 325605, (2007)

10. S. V. Mahajan, D. W. Kavich, M. L. Redigolo, and J. H. Dickerson, Structural properties of electrophoretically deposited europium oxide nanocrystalline thin films, *J. Mater. Sci.*, **41** 8160, (2006)

REFERENCES

[1] Blasse G 1979 *Handbook on the Physics and Chemistry of Rare Earths* vol. 4 (North-Holland Pub.)

[2] Goldburt E T, Kulkami B, Bhargava R N, Taylor J and Libera M 1997 *J. Lumin.* **72-74** 190–192

[3] Wakefield G, Keron H A, Dobson P J and Hutchison J L 1999 *J. Colloid Interface Sci.* **215** 179–182

[4] Kwo J, Hong M, Kortan A R, Queeney K T, Chabal Y J, Mannaerts J P, Boone T, Krajewski J J, Sergent A M and Rosamilia J M 2000 *Appl. Phys. Lett.* **77** 130–132

[5] Blasse G and Grabmaier B C 1994 *Luminescent Materials* (Springer-Verlag)

[6] Shionoya S and Yen W M 1999 *Phosphor Handbook* (Boca Raton: CRC Press)

[7] Feng J, Shan G, Maquieira A, Koivunen M E, Guo B, Hammock B D and Kennedy I M 2003 *Anal. Chem.* **75** 5282–5286

[8] Nichkova M, Dosev D, Gee S J, Hammock B D and Kennedy I M 2005 *Anal. Chem.* **77** 6864–6873

[9] Eilers H and Tissue B M 1995 *Mater. Lett.* **24** 261–265

[10] Bihari B, Eilers H and Tissue B M 1997 *J. Lumin.* **75** 1–10

[11] Wakefield G, Keron H A, Dobson P J and Hutchison J L 1999 *J. Phys. Chem. Solids* **60** 503–508

[12] Bazzi R, Flores-Gonzalez M A, Louis C, Lebbou K, Zhang W, Dujardin C, Roux S, Mercier B, Ledoux G and Bernstein E 2004 *J. Colloid Interface Sci.* **273** 191–197

[13] Si R, Zhang Y W, You L P and Yan C H 2005 *Angew. Chem., Int. Ed. Engl.* **44** 3256–3260

[14] Si R, Zhang Y W, Zhou H P, Sun L D and Yan C H 2007 *Chem. Mater.* **19** 18–27

[15] Yang H S, Lee H and Holloway P H 2005 *Nanotechnology* **16** 2794–2798

[16] Dosev D, Guo B and Kennedy I M 2006 *J. Aerosol Sci.* **37** 402–412

[17] Islam M A and Herman I P 2002 *Appl. Phys. Lett.* **80** 3823–3825

[18] Mahajan S V, Kavich D W, Redigolo M L and Dickerson J H 2006 *J. Mater. Sci.* **41** 8160–8165

[19] Goldschmidt V M, Ulrich F and Barth T 1925 *Mater. Naturv.* **K1** 5

[20] Foëx M and Traverse J P 1966 *Rev. Int. Hautes Temp. Refract.* **3** 429

[21] Chikalla T D, McNeilly C E and Roberts F P 1972 *J. Am. Ceram. Soc* **55** 428

[22] Pauling L 1928 *Z. Krystallogr.* **69** 415

[23] Koehler W C and Wollan E O 1953 *Acta Crystallogr.* **6** 741

[24] Douglass R M and Staritzky E 1956 *Anal. Chem.* **28** 552

[25] Cromer D T 1957 *J. Phys. Chem.* **61** 753

[26] Pauling L and Shappell M D 1930 *Z. Krystallogr.* **75** 128

[27] Eyring L 1991 *Synthesis of Lanthanide and Actinide Compound* (Kluwer Academic Publisher)

[28] Blasse G 1992 *Int. Revs. Phys. Chem* **11** 71

[29] Dieke G H 1968 *Spectra and Energy Levels of Rare Earth Ions in Crystals* (New York: Wiley)

[30] Carnall W T, Fields P R and Rajnak K 1968 *J. Chem. Phys.* **49** 4450–4455

[31] Ofelt G S 1962 *J. Chem. Phys.* **37** 511–519

[32] Prokofiev A M, Shelykh A I and Melekh B T 1996 *J. Alloys Compd.* **242** 41–44

[33] Rozhkov V A, Trusova A Y and Berezhnoy I G 1998 *Thin Solid Films* **325** 151

[34] Subba Rao G V, Ramdas S, Mehrotra P N and Rao C N R 1970 *J. Solid State Chem.* **2** 377–384

[35] Hubbard K J and Schlom D G 1996 *J. Mater. Res.* **11** 2757–2776

[36] Louis C, Bazzi R, Flores M A, Zheng W, Lebbou K, Tillement O, Mercier B, Dujardin C and Perriat P 2003 *J. Solid State Chem.* **173** 335–341

[37] Bazzi R, Flores-Gonzalez M A, Louis C, Lebbou K, Dujardin C, Brenier A, Zhang W, Tillement O, Bernstein E and Perriat P 2003 *J. Lumin.* **102** 445–450

[38] Soderlind F, Pedersen H, Petoral J R M, Kall P O and Uvdal K 2005 *J. Colloid Interface Sci.* **288** 140–148

[39] Cao Y C 2004 *J. Am. Chem. Soc* **126** 7456–7457

[40] Wang H Z, Uehara M, Nakamura H, Miyazaki M and Maeda H 2005 *Adv. Mater.* **17** 2506–2509

[41] Mahajan S V and Dickerson J H 2007 *Nanotechnology* **18** 325605

[42] Park J, An K J, Hwang Y S, Park J G, Noh H J, Kim J Y, Park J H, Hwang N M and Hyeon T 2004 *Nat. Mater.* **3** 891–895

[43] Pavia D L, Lampman G M and Kriz G S 1979 *Introduction to Spectroscopy: A Guide for Students of Organic Chemistry* (Philadelphia: W.B. Saunders Company)

[44] Hyeon T, Lee S S, Park J, Chung Y and Na H B 2001 *J. Am. Chem. Soc.* **123** 12798–12801

[45] Shim M and Guyot-Sionnest P 2000 *Nature* **407** 981–983

[46] Qu F Y, Oliveira R H and Morais P C 2004 *J. Magn. Magn. Mater.* **272** 1668–1669

[47] Nakamoto K 1997 *Infrared and Raman Spectra of Inorganic and Coordination Compounds* (New York: John Wiley & Sons)

[48] Ren Y, Iimura K i and Kato T 2001 *Langmuir* **17** 2688–2693

[49] Mahajan S V and Dickerson J H 2009 *J. Alloys Compd.* **488** 574–577

[50] Maenosono S, Okubo T and Yamaguchi Y 2003 *J. Nanopart. Res.* **5** 5–15

[51] Besra L and Liu M 2007 *Prog. Mater Sci.* **52** 1–61

[52] Fukada Y, Nagarajan N, Mekky W, Bao Y, Kim H S and Nicholson P S 2004 *J. Mater. Sci.* **39** 787–801

[53] Put S, Vleugels J, Anne G and Van der Biest O 2003 *Colloids Surf., A* **222** 223–232

[54] Sarkar P, Datta S and Nicholson P S 1997 *Composites Part B-Engineering* **28** 49–56

[55] Ferrari B, Sanchez-Herencia A J and Moreno R 1998 *Mater. Res. Bull.* **33** 487–499

[56] Zhitomirsky I and GalOr L 1997 *Journal of Materials Science-Materials in Medicine* **8** 213–219

[57] Sridhar T M and Mudali U K 2003 *Tran. Ind. Inst. Metals* **56** 221–230

[58] Dabbousi B O, Bawendi M G, Onitsuka O and Rubner M F 1995 *Appl. Phys. Lett.* **66** 1316–1318

[59] Shevchenko E V, Talapin D V, Kotov N A, O'Brien S and Murray C B 2006 *Nature* **439** 55–59

[60] Mirkin C A, Letsinger R L, Mucic R C and Storhoff J J 1996 *Nature* **382** 607–609

[61] Murray C B, Kagan C R and Bawendi M G 1995 *Science* **270** 1335–1338

[62] Dabbousi B O, Murray C B, Rubner M F and Bawendi M G 1994 *Chem. Mater.* **6** 216–219

[63] Kim F, Kwan S, Akana J and Yang P 2001 *J. Am. Chem. Soc* **123** 4360–4361

[64] Singh I, Kaya C, Shaffer M S P, Thomas B C and Boccaccini A R 2006 *J. Mater. Sci.* **41** 8144–8151

[65] Mahajan S V, Hasan S A, Cho J, Shaffer M S P, Boccaccini A R and Dickerson J H 2008 *Nanotechnology* **19** 8

[66] Giersig M and Mulvaney P 1993 *J. Phys. Chem.* **97** 6334–6336

[67] Teranishi T, Hosoe M, Tanaka T and Miyake M 1999 *J. Phys. Chem. B* **103** 3818–3827

[68] Wong E M and Searson P C 1999 *Appl. Phys. Lett.* **74** 2939–2941

[69] Dor S, Ruhle S, Ofir A, Adler M, Grinis L and Zaban A 2009 *Colloids Surf., A* **342** 70–75

[70] Ferrari B, Bartret A and Baudin C 2009 *J. Eur. Ceram. Soc.* **29** 1083–1092

[71] Mahajan S V, Cho J, Shaffer M S P, Boccaccini A R and Dickerson J H 2010 *J. Eur. Ceram. Soc.* **30** 1145–1150

[72] Castro Y, Ferrari B, Moreno R and Duran A 2004 *Surf. Coat. Technol.* **182** 199–203

[73] Jung D, Tabellion J and Clasen R 2006 *Key Eng. Mater.* **314** 81–88

[74] Islam M A, Xia Y Q, Steigerwald M L, Yin M, Liu Z, O'Brien S, Levicky R and Herman I P 2003 *Nano Lett.* **3** 1603–1606

[75] Somarajan S, Hasan S A, Adkins C T, Harth E and Dickerson J H 2008 *J. Phys. Chem. B* **112** 23–28

[76] Zhao G F, Ishizaka T, Kasai H, Hasegawa M, Furukawa T, Nakanishi H and Oikawa H 2009 *Chem. Mater.* **21** 419–424

[77] Boccaccini A R, Cho J, Roether J A, Thomas B J C, Minay E J and Shaffer M S P 2006 *Carbon* **44** 3149–3160

[78] Cho J, Schaab S, Roether J A and Boccaccini A R 2008 *J. Nanopart. Res.* **10** 99–105

[79] Du C S and Pan N 2006 *Nanotechnology* **17** 5314–5318

[80] Du C S and Pan N 2006 *J. Power Sources* **160** 1487–1494

[81] Thomas B J C, Boccaccini A R and Shaffer M S P 2005 *J. Am. Ceram. Soc.* **88** 980–982

[82] Thomas B J C, Shaffer M S P, Freeman S, Koopman M, Chawla K K and Boccaccini A R 2006 *Key Eng. Mater.* **314** 141–146

[83] Islam M A and Xia S G 2009 *J. Phys. Condens. Matter* **21** 285301

[84] Hamaker H C 1940 *Trans. Farad. Soc.* **36** 279–83

[85] Avgustinik A I, Vigdergauz V S and Zhuravlev G I 1962 *J Appl. Chem. USSR* **35** 2175–2180

[86] Van der Biest O O and Vandeperre L J 1999 *Annu. Rev. Mater. Sci.* **29** 327–352

[87] Zhitomirsky I 2002 *Adv. Coll. Interface Sci.* **97** 279–317

[88] Moreno R and Ferrari B 2000 *Mater. Res. Bull.* **35** 887–897

[89] Sigmund W M, Bell N S and Bergstrom L 2000 *J. Am. Ceram. Soc.* **83** 1557–1574

[90] Yates D E, Levine S and Healy T W 1974 *J. Chem. Soc.-Farad. Trans. I* **70** 1807–1818 times Cited: 680

[91] Wang G H, Sarkar P and Nicholson P S 1997 *J. Am. Ceram. Soc.* **80** 965–972

[92] Wang G H, Sarkar P and Nicholson P S 1999 *J. Am. Ceram. Soc.* **82** 849–856

[93] Vandeperre L, Zhao C and Van der Biest O 2000 in *Sixth conference and exhibition of the European Ceramic Society* (Brighton, UK: Institute of Materials) pp. 69–74

[94] Negishi H, Yamaji K, Imura T, Kitamoto D, Ikegami T and Yanagishita H 2005 *J. Electrochem. Soc.* **152** J16–J22

[95] Ishihara T, Sato K and Takita Y 1996 *J. Am. Ceram. Soc.* **79** 913–919

[96] Mathews T, Rabu N, Sellar J R and Muddle B C 2000 *Solid State Ionics* **128** 111–115

[97] Deryaguin B V and Landau L D 1941 *Acta Physicochim USSR* **14** 633

[98] Verwey E J W and Overbeek J T G 1948 *Theory of the stability of lyophobic colloids* (Amsterdam: Elsevier)

[99] Von Smoluchowski M 1917 *Z Phys Chem* **92** 129–168

[100] Moon J M, An K H, Lee Y H, Park Y S, Bae D J and Park G S 2001 *J. Phys. Chem. B* **105** 5677–5681

[101] Shaffer M S P, Fan X and Windle A H 1998 *Carbon* **36** 1603–1612

[102] Esumi K, Ishigami M, Nakajima A, Sawada K and Honda H 1996 *Carbon* **34** 279–281

[103] Cushing B L, Kolesnichenko V L and O'Connor C J 2004 *Chem. Rev.* **104** 3893–3946

[104] Shim M and Guyot-Sionnest P 1999 *J. Chem. Phys.* **111** 6955–6964

[105] Islam M A, Xia Y Q, Telesca D A, Steigerwald M L and Herman I P 2004 *Chem. Mater.* **16** 49–54

[106] Kasuya R, Kawano A and Isobe T 2007 *Appl. Phys. Lett.* **91** 111916

[107] Raue R, Vink A T and Welker T 1989 *Philips Tech. Rev.* **44** 335–347

[108] Mochizuki S, Nakanishi T, Suzuki Y and Ishi K 2001 *Appl. Phys. Lett.* **79** 3785–3787

[109] Wang Y C, Leu I C and Hon M H 2004 *J. Am. Ceram. Soc.* **87** 84–88

[110] Zhitomirsky I and GalOr L 1997 *J. Mater. Sci. - Mater. Med.* **8** 213–219

[111] Hsieh L Z, Ko H H, Kuei P Y, Chang L B and Jeng M J 2005 *J. Appl. Phys.* **98**

[112] Nazarov A N, Gomeniuk Y V, Gomeniuk Y Y, Gottlob H D B, Schmidt M, Lemme M C, Czernohorsky M and Osten H J 2007 *Microelectron. Eng.* **84** 1968–1971

[113] Endres R, Stefanov Y and Schwalke U 2007 *Microelectronics Reliability* **47** 528–531

[114] Wang J C, Lai C S, Chen Y K, Lin C T, Liu C P, Huang M R S and Fang Y C 2009 *Electrochem. Solid-State Lett.* **12** H202–H204

[115] Guan W H, Long S B, Liu M, Li Z G, Hu Y and Liu Q 2007 *J. Phys. D: Appl. Phys.* **40** 2754–2758

[116] Park B, Cho K, Kim H and Kim S 2006 *Semicond. Sci. Technol.* **21** 975–978

[117] Yim S S, Lee M S, Kim K S and Kim K B 2006 *Appl. Phys. Lett.* **89** 093115–3

[118] Kanjilal A, Hansen J L, Gaiduk P, Larsen A N, Cherkashin N, Claverie A, Normand P, Kapelanakis E, Skarlatos D and Tsoukalas D 2003 *Appl. Phys. Lett.* **82** 1212–1214

[119] Duguay S, Grob J J, Slaoui A, Le Gall Y and Amann-Liess M 2005 *J. Appl. Phys.* **97** 104330

[120] Liu Y, Chen T P, Ding L, Zhang S, Fu Y Q and Fung S 2006 *J. Appl. Phys.* **100** 096111

[121] Shi Y, Saito K, Ishikuro H and Hiramoto T 1998 *J. Appl. Phys.* **84** 2358–2360

[122] Scott G D and Kilgour D M 1969 *J. Phys. D: Appl. Phys.* **2** 863–866

[123] Xia Y N, Yang P D, Sun Y G, Wu Y Y, Mayers B, Gates B, Yin Y D, Kim F and Yan Y Q 2003 *Adv. Mater.* **15** 353–389

[124] Baughman R H, Zakhidov A A and de Heer W A 2002 *Science* **297** 787–792

[125] Yu M F, Lourie O, Dyer M J, Moloni K, Kelly T F and Ruoff R S 2000 *Science* **287** 637–640

[126] Kagan C R 1996 Ph.D. thesis

[127] Murray C B, Kagan C R and Bawendi M G 2000 *Annu. Rev. Mater. Sci.* **30** 545–610

[128] Boccaccini A R, Roether J A, Thomas B J C, Shaffer M S P, Chavez E, Stoll E and Minay E J 2006 *J. Ceram. Soc. Jpn.* **114** 1–14

[129] Cava C E, Possagno R, Schnitzler M C, Roman P C, Oliveira M M, Lepiensky C M, Zarbin A J G and Roman L S 2007 *Chem. Phys. Lett.* **444** 304–308

[130] Choi W B, Chung D S, Kang J H, Kim H Y, Jin Y W, Han I T, Lee Y H, Jung J E, Lee N S, Park G S and Kim J M 1999 *Appl. Phys. Lett.* **75** 3129–3131

[131] Du C S and Pan N 2006 *Nanotechnology* **17** 5314–5318

[132] Georgakilas V, Gournis D, Tzitzios V, Pasquato L, Guldi D M and Prato M 2007 *J. Mater. Chem.* **17** 2679–2694

[133] Girishkumar G, Vinodgopal K and Kamat P V 2004 *J. Phys. Chem. B* **108** 19960–19966

[134] Kalbac M, Frank O, Kavan L, Zukalova M, Prochazka J, Klementova M and Dunsch L 2007 *J. Electrochem. Soc.* **154** K19–K24

[135] Li W Z, Liang C H, Zhou W J, Qiu J S, Zhou Z H, Sun G Q and Xin Q 2003 *J. Phys. Chem. B* **107** 6292–6299

[136] Xue B, Chen P, Hong Q, Lin J Y and Tan K L 2001 *J. Mater. Chem.* **11** 2378–2381

[137] Chicatun F, Cho J, Schaab S, Brusatin G, Colombo P, Roether J A and Boccaccini A R 2007 *Adv. Appl. Ceram.* **106** 186–195

[138] Dakhel A A 2004 *Eur. Phys. J.: Appl. Phys.* **28** 59–64

[139] Singh M P, Shalini K, Shivashankar S A, Deepak G C, Bhat N and Shripathi T 2008 *Mater. Chem. Phys.* **110** 337–343

[140] Singh C, Shaffer M S and Windle A H 2003 *Carbon* **41** 359–368

[141] Du C, Yeh J and Pan N 2005 *J. Mater. Chem.* **15** 548–550

[142] Corni I, Ryan M P and Boccaccini A R 2008 *J. Eur. Ceram. Soc.* **28** 1353–1367

[143] Mikhelashvili V, Eisenstein G and Lahav A 2007 *Appl. Phys. Lett.* **90**

[144] Yuan H, Cheow P S, Ong J and Toh C S 2008 *Sens. Actuators B* **134** 127–132